TECHNISCHE UNIVERSITÄT MÜNCHEN
Institut für Nanoelektronik

Nanoimprint technologies for energy conversion applications

Robin Daniel Nagel

Vollständiger Abdruck der von der Fakultät für Elektrotechnik und Informationstechnik der Technischen Universität München zur Erlangung des akademischen Grades eines

Doktor der Naturwissenschaften

genehmigten Dissertation.

Vorsitzender:	Prof. Dr.-Ing. Klaus Diepold
Prüfer der Dissertation:	1. Prof. Dr. Paolo Lugli
	2. Prof. Dr. Katharina Krischer
	3. Prof. Dr. Bernhard Wolfrum

Die Dissertation wurde am 20.04.2020 bei der Technischen Universität München eingereicht und durch die Fakultät für Elektrotechnik und Informationstechnik am 28.10.2020 angenommen.

1 Abstract

The aim of this thesis is to implement and optimize nano-transfer printing and nanoimprint lithography as reliable and reproducible methods for the fabrication of metal nanoelectrodes for energy conversion applications with a focus on heterogeneous electrocatalysis. The basis of the experiments is the development of a stamp replication process, where the fabricated semi-flexible working stamps can then be used for both patterning methods. The final electrodes on silicon substrates are characterized and discussed in terms of electrical and optical properties, morphology, resolution, shape retention and electrocatalytic activity. It is demonstrated that nano-transfer printing is an excellent method for directly printing electrical circuits and functional devices fast and easily in a purely additive manner. The separation of used chemicals and structuring processes from the sample opens up a variety of new applications (e.g. in organic electronics), where standard patterning procedures are often inapplicable. A lift-off nanoimprint lithography process is developed, enabling in situ feature size tuning and high aspect ratio metal structures. It is found that for electrochemical experiments where high potentials in acidic environments are applied, lift-off nanoimprint lithography provides highly stable nanostructures. Both methods offer patterning in the sub-50 nm range with nanometer scale precision. Arrays of gold nanoelectrodes are fabricated on p-silicon substrates and the efficiency of the fabricated solar fuel device is tested in terms of hydrogen evolution and carbon dioxide reduction. A strong reduction of the needed on-set over-potential for these reactions is found with decreasing electrode size as well as a change in product selectivity.

Contents

2 Introduction

The ability to fabricate micro- and nanostructures over large areas with high throughput is of crucial importance to the advancement of nanoscience and for the semiconductor industry. Especially in the semiconductor industry, the capability to manufacture high-density components and integrated circuits (ICs) can be a decisive factor for a company's survival. The International Roadmap for Devices and Systems (2018) defined 7 nanometers to be the node range labeling for 2019 and the physical gate length (defined as the distance between metallurgical source/drain junctions) to be 18 nm. This has already been reached by industry standards. Critical issues, such as resolution, reliability, and production speed have to be addressed to develop new lithography processes or only to further refine existing ones. Here, optical lithography is still the standard for microprocessor fabrication, where the diffraction of light limits the overall resolution. The so-called Abbe diffraction limit is roughly half of the used wavelength for resist exposure, yet can be lowered by increasing the numerical aperture of the optical system. This limit can be pushed further to the already achieved range by using advanced techniques, such as extreme ultraviolet (EUV) radiation, high refractive index immersion oils, phase-shifting masks, off-axis illumination, and multiple patterning. As a result, the well-known Moore's law that states that the number of transistors in dense integrated circuits doubles about every year [1] (sometimes cited to be 18 or 24 months depending on the reference) is still valid. However, this exponential growth of the transistor density comes along with exponential growth of the cost of the exposure units. For large-scale chip fabrication, the cost of such a unit already exceeds the 100 million dollar mark.

In principle, a wide range of fabrication techniques can be used instead to produce metal nanostructures. Self-assembly methods like nanosphere lithography, micellar nanolithography, or template-assisted electrodeposition are capable of forming structures in the nanometer range. However, their final shape is predefined by the used method. Instead, electron-beam (e-beam) lithography is commonly used for nanopatterning purposes in scientific research and provides a very high feature resolution. The main problem though is its purely linear writing behavior result-

ing in very low throughput, which limits the maximum possible structured area or leads to very high production costs and durations. This is where nanoimprint lithography (NIL) steps in, combining large area nanopatterning with low-cost fabrication and a free to choose layout and structure shape[2,3]. Here, the pattern is initially defined on a template as a 3D-relief structure. It can then be used to directly transfer patterned thin metal layers to a receiving substrate in a nano-transfer printing process (nTP) or to replicate its features in a soft polymer layer, which then acts as a mask for subsequent etching or metalization steps.
Possible applications of nanoimprint technology are as versatile as the need for nanostructured surfaces. From the fabrication of electrical interconnects, in photonics, to organic light-emitting diodes, magnetic devices, and biological applications (just to name a few), any field of application can benefit individually and in a unique way from the miniaturization of structures. In this thesis, the focus is laid on the energy conversion field with a special interest in the catalytic conversion of carbon dioxide (CO_2) into usable carbon fuels (figure 2.1)

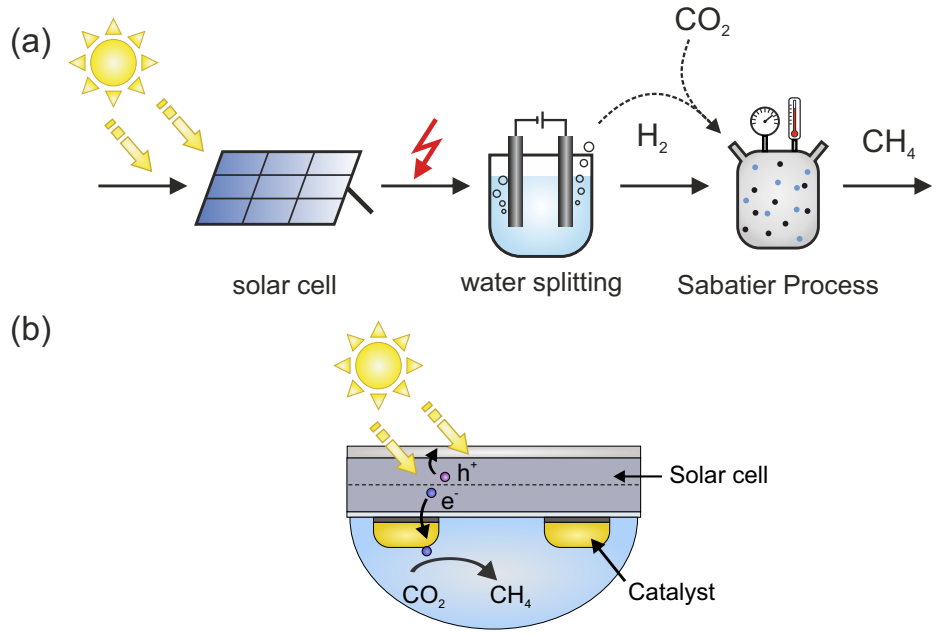

Figure 2.1: Sketch of possible methanation processes. (a) Power-to-gas approach: Several steps are needed resulting in low overall efficiency. (b) Photoelectrochemical device: All steps are combined into one single device.

Due to the need for regeneratively produced fuels and base chemicals, this has drawn much attention in recent years. A typical approach is the Power-to-gas (P2G) technology that converts electrical power to gas fuel, e.g. hydrogen or methane. In the case of carbon fuels, CO_2 combined with hydrogen can undergo a methanation reaction (such as the Sabatier reaction). Here, hydrogen can also

be obtained from electrical energy through the electrolysis of water, while the overall energy conversion can be renewable if solar cells are used as the electrical power source. This concept has already been tested but is not yet efficient enough as it involves several conversion steps (sunlight to electricity, electricity to H_2 and H_2+CO_2 to CH_4), each of which has individual conversion losses that multiply to a low overall efficiency (figure 2.1(a)). A better approach would be to combine these processes into one single PhotoElectroChemical (PEC) device, where photoelectrons are directly used on a catalyst surface to trigger the mentioned chemical reaction (figure 2.1(b)). PEC devices for water splitting[4–6] and carbon dioxide reduction[7–9] have already been reported, yet are still far away from being economically viable. The combination of several process steps into a single device, of course, involves some challenges: First, there must be a material combination providing a sufficiently high photovoltage to drive the electrochemical reaction. Secondly, the photon absorber must be decorated with an efficient catalyst material while allowing a fast electron transfer at the electrode/electrolyte interface. Besides, the device must be stable concerning electro corrosion. Recent studies showed that silicon-based multijunction cells can fulfill these requirements for water splitting applications[10,11].

The aim of this thesis is to utilize nanoimprint technologies as a step forward to develop and optimize a PEC device that can convert CO_2 to carbon fuels. This includes the development of a scalable and reliable nanopattern replication process (Chapter 4) where imprint molds are used to directly transfer metal electrodes on a photon absorber (silicon) (Chapter 6) or where a patterned resist is used as a mask for subsequent metal deposition and lift-off processes (Chapter 5). Both methods are characterized and optimized towards their application in electrochemistry in terms of electrode morphology, surface cleanliness (contaminations), and electrical properties of the metal-/semiconductor and metal-/electrolyte interfaces (Chapter 7). Electrocatalytic experiments will demonstrate the advantages of nanoimprint technology for this purpose and show that electrode size variations can significantly improve the efficiency and product selectivity of chemical processes.

3 Materials and methods

In this work, several fabrication and characterization technologies have been used. The following chapter will describe the most important techniques, such as lithographic patterning, dry-chemical etching, metal deposition, and cyclic voltammetry to give a basic understanding for the discussion in the later chapters.

3.1 Lithographic patterning methods

3.1.1 Photolithography

Photolithography is a wide-spread used process in microfabrication. This, often called conventional lithography, offers large area patterning and high throughput. However, light diffraction limits the maximum resolution.

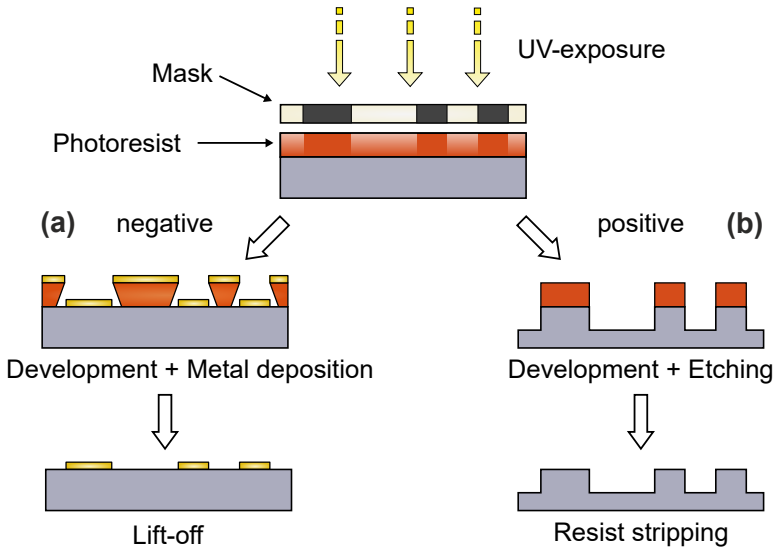

Figure 3.1: Schematic of a photolithography process. The coated substrate is exposed to UV light through a mask. After developing, the pattern is transferred to the photoresist and can be used for subsequent etching or deposition steps.

In Photolithography, a substrate is coated with a thin layer of photosensitive polymer (photoresist). It is then exposed to UV light through a mask (figure 3.1), which contains a predefined pattern of typically a thin chrome layer. The exposure

causes a local chemical change of the resist. The typical resists used in this thesis consisted of Novolak (a phenolic resin) and a photo-active DiazoNaphtoQuinon-sulphonate group (DNQ). During exposure (with light of 320-440 nm wavelength), the DNQ is converted into a carbonylic acid by elimination of nitrogen and binding of a water molecule. Using a developer (typically a solution consisting of potassium hydroxide or sodium hydroxide), either the exposed part of the resist (positive) or the unexposed one (negative) is removed. The patterned resist layer itself then acts as a mask for further etching or depositing steps.
In this thesis, an image reversal resist (AZ5214E, Microchemicals GmbH, Germany) was used. This resist can be used in a positive or negative process type. The positive one involves only a single exposure step and results in nearly vertical sidewalls of the developed resist pattern. It is used for subsequent dry-etching steps, where the etching process itself will also remove parts of the photoresist. This will minimize a widening effect of the cavities throughout the etching. The same photoresist can also be used in an image reversal (negative) process. Here, while using a photolithographic mask, only a very short UV exposure duration is chosen. As a consequence, only the top part of the resist is chemically changed, leaving the resist close to the substrate partially unexposed. The sample is then baked on a hotplate, causing the exposed parts of the polymer (which were soluble to the developer) to cross-link and leading to the neutralization of carboxylic acid formed by the DNQ, which drastically lowers its developing rate. As a final step, a flood exposure (no mask) is performed only affecting the parts of the photoresist, which have not yet been exposed. This not only results in a pattern inversion but also in an undercut formation at their edges (see figure 5.20 (a)). A negative sidewalls slope facilitates the separation of metal layers on top of the resist and those on the substrate during metal deposition, resulting in an easy lift-off step.
A mask aligner "MJB3" and "MA6" for larger substrates and SCIL imprinting from Süss MicroTec, Germany, was used for optical lithography and OrmoStamp® fabrication.

3.1.2 Nanoimprint lithography

Nanoimprint lithography (NIL) is an alternative nanopatterning method, combining nanometer-scale resolution and high throughput. It is based on a replication technique that has proven to provide high resolution even when using low-cost equipment. In fact, the resolution achieved so far by molding is in the same range or even higher than the one used in high-end photolithography tools in industrial

fabrication of microprocessors and memory chips and can reach values of 5 nm and below[12]. It is especially useful when large numbers of identical samples for statistical evaluation or large-scale device fabrication are needed. This makes NIL a promising technology for next-generation nanolithography.
In a top-down approach, a substrate is structured with a 3D relief. For a free to choose layout, a high-end patterning tool such as e-beam lithography is required. This written master stamp can then be used for multiple imprinting processes or as a template for casting multiple working stamps. Thus, the initial effort is capitalized more efficiently.

Nanoimprint process

The nanoimprint process is based on a squeeze flow of molding material. Figure 3.2 gives a schematic overview of this process, where the difference between the most common types of NIL, namely thermal NIL and UV-NIL, is highlighted. A patterned stamp is pressed against a thin layer of imprint-polymer resist on a substrate. When using a thermal imprint thermoplastic resist (**thermal NIL**), the glass transition temperature T_g of the polymer is above room temperature (T_i). Consequently, it has an initially high viscosity and can be considered as a solid. This mechanical property can be repeatedly and reversibly changed from a solid into a viscous state by varying the process temperature T_p.
After pressure is applied, the polymer film is heated through the substrate, and its temperature is raised above T_g. This allows the liquified resist to flow and it is forced to fill all cavities of the mold, conforming exactly to the surface relief of the stamp. When the cavities are filled, the resist is cooled down below T_g resulting in a hardening of the now embossed layer.
When performing UV-light induced NIL (**UV-NIL**), the imprint polymer is a UV-curable resin, which is initially low viscous. Here, no heating and only a little pressure are needed for the imprinting as T_g is far above room temperature (figure 3.2). After the stamp cavities are filled during imprinting, the polymer is exposed to UV light, which initiates a cross-linking and hardening of the resist. One could say that this exposure chemically increases T_g above T_p, but this is only legit, when the process is reversible, which for most materials won't be the case.
After releasing the pressure, the stamp can be demolded from the substrate without a reflow of the resist, and it can be reused for the next imprint cycle.
Imprinting will always leave a thin residual layer on the substrate. Only in special cases, a dewetting effect can intrinsically remove such a layer after demolding. As

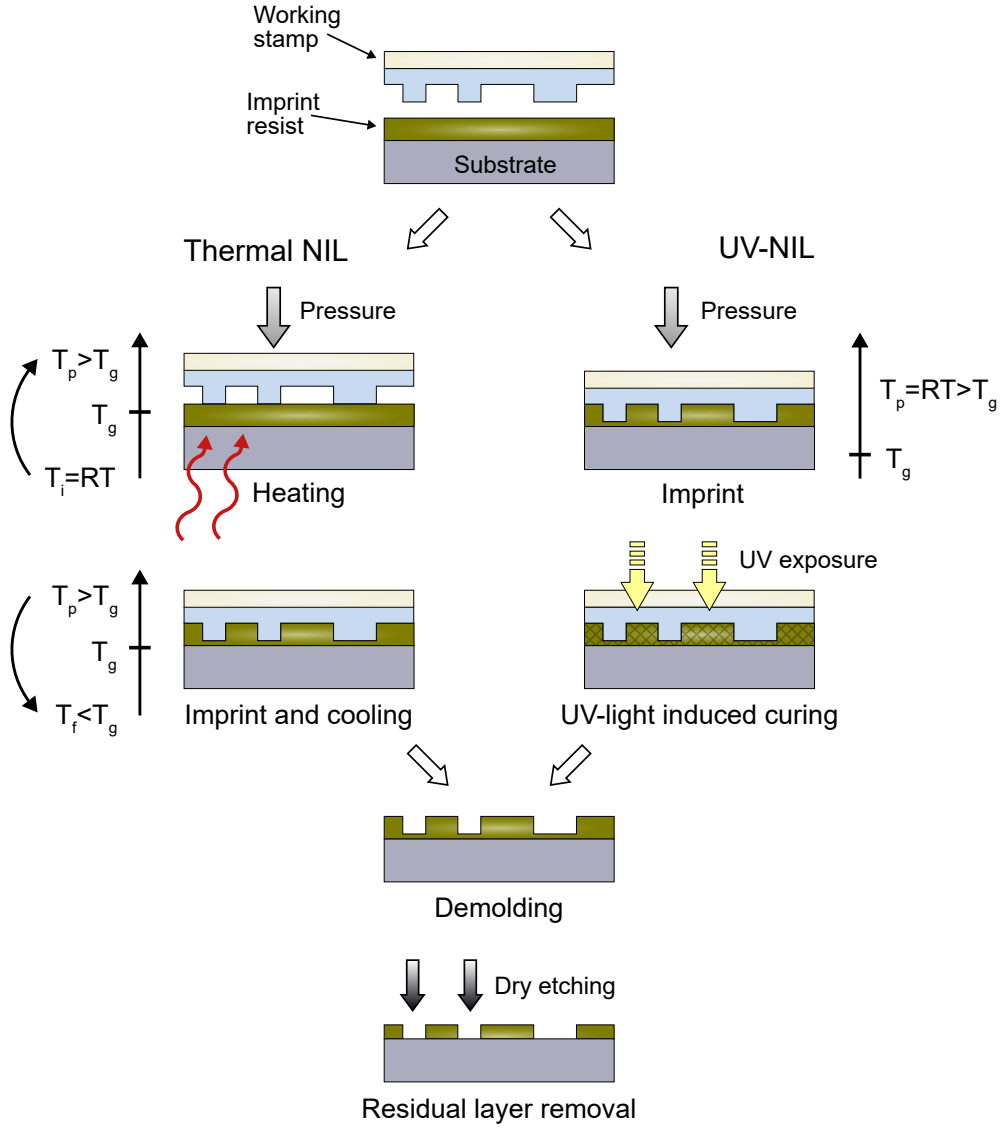

Figure 3.2: Schematic overview of a nanoimprint lithography process. A polymer resist layer on a substrate is patterned, which serves as a mask for any subsequent processing step. In thermal NIL this is achieved by heating the resist above its glass transition temperature. In UV-NIL, an already low viscous resist is hardened after the molding by exposing it to UV light.

a consequence, this remaining layer has to be removed to open up the underlying substrate surface. In this work, this was done using reactive ion etching with oxygen plasma, an anisotropic dry-etching method that can thereby maintain the shape of the pattern (section 3.4). The thickness of this residual layer depends on the initial thickness of the imprint polymer and the topology of the stamp. A more detailed insight into NIL theory and imprint parameters can be found in chapter 5.

UV-NIL is the faster one of the two methods. As the curing duration for a given imprint resist only depends on the intensity of the used UV source, it can be as

fast as few seconds. Thermal NIL needs a heating step and especially a time-consuming cooling step. On the other hand, UV-NIL processes require either a UV-transparent stamp or substrate. In this thesis, we mainly use thermal NIL for the fabrication of electrochemical devices and an adapted UV-NIL process for the fabrication of semi-flexible copies of a silicon master stamp.

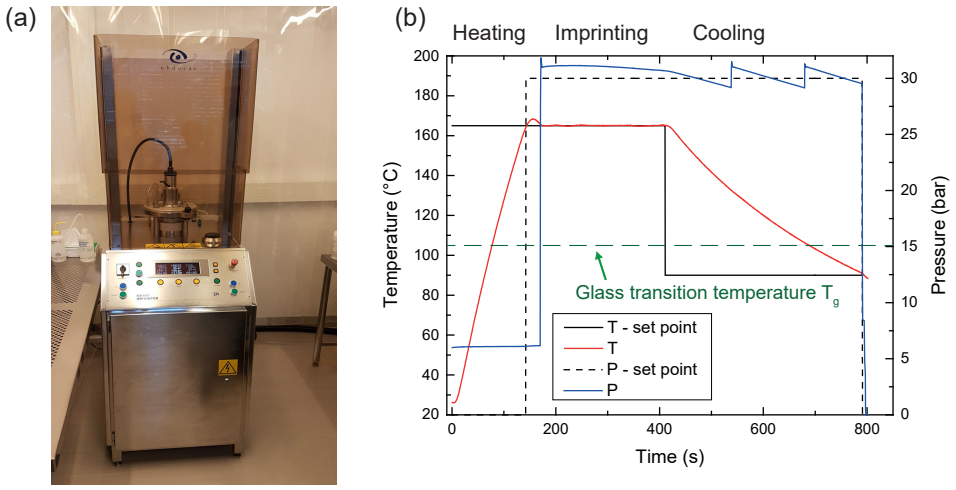

Figure 3.3: (a) Photo of an Obducat Nanoimprinter 2.5. (b) Typical thermal NIL process of an imprint polymer mr-I 8000R: The temperature is set to 165°C and the samples are heated. A small overshoot occurs due to thermal lag. As soon as the temperature setpoint is reached the process pressure is applied. Small leakage leads to a pressure drop over time. When a critical value is reached, the pressure is automatically adjusted by the imprinter.

Obducat NIL-2.5 Nanoimprinting tool A nanoimprinter "NIL-25-OB-HT-PL-LW-UV" from Obducat, Sweden was used for all imprints and transfer prints performed in this thesis. Using this device, it is possible to process multiple samples in parallel or single wafers up to 2.5 inch diameter. The pressure is applied by compressed nitrogen ranging from approx. 5 bar to about 70 bar. Temperature can be changed through an electric heater within the substrate chuck up to 250°C. Compressed air is used for cooling. Additionally, liquid nitrogen can be utilized for a faster process if the machine reservoir is filled before the process (this option was only used when multiple processes were executed since the filling of the reservoir takes longer than a single air-cooling step). The imprinter also features a UV exposure unit, where samples are exposed from the top during an imprint process. All settings can be managed by a computer-controlled user interface, which also records the process parameters. Figure 3.3(b) shows a typical thermal imprinting process.

3.1.3 Nano-transfer printing

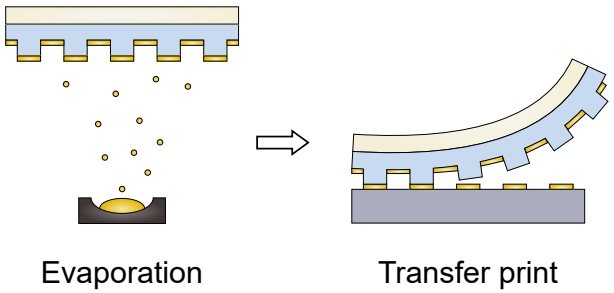

Figure 3.4: Schematic overview of a nano-transfer print process. The ready-to-use stamp is coated with a thin metal layer in a physical vapor deposition (PVD) process. The stamp is brought into intimate contact with a receiving substrate. Upon the stamp release, only the metal layers on top of the stamp protrusions stick to the target substrate. Reprinted from Nagel et al.[13] with the permission of AIP Publishing.

Nano-transfer printing (nTP) is a promising high-resolution technique to directly produce patterned metallic films at the nanoscale on different kinds of substrates without the need for conventional lithographic methods. Here, the pattern is initially defined on a stamp as a 3D-relief structure. After metal deposition on the entire stamp area, its relief is brought into intimate contact with the target substrate (figure 3.4). If the adhesion of the metal film towards the substrate is stronger than towards the stamp, the film will adhere to the target substrate upon release of the stamp. Consequently, nano-scale metal structures can be easily defined in a purely additive process. For a successful transfer, the adhesion of the metal to the stamp should be minimal. The stamp is therefore treated with an anti-sticking layer (ASL) self-assembled monolayer (SAM) (section 3.5), which is an essential preparation step. The stamp may consist of a rigid material (e.g. silicon) to achieve high structure resolution in the nanometer range or of a flexible material such as polydimethylsiloxane (PDMS). A flexible stamp has the advantage of easily forming conformal contact with the substrate. A transfer can only take place where contact is established, and flexible material can adapt to minor surface irregularities and dust particles. On the other hand, soft PDMS stamps have a low Young's modulus ($< 1\,\mathrm{MPa}$) and are consequently susceptible to distortions and structural collapse. An approach of fabricating semi-flexible stamps, combining the advantages of both worlds, is presented in chapter 4.

One of the biggest advantages of nTP is the separation of the structuring process from the substrate. The transfer process itself does not necessarily involve high temperatures nor any form of chemistry (e.g., organic solvents, developer solutions, etc.) on the substrate. Thus, it is especially interesting for applications

where harsh conditions should be avoided (e.g., organic electronics).
A more detailed insight into the nTP process and fundamental ideas behind it can be found in chapter 6.

3.2 Metal Deposition

Metal deposition in the presented work was carried out in a high vacuum chamber of a Leybold L560 e-beam physical vapor deposition (PVD) machine. The chamber is pumped down to a pressure below $1 \cdot 10^{-7}$ mbar using a turbomolecular pump. To ensure short pumping times, samples are brought in the chamber through a load-lock having a smaller volume. An electron beam is generated by heating a tungsten filament while applying a high electric field. The electron beam is accelerated to high kinetic energy and directed towards the evaporation material. Several crucibles with the containing metal sources are available (in most cases, gold and titanium are used). The metal is heated by the e-beam, causing it to melt or sublimate. The resulting vapor can then be used to deposit thin solid films on the substrates gradually. The rate at which atoms reach the substrate surface depends on the source temperature, which can be adjusted by the strength of the e-beam. The layer growth is typically between 0.3 Å/s and several nm/s, which is constantly monitored by an oscillating quartz crystal. In the presented work, if not mentioned otherwise, gold layers were evaporated at a rate of 3 Å/s and a pressure of $1 \cdot 10^{-7}$ mbar, whereas titanium layers were evaporated at a rate of 1Å/s and a pressure of $6 \cdot 10^{-8}$ mbar. Deposition time is controlled by a mechanical shutter, which is opened after the desired evaporation rate is reached. Substrates were usually fixed upside down on a special specimen holder. For lift-off and nTP purposes, the samples were attached flat with respect to the source. For contact purposes (especially on rough or pre-structured samples), the samples should be attached tilted with a rotating specimen holder to cover also vertical sidewalls of the sample surface.
Water vapor preexisting in the chamber or outgassing of the samples can negatively affect the metal deposition by either causing collisions with the metal atoms or by leading to oxidation if non-noble metals are used. This oxidation (e.g., when titanium is being used) can lower the evaporation pressure compared to inert metals, as it removes oxygen out of the vacuum chamber. As a consequence, the actual deposition (by opening the shutter) of non-noble metals like titanium should only be performed when the pressure is stabilized after a short period of time. To minimize these effects, the sidewalls of the chamber are cooled

with liquid nitrogen causing possible water vapor to freeze out.

3.3 Plasma etching

A plasma etcher is a tool to generate plasma from process gas by using microwave radiation. This gas can be inert (e.g., argon) or chemically active like oxygen. The formed ions and radicals fill the reaction chamber and eventually hit the substrate surface, where they can undergo a chemical reaction causing chemical etching and, to some extent, also physical etching. In this thesis, mostly oxygen is used to clean substrates from organic contaminations and to activate surfaces by the generation of hydroxyl (-OH) groups, which facilitates the adhesion to polar polymers for coating processes. The plasma can also be used to etch into organic polymer layers (e.g., to remove residual layers of NIL resists, when reactive ion etching (RIE) is not applicable). Due to the undirected ion generation, the etching behavior is isotropic and thus only reasonably applicable for complete removal or very thin layer etching of structured resist, otherwise, it would change the pattern by lateral etching of individual structures. The etching is highly selective as the treatment does not affect non-oxidizing materials, thus a process executed too long or intense may not be critical.
For this thesis, a Q150 plasma system from "Alpha Plasma" was used, which works with rf-radiation at 2.45 GHz with adjustable power between 50-1200 W.

3.4 Reactive-ion etching

Reactive-ion etching (RIE) is a special type of a dry-chemical etching process. It is carried out in a chamber which is evacuated to a pressure of $1 \cdot 10^{-6}$mbar and then flooded with one or several process gases. A plasma is formed by a strong electromagnetic field, which is generated with a frequency of 13.56 MHz. The oscillating field ionizes the process gas molecules by stripping them off electrons. Due to the electric field, these electrons are removed from the plasma and will cause a self-bias effect when hitting the substrates. The now negatively charged substrates will lead to an acceleration of the positively charged process gas ions towards themselves and thus get bombarded by these high-speed ions. The kinetic energy of these ions causes physical etching while their chemical reactivity can also etch the surface chemically. Due to the high velocity and mainly vertical movement of the ions, RIE can create very anisotropic etch profiles. For nanoimprinting, anisotropic etching is especially important when removing resid-

ual layers of the imprint polymer, since any lateral etching would lead to a change of nanostructure width or even completely remove the pattern when deep etching is needed.
A Plasmalab 80 from Oxford was used during this work. Lithographic resists are usually purely organic material, and thus RIE with oxygen plasma is performed for their removal, while for silicon or silicon oxide etching, a combination of fluorinated gases (SF_6 and C_4F_8) are used. Details on the process parameters can be found in chapter 5.

3.5 Anti-sticking layer

An anti-sticking layer (ASL) is used to lower the surface free energy of a stamp or sample surface. In the presented work silicon-containing materials are used. Thus, the ASL needs to have a silicon-bonding molecular end-group. Typically a silane group is a suitable candidate. This bonding group (see also figure 3.5 (a)) has the ability to form a durable covalent bond to silicon if its surface is terminated with hydroxyl (-OH) groups. The functional group, on the other end of the molecule, can be a binding one to different types of materials making the molecule rather a coupling agent. For anti-sicking purposes, a heavily fluorinated tail group is commonly used. Perfluorooctyltrichlorosilane (PFOTS) (figure 3.5 (b)) as a suitable ASL molecule was chosen, where the chlorosilane group has one of the strongest bonding properties to silicon surfaces, and the fluorinated tail group has a Teflon like character (in principle it is a basic Polytetrafluorethylen (PTFE) chain). The ASL molecule will bind to the hydroxyl groups of the -OH terminated surface by forming hydrochloric acid molecules. As the chlorosilane group reacts heavily with water (vapor), the ASL should be stored under dry conditions and in the best case in a nitrogen atmosphere. However, a reaction mechanism including an intermediate step was reported where PFOTS gets hydrolyzed in the presence of water vapor followed by an interfacial condensation and polymerization reaction between the hydroxyl group of the substrate and the now formed silanol group[14]. As a consequence, the presence of a small amount of water vapor in the reaction chamber (a desiccator is used here) may favor better ASL properties.

The ASL process is based on the formation of a self-assembled monolayer (SAM). Since the molecule can only bind to the substrate surface, the Teflon tail group will prevent the formation of multilayers when fully covered with PFOTS.

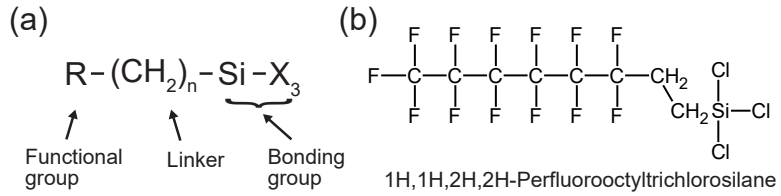

Figure 3.5: (a) basic structure of an anti-sticking molecule. (b) used molecule in this thesis.

This is a requirement for nanoimprint stamps as nanostructures would be overgrown, causing sharp edges to soften. The PFOTS molecules may still condense on the already formed SAM, but without a covalent bond, they are only loosely bound and can be easily removed later on.
Silanes can be applied to substrates under dry conditions by chemical vapor deposition methods in a desiccator. These methods favor monolayer deposition compared to those from the liquid phase. A prerequisite is the high vapor pressure of the ASL, which needs to be above the chamber pressure at room temperature.

The anti-sticking layer treatment was carried out as follows: First, the substrates are cleaned with acetone and isopropanol and exposed to oxygen plasma (200 W for 2 min). This step is needed for the generation of hydroxyl groups on the surface. The substrates are placed above or adjacent to an ASL reservoir in a desiccator. Already one droplet (2 µl) of PFOTS is sufficient for multiple samples. The desiccator is pumped down to approx. 0.1 bar for 20-30 min leading to the evaporation of the ASL liquid and its deposition on all open surfaces. In general, the desiccator and therefore also the substrate temperature should be maintained above 50°C and below 120°C to promote the reaction.
In the presented work, this parallel heat treatment was not carried out but replaced by a subsequent temper step on a hotplate at 130°C for 10 min. This method has been shown to be effective[15]. The heat treatment facilitates not only incompleted chemical reactions but also removes unwanted multilayers of the ASL molecule, which are physisorbed on top of the first covalently bound SAM. In principle, rinsing the samples with acetone and isopropanol as a final step can be performed, but as no benefits were observed, this step was neglected.

3.6 Cyclic voltammetry

Cyclic voltammetry (CV) is the most common technique in electrochemistry (EC) to characterize electrode surfaces. It is a type of potentiodynamic EC-measurement. The experiments in this thesis are designed as a three-electrode system (figure 3.6).

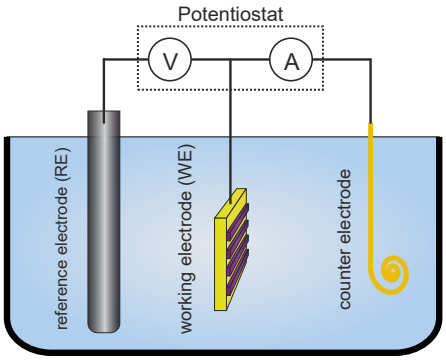

Figure 3.6: Sketch of a three-electrode setup. A potentiostat applies a potential at the working electrode with respect to the reference electrode. The current, which flows between the working- and the counter electrode is being measured.

Typically a triangular voltage is applied between the investigated electrode (working electrode (WE)) and the reference electrode (RE). Simultaneously, the current flow between the WE and the counter electrode is measured. This results in a voltage-current plot, which shows characteristic features depending on the electrochemical processes taking place at the WE-electrolyte interface (shown in figure 7.6). With this measurement technique, it is possible to characterize ad- or desorption and oxidation or reduction processes precisely.

4 Working stamp fabrication by imprint master mold replication

4.1 Introduction

Nanoimprint lithography can be separated into two parts: First, the technology of fabricating imprinting molds (or stamps) and second, the transfer of nanostructured shapes using their patterned surface. Even though at first glance, the imprinting step seems to be the more important one, the foundations for a successful process are already laid in this first step of stamp fabrication. Most of the stamp properties have a decisive impact on the following procedures and may also vary for different applications. This chapter will highlight the requirements for nanoimprint stamps for most common applications and will describe the replication process developed during this work to overcome most limitations of standard silicon templates. Parts of this chapter have already been published and taken from Nagel et al.[16]

Table 4.1: Requirements on stamp material and fabrication process.

Pattern	Fabrication
High resolution	Fast
High aspect ratio	Inexpensive
Large Area	Simple & defect tolerant
Properties	**Processing**
Flexible	Clean/Non-contaminating
Hard (high young's modulus)	Bio-compatible
Temperature stable	Non-hazardous
Transparent	Surface modification possible (e.g., ASL)
	Reusable

High resolution is the key feature of a nanoimprint stamp. Not restricted by the diffraction limit of light like in optical lithography, the structures on a nanoimprint stamp can be as small as they are still mechanically stable. Already in the

early days of nanoimprinting, a sub 10 nm imprint was demonstrated by Chou et al.[17]. Here, a hard material like silicon offers excellent properties for minimal feature size and is only limited by the initial patterning technique. The height of the protrusions may have a direct influence on direct molding applications[18,19]. However, for imprinting polymer masks, taller structures play a subordinate role but can result in higher process tolerances during subsequent etching or metalization steps due to a thicker polymer layer. In combination with small lateral dimensions, these high aspect ratio structures can, however, have stability issues that are discussed at the end of this chapter.

Imprint molds are usually made from silicon[17], dielectric materials (e.g., silicon dioxide or silicon nitride[20]), metals (e.g., nickel[21]), or polymeric materials with a sufficiently high young's modulus[22]. Common features of these different materials are that they are hard and have high mechanical strength. While a hard material offers the highest resolution and structure stability during imprinting, the brittle character of such materials (especially crystalline ones) tends to be sensitive to surface defects like dust particles as they can not adapt to such impurities. Therefore, a flexible stamp approach would be advantageous.

Another issue in nanoimprinting is stamp alignment on the substrate. While alignment on the nanometer scale needs special tools and techniques, even micrometer alignment accuracy is hard to achieve with standard silicon stamps: As they are opaque for light in the visual range, an alignment system based on infrared light would be necessary. A better approach is the use of already transparent stamps, which are also needed if UV-imprinting is being performed.

As a starting point of all patterning processes, the initial imprint mold has to be manufactured. Typically, a free to choose layout can only be written with some sort of high-end, cost-intensive lithographic methods (e.g., e-beam lithography). Yet, this only allows small patterned areas when multiple stamps are fabricated. Otherwise, the costs for the molds increase tremendously. While silicon stamps with 300x300 μm^2 were used at the beginning of this thesis, for electrochemical applications, this area is just too small to obtain evaluable and reliable results. Consequently, a better approach is to use a large area silicon stamp as a master template for replication of a daughter or working stamp based on a cheaper and preferably more flexible material. While this master can be cost-intensive as well, as it then serves as a template for multiple replication processes, the initial effort is capitalized more efficiently.

A widely used material for this purpose is Polydimethylsiloxane (PDMS), a silicon-based organic polymer[23,24]. It is chemically inert and transparent in the

visible spectrum. To verify its capabilities as an imprint stamp material, Sylgard 184 from Dow Corning was used, which comes as base PDMS and a curing agent. When mixed in the right ratio, it can be drop-casted or spin coated on a master stamp and hardens over several hours. At elevated temperatures of 90°C, this duration can be reduced to 15-20min[25,26]. For micro-contact printing and imprinting of larger structures above 300 nm, this material can be used. For smaller structures, lateral collapse occurs using PDMS as it has a rather low young's modulus of 1.7 MPa[26]. Haeberle (Institute for Nanoelectronics, Technical University Munich) showed in his work that in addition to this problem, roof collapse can occur for structures with interdistances in the μm range[16,27]. To overcome these limitations, the industry has developed and uses h-PDMS and x-PDMS, harder and more expensive versions of standard PDMS. Yet, in addition to these mechanical instabilities, it was found that the mentioned curing duration is too high for mass production. While a stamp can be reused for imprinting polymer layers, this fails for nano-transfer printing. Remaining metal on the stamp can significantly impede the establishment of conformal contact in subsequent transfer attempts and thus prevent a successful transfer of the metal film.
Instead, in the following, a method to use OrmoStamp® (micro resist technology GmbH, Germany), a commercially available UV-curable, solvent-free, organic/inorganic hybrid polymer from Micro resist technology GmbH, Berlin, is presented as a viable, cost-efficient material for stamp replication. OrmoStamp® has initially been developed for ultraviolet nanoimprint lithography (UV-NIL) as an alternative to the use of expensive quartz wafers and is suitable for replication of silicon master templates with structures in the low nanometer range[22]. Once cured, the optical transparent replica has a Young's modulus of 650 MPa[28], and its surface can be modified with the same chemistry (PFOTS) as silicon to decrease its surface free energy.

4.2 Stamp replication process

The OrmoStamp® replication process is based on an adapted UV-NIL process. For reasons described in Section 4.3.1, the fabrication of working stamps comprises two successive replication processes: (1) the fabrication of a negative replica (daughter) from a master mold based on silicon, and (2) the fabrication of working stamps by again replicating the negative intermediate daughter stamps using the identical process (figure 4.1).

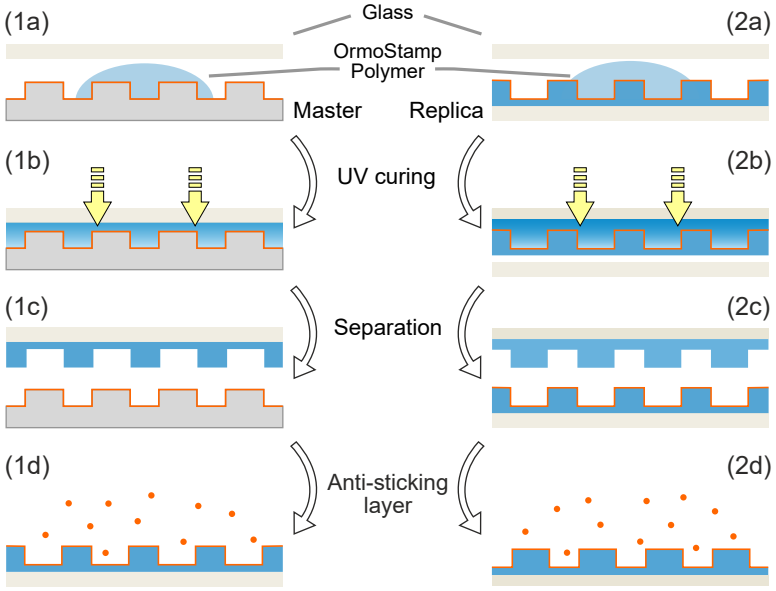

Figure 4.1: OrmoStamp® two-fold, adapted UV-NIL replication process. First, a negative replica of the silicon master is cast, which then serves as a template to replicate the positive working stamp.

4.2.1 Silicon master mold preparation

The silicon masters used in this thesis were ordered from IMS Chips, Stuttgart and were fabricated by e-beam lithography with a subsequent reactive ion etching step to convert the written pattern into a 3D relief. As a first step, the silicon master is coated by an anti-sticking layer (ASL) to reduce lift-off forces during the separation of the replica from the master. Before coating, the silicon surface is cleaned with acetone and isopropanol and then exposed to oxygen plasma (200 W, 2min, 100 sccm, 100 Pa). This is, first of all, an additional cleaning step by ashing all remaining carbon-based contaminations (see section 3.3), and second, it will *activate* the silicon surface by functionalizing it with hydroxy groups, thereby facilitating a chemical reaction with the ASL molecule during the following deposition.

The activated silicon master is placed in a desiccator together with a droplet of perfluorooctyltrichlorosilane (PFOTS) and pumped down to approx. 0.1 bar for 20 min. The ASL evaporates and homogeneously fills the desiccator volume and, as a result, covers all exposed surfaces. The Si-Cl end group of the ASL will react with the activated silicon surface by the elimination of hydrochloric acid. When fully covered, the perfluorooctyl end group will hinder further reactions, which makes this treatment a self-assembled monolayer process (SAM). Afterward, the master mold is removed from the desiccator and placed on a hot plate at 150°C for 15 min. On the one hand, this will facilitate the reaction of not yet bound PFOTS molecules in direct contact to the silicon surface, and on the other hand, it removes unwanted physisorbed multilayers of this molecule which have been condensed on top of the formed ASL during evaporation. The master mold is now ready for the replication process, and the ASL is stable for hundreds of copies. If a noticeable degradation of the ASL occurs. This treatment can be refreshed by first cracking the ASL in oxygen plasma and redoing the same procedure. In this work, this was done only once a year. While a degradation was not observed, it was carried out preventively to maintain stable results and identical OrmoStamp® copies.

4.2.2 OrmoStamp replication process

Preparation

As mentioned above, OrmoStamp® was chosen for stamp replication, which was specially designed as a cost-effective alternative to quartz stamps. This polymer is a UV-curable resin and can be drop-cast directly on top of the structured area of the master. Due to a rather thin final layer of this polymer (around 30μm) after casting, it is still flexible after hardening, thus it must be backed by a glass carrier.
For the first negative copy of the silicon master mold, a 500 μm thick 2-inch borosilicate glass wafer (D 263® T eco - Schott AG, Germany) was chosen. As this first copy again is used for the fabrication of up to hundreds of working stamp copies, this ensures an easy to handle and long-term stable daughter stamp. For the working stamps, a microscope cover glass 18 mm in diameter and 100 μm thickness is used to retain the flexibility of the polymer layer.

Cleaning and Activation

The microscope cover glasses are not intended for cleanroom use, thus their cleanliness doesn't fulfill prime wafer grade compared to the borosilicate glass wafers. They are shipped in 100 pcs per box without separating papers and are sometimes covered by small glass particles caused during the manufacture cleavage step. Thus, they must be specially cleaned before usage. As an upside, they are very inexpensive (∼0.05€ each). As a first step, the coverslips are rubbed with a cleanroom tissue and isopropanol to remove larger particles from their surface. This step is not necessary for borosilicate glass wafers. Then, all backing glasses are cleaned with acetone and isopropanol in an ultrasonic bath for at least 5 minutes. This was carried out with a custom-made sample holder cleaning up to 50 pcs in a single cleaning step.
After dry blowing with pressurized nitrogen, the backing glasses are exposed to strong oxygen plasma (600 W, 6min, 100 sccm, 100 Pa). This step has a considerably higher intensity compared to the activation step during the anti-sticking process (200 W, 2min, 90 sccm, 100 Pa). It was found that too mild plasma results in insufficient adhesion properties during the subsequent coating step of the adhesion promoter OrmoPrime08®. This could lead to a dewetting effect during spin coating preventing the formation of a closed film or it could result in a cracked layer after hardbake.
OrmoPrime08® is an adhesion promoter solution based on organofunctional silanes. It will enhance the adhesion of OrmoStamp® resin to various substrates in particular glass wafers and coverslips. The cleaned and activated glass substrates are covered with a droplet of OrmoPrime® polymer, and a thin layer is formed by spin coating (4000 rpm, 60s, 1000 rpm/s) followed by a hardbaking step at 150°C for 5min. This will result in a film thickness of about 130 nm (according to manufacturer guidelines). The exact thickness is not of great importance as the final OrmoStamp® layer will be with 30 μm height, thicker by orders of magnitudes. On this basis, an additional filtration of the primer before use isn't needed (OrmoPrime® is shipped with a filtration level of 0.1 μm).

Structure replication

Structure replication is achieved by drop casting. A defined amount of the OrmoStamp® resin is placed centered on the master. OrmoStamp® is stored in a fridge at 5°C in order to preserve its shelf life. At this temperature, the polymer is highly viscous, which is disadvantageous for drop casting. Therefore, a small portion is allowed to warm up to room temperature. If air bubbles are visible in

Table 4.2: Amount of OrmoStamp resin needed for a complete filling of different stamp sizes resulting in a layer thickness of $\sim 30\,\mu m$.

Stamp area	OrmoStamp Volume
working stamp (18 mm diameter)	5-7 μl
squared glass backing (3x3 cm^2)	30 μl
2-inch wafer (50.8 mm diameter)	70 μl

the resin, they must be removed by carefully dipping a fresh glass pipette close to the inclusion. In most cases, this will automatically remove the bubble by sucking in a small amount of OrmoStamp®, including the bubble. Then, the chosen glass backing is placed carefully on the formed droplet (Fig. 4.1 (a)). Without applying any pressure, the resin spreads between master and glass to form a thin layer and fills up any gaps by capillary forces. The final layer thickness is determined by the initial volume of the OrmoStamp® droplet and the surface area of the stamp. Typically, a layer thickness of $30\,\mu m$ is convenient for both retaining the semi-flexible character while reducing the spreading speed of the polymer (see section 5.2). For that reason, a well-defined amount of resin has to be applied in this step. A multi-step pipette was used (HandyStep S, Brand GmbH + Co KG, Germany) for this purpose. Here, it is possible to define volumes starting from $2\,\mu l$ and $1\,\mu l$ increment with a measured accuracy of 2.4% and a measured coefficient of variation of 3% in H_2O dist. (according to manufacturer datasheet) for a typical volume of 5-7 μl for working stamp fabrication (Table 4.2). It is possible to use one filling for up to 18 stamps. Yet, the main reason to favor a multi-step over a single-step pipette is the rather high viscosity of the OrmoStamp® polymer. When refilling the tip with the resin or when dispensing it later, OrmoStamp® tends to stick to the outer tip surface due to its specially tuned wetting abilities, preventing getting a defined volume in the first dispensing stroke. As this dead volume then stays constant throughout one tip filling a multi-step pipette is necessary to avoid this problem. Full spreading takes some seconds for small working stamps and can take up to 5-10 min for full wafer-scale replication. To decrease filling time, a thicker final layer can be chosen.

When the resin is fully spread, it is exposed to UV light from a mask-aligner (Hg lamp, 350 W, $7mWcm^{-2}$ at 365 nm [i-line]) for 120s to initiate the curing process (Fig. 4.1 (b)). The exposure dose for full curing is around $1000mJ/cm^2$. OrmoStamp® is sensitive to UV broadband. While already the i-line dose after 120s exposure time is around $840mJ/cm^2$, the broadband dose is far above the required level. Applying a UV overdose during curing does not affect its proper-

ties. Afterward, the glass plate, together with the cured polymer, can be carefully released from the master by lifting the glass with a thin razor blade (Fig. 4.1 (c). Typically, a short flood exposure for 20s with the structured surface on top is performed after demolding to increase mechanical and thermal stability. The cured replica stamp requires a hard bake for 30min at 130°C on a hot plate. This step should be started on a cold hotplate with a low heating ramp, and the cool down at the end should also be slow to minimize thermal stresses. Otherwise, the delamination of the cured resin from the glass backing can occur.
As a final step, replicated stamps are coated with a PFOTS SAM as described above (Fig. 4.1 (d)). Compared to the standard procedure, only a mild oxygen plasma is applied (100 W, 1min), since too much power or long durations will degenerate the cured polymer. The efficacy of this SAM treatment was checked by means of a static water contact angle (CA) measurement: the coated surface exhibits a CA of ∼110°, while an uncoated surface has a CA of ∼80° [27].

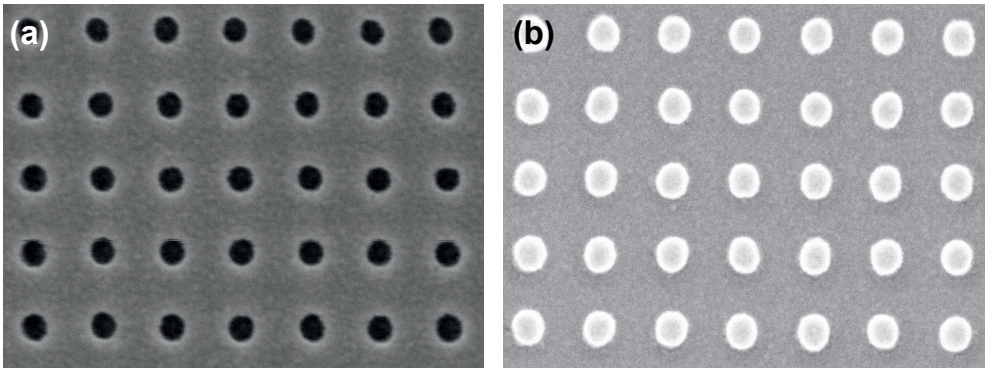

Figure 4.2: SEM images of (a) a negative OrmoStamp® copy of a silicon master mold with 75 nm pillars (b) positive working stamp fabricated using the negative stamp from (a).

This negative replica can then be used for imprinting or transfer printing applications or as a template to produce positive working stamps following the same procedure (figure 4.2). The final working stamp is backed by a 0.1 mm thin microscope cover glass to retain the flexibility of the polymer layer. This way, a transparent, semi-flexible, defect-free, identical copy of the original silicon stamp is obtained. During this work, typically up to a hundred working stamps from a single negative replica of a silicon master were reliably produced, multiplying up the lifetime of a cost-intensive silicon master tremendously. Note that with the process described here, stress on the silicon master is minimal since no pressure or temperature is applied during the master replication. This way, it is possible to separate high imprint pressures, including possible particle contaminations from

the master. Although OrmoStamp® working stamps can be used several times and be cleaned with acetone and isopropanol, due to the easy fabrication, they were typically used only once.

4.3 Ormostamp properties

4.3.1 Shape retention and shrinking

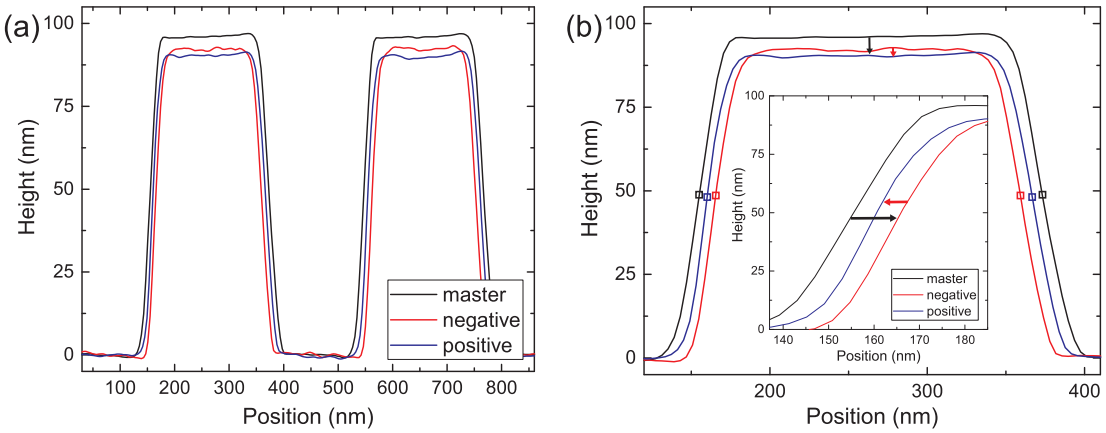

Figure 4.3: AFM measurement of a master stamp with 200 nm lines and 400 nm pitch and its OrmoStamp replicas. A constant height shrinkage occurs for every replication step, while the line width increases again from the negative copy to the positive working stamp. The marked positions in (b) define the points of line width extraction.

The most important requirement for a nanoimprint stamp replication process is the shape retention of the nanostructures. Many applications of this patterning technique need a resolution in the nanometer range, thus any changes in size and shape during replication might directly affect all following results in the experiment or device fabrication. The method presented here includes a twofold replication of a master mold and additionally a final transfer print or imprint. Therefore, it is important to examine how the dimensions change throughout all copying steps compared to the original ones. The shape retention of the nanostructures after the UV-curing step during the replication process is the first critical point, thus it was both checked with AFM and SEM. According to the manufacturer, a volume shrinkage of 4-6% takes place during this step. This is obviously unfavorable for a high lateral dimension accuracy. Using AFM measurements in tapping mode, the nanostructure step-height, pitch and line width on the silicon master and on its copies were measured and are summarized in Table 4.3, Table 4.4, and Table 4.5.

Here, a master with lines equally sized in width and inter distance is used.

Table 4.3: UV-curing induced shrinkage (height).

	Master	Daughter	Working stamp
Height (nm)	94.1±1.6	90.1±1.1	87.0±2.4
Shrinkage (nm)		4.0±1.9 (-4.3%)	3.1±2.6 (-3.4%)

Table 4.4: Lateral shrinkage (pitch).

	Master	Daughter	Working stamp
Pitch (nm)	394.3±2	394.3±2	394.5±2
Shrinkage (nm)		0±2.8 (0.0%)	0.2±2.8 (0.0%)

Table 4.5: Lateral line shrinkage (width).

	Master	Daughter	Working stamp
Width (nm)	218±1.4	193±2.6	208±1
Shrinkage (nm)		-25±18 (-11.5±8%)	+15±9 (+7.8±4.7%)

The shrinkage is calculated regarding the corresponding parent stamp dimensions. 200 nm lines with 400 nm pitch (200 nm inter distance) are exemplarily shown in Figure 4.3. As can be seen, the initial height of the silicon master pattern of 94.1± 1.6 nm decreases after the first OrmoStamp® copy to a value of 90.1 ± 1.1 nm, which corresponds to shrinkage of -4.3%. The final working stamp has a structure step-height of 87.0 ± 2.4 nm (-3.4%). The shrinkage of both steps is in good agreement with the expected value of around 4%. If the working stamps are used for nanoimprint, this height reduction is particularly relevant. The initial spin-coated imprint polymer layer thickness has to be adjusted accordingly, or this shrinkage has to be respected in the master fabrication with an additional design-wise implemented height. For transfer printing, this plays a subordinate role, since the height is only important to prevent a metal overgrowth of the structures during evaporation.

While the height measurements reflect the actual height of the structures quite precisely, the width of the lines appears wider than their actual lateral dimensions. Since the structures are already very small, at such small and steep edges, the shape of the AFM tip itself can't be neglected anymore. In fact, the measured curve is a superposition of the stamp structure and the tip geometry creating an artifact in the measurement. Here, the side of the probe will cause a broadening of features in the image. If the probe is much smaller than the features of the images being measured, the probe-generated artifacts will be minimal, and the dimensional measurements derived from the images will be accurate. As a result, it is difficult to measure the absolute width of high aspect ratio structures precisely. Yet, it is possible to measure different values quite accurately as the

broadening is a fixed value due to a fixed tip geometry. The measurement values of absolute and percentage lateral shrinkage shown in Table 4.5 are extracted by that means and related to the line width of the master and the corrected ones of its copies. Some difficulties arise for making a proper evaluation of this measured data: First, the point of data extraction itself has some uncertainties. Due to possible AFM overshoots and rounded edges, the width was not extracted as the distance between the top edges of a line but rather as the distance between the half-height positions of the AFM measurement (as depicted in Figure 4.3 (b)), which gave most reliable results.
Second, we have a material change between the silicon master and the OrmoStamp® copies. This could lead to a different distance of sample surface and AFM probe in tapping mode. While height measurements are not affected by this problem, since this change would be identical for all horizontal surfaces and thus is deducted equally when calculating the absolute height, for lateral measurements, in contrast, the effect takes place on both sides of a line step thus sums up to twice the amount. So, the shrinkage of a copied stamp while changing from silicon to OrmoStamp® material is larger than in the second copying step as can be seen in Table 4.5. Additionally, if the widths of the initial master line structures are not perfectly identical to their inter distances, this discrepancy will be inverted during a single copy process, since the actual width of a line of a negative copy only corresponds to the interdistance of two lines of the parent stamp. This uncertainty was estimated using high-resolution SEM images and AFM by comparing a negative daughter stamp with imprinted lines using a working stamp. An uncertainty of max. 6 nm was found for 200 nm wide lines, and it was included as a systematic error during error calculation. In Figure 4.3 (b) it can be seen that structures of the first negative OrmoStamp® copy have a smaller width compared to the silicon master due to the shrinkage and, consequently, a larger inter distance as the pitch stays constant (see Table 4.4). The silicon master has an initial line width of 200 nm. Yet it was measured to be 218 ± 1.4 nm due to the measurement artifacts and problems described above. The features of the first negative OrmoStamp® replication have a width of 193 ± 2.6 nm which means a reduction of -25 ± 18 nm ($-11.5 \pm 8\%$) (here, the uncertainty of material changes and initial width/inter distance discrepancy is included).
In contrary, this unwanted behavior is relativized by second-time replication in order to fabricate the positive working stamp. The now widened lines (due to this widened inter distance) shrink again by the same percentage but are still wider than the protruding lines of the negative parent stamp and consequently

turn back to almost the original value of the silicon master. The measurement of the final positive working stamp reveals this effect (Fig. 4.3). The width was measured to be $208nm \pm 1\,\text{nm}$, meaning that this is now a widening of the lines of about $15nm \pm 9\,\text{nm}$ ($+7.8 \pm 4.7\%$). With respect to the error bars, these values are reasonable compared to the calculated shrinkage percentages obtained by the height reduction measurements. This is one of the reasons for the developed two-fold replication process in this work. As the height reduction can be taken into consideration throughout the patterning process, lateral shape retention is most important and can be achieved by this procedure.
Shrinkage usually is isotropic. Yet, as the closed base film is fixed due to the glass backing, it only affects free-standing parts of the stamp. It can be assumed, as the base of each line must also be fixed in width, that this shrinkage additionally leads to a deviation from perfectly vertical sidewalls. However, this effect couldn't be measured as it is very small. The shrinkage of the OrmoStamp® base film of $30\,\mu m$ thickness on top of the backing material will induce stress and potentially leads to a bending of the final stamp. When OrmoStamp® was only backed by a thin plastic foil, this bending has been observed. Using the final 0.1 mm thin cover glass, the bending was little to none present. This is the root of the constant pitch for all replicated structures, which are measured and listed in Table 4.4.

4.3.2 Self-cleaning effect

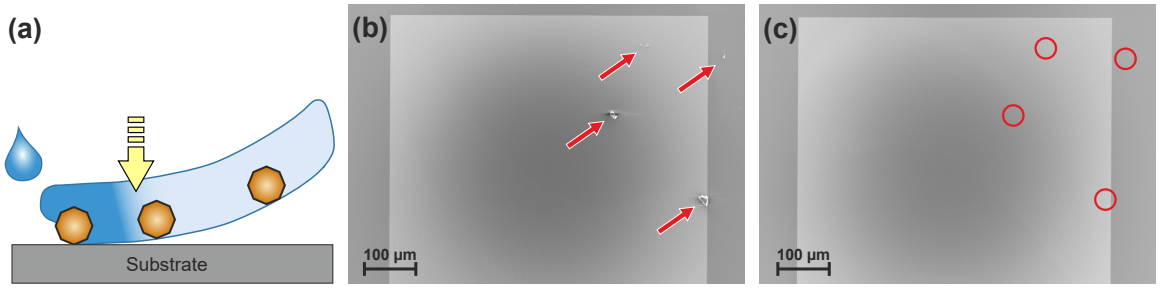

Figure 4.4: (a) Sketch of the self-cleaning effect: Encapsulated contaminations are removed after UV-curing and demolding. (b)+(c) Comparison of a silicon master stamp: (b) before an OrmoStamp replication with particle contaminations (marked by red arrows) and (c) self-cleaned surface of the same master after one OrmoStamp replication. Adapted from [16].

Unlike defects on the target substrates, defects on the silicon master will later be present on each working stamp and, consequently, also on the target substrate. Thus, cleaning of the silicon master stamp is required from time to time where the use of an ultrasonic bath or reactive chemicals might damage the fragile nanostructured surface. A self-cleaning effect was found to take place during

every replication procedure and is explained as follows: The liquid resin encapsulates any dust particles or residual resin during the drop casting, which then are removed from the master surface in the demolding step after the resin is cured. Figure 4.4 shows a nanopatterned silicon wafer with contaminations. After only a single OrmoStamp® replication, the surface is completely particle-free. The studied results demonstrate that this is a non-destructive cleaning procedure, which can effectively remove all particles and residual resist from the stamps. It can also be used as an alternative method for substrate cleaning.

4.3.3 Optical properties

After UV-curing, the fabricated stamps are themself transparent in the optical and near UV regime, as depicted in Figure 4.5. Of course, the used glass backing must be UV-transparent in the first place, otherwise the replication procedure wouldn't be possible. At the most prominent emission lines (i-line, h-line, and g-line) of the mercury-vapor lamp used for curing, the transmission for the 400 μm thick quartz wafers (D 263® T eco) is about 90% while the thin OrmoStamp® layer is nearly entirely transparent. This way, the opaque silicon master is not only replicated but also converted into a transparent stamp, which enables optical alignment for device fabrication purposes.

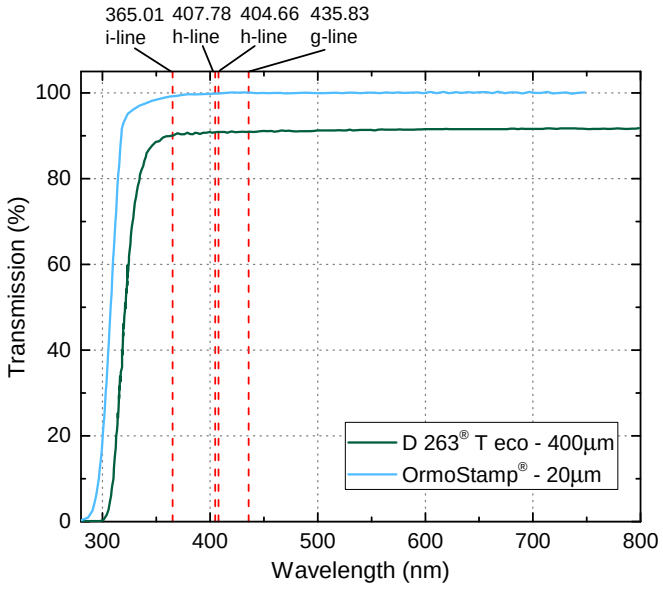

Figure 4.5: Transmission spectra of a cured 20 μm thick OrmoStamp® (micro resist technology GmbH) layer and a 400 μm thick D 263® T eco (SCHOTT AG) backing glass used for negative replicas. The materials are highly transparent at the emission lines of a mercury-vapor lamp. Reprinted with the kind permission of "micro resist technology GmbH", Germany and "SCHOTT AG", Germany [29,30].

4.3.4 Structural limitations of stamp patterns

Minimizing the feature size of the stamp will eventually reach a limit. The resolution of the OrmoStamp® polymer is at the molecular level and thus will not limit stamp fabrication. The mechanical properties of the stamp material and the imprint structure geometry instead have the biggest influence on the smallest possible structure size. Especially during imprint and transfer print, where typically high pressures (30 bars in the standard process) and temperatures (above 200°C) are applied, the mechanical stability is an issue, and it could result in distortions. Finn et al. discussed stamp geometries and limitations using a theoretical model of Hui et al.[26,31,32] In this section, the stamp failures relevant for this work are summarized (Equation (4.1)-(4.3)).

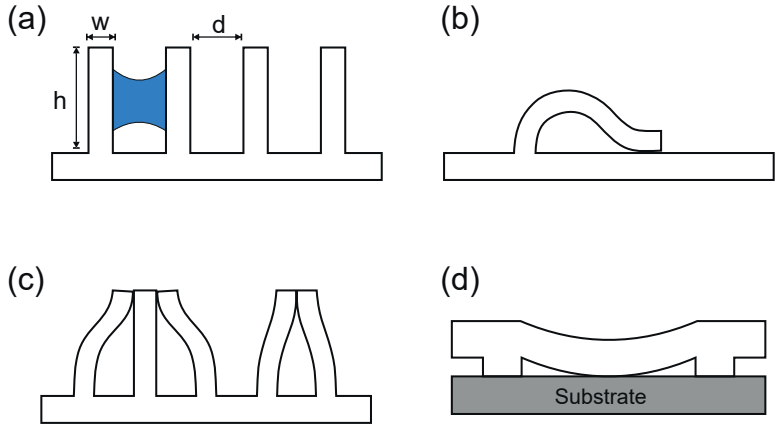

Figure 4.6: Possible layout constraints by nanostructure deformation on the stamp. a) Schematic of a non-distorted stamp b) Ground collapse of a single structure c) Lateral collapse of two or more structures d) Roof collapse of the base layer.

Condition for lateral collapse:

$$\sqrt{\frac{d}{w}} < \frac{h}{w}\left(\frac{4\gamma}{3E^{*}w}\right)^{1/4} \tag{4.1}$$

Condition for lateral collapse of equidistant lines with a pitch twice the width of a line ($w = d$):

$$\frac{h}{w} = \left(\frac{3E^{*}w}{4\gamma}\right)^{1/4} \tag{4.2}$$

Condition for roof collapse:

$$\frac{2\sigma d}{\pi E^* h}\left(1+\frac{b}{d}\right)\cosh^{-1}\left[\left(\cos\left(\frac{d\pi}{2\,(d+b)}\right)\right)^{-1}\right] < 1 \tag{4.3}$$

The sketch in Figure 4.6 shows typical failures of high aspect ratio structures. Ground collapse (Fig. 4.6 (b)) is the only possibility, which can occur if the distance of two individual structures is large than twice their height. Here, the adhesion forces between its surface area and the base layer are larger than the restoring forces of the bent structure. However, this has not been found to happen with our stamps, as the needed aspect ratios must be very large. Zhang et al. observed experimentally ground collapse to happen for soft PDMS material with a structure aspect ratio of 18[26]. The main issues are the lateral collapse of adjacent structures and roof collapse between protrusions of very large distance (Fig. 4.6 (c)+(d)). The first type can be calculated if Equation 4.1 is fulfilled for the special case of a line stamp or squared pillars. It includes the material parameters Young's modulus E, poison ratio ν (both combined as $E^* = E(1-\nu^2)$), surface energy γ, and the geometrical parameters height h, width w, and inter distance d. In this work, line stamps are used with a pitch twice the width of a line ($w = d$). Using these restrictions, the equation can be simplified to express the critical aspect ratio above which lateral collapse occurs (Equation 4.2).
It is now possible to calculate the minimal feature size of our line stamps assuming a typical height of 100 nm and using the OrmoStamp® material parameters $E = 650$ MPa and $\gamma = 41 mN/m$. The limits here are given by $d = w = 25.7$ nm corresponding to an aspect ratio of $h/w = 3.89$. The surface energy can be reduced to $\gamma = 11 mN/m$ by applying an anti-sticking layer on the surface, resulting in a minimal line width of $w = d = 19.8$ nm and an aspect ratio of $h/w = 5.06$.
A comparison of different stamp materials can be found in Table 4.6. The critical aspect ratio is given for 200 nm wide lines with 400 nm pitch.

The limits were tested with a 35 nm line stamp of 110 nm height. Note, while this configuration is stable in theory, the young's modulus of the OrmoStamp® polymer was reduced by incomplete UV-curing during stamp fabrication. An AFM image of this stamp is given in Figure 4.7. The lateral collapse of some of the lines is clearly visible. With complete curing, the lateral collapse was not present, as expected. While the minimal feature size using silicon stamp is 9.7 nm for this specific parameter set (same height) as above with the much higher young's modulus of silicon $E_{si} = 130$ GPa and $\gamma = 63\, mN/m$[34], though

Table 4.6: Critical aspect ratios for different stamp materials. Exemplarily shown for 200 nm lines with 400 nm pitch. This critical ratio is only valid for the chosen dimensions and may vary for other parameters. *Depends on crystal orientation[33].

	Ormostamp[28]	Ormostamp \w ASL	Silicon[33,34]
Young's modulus (E)	650 MPa	650 MPa	130 GPa*
Surface energy (γ)	41 mN/m	11 mN/m	63 mN/m
Critical aspect ratio (h/w)	6.5	9.0	21.9
	PDMS[26,35]	Kapton	
Young's modulus (E)	1.7 MPa	2.5 GPa	
Surface energy (γ)	25 mN/m	37 mN/m	
Critical aspect ratio (h/w)	1.7	9.3	

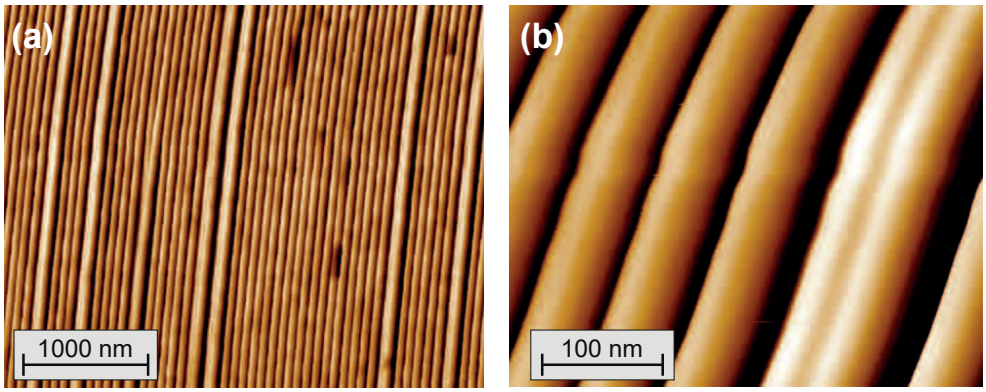

Figure 4.7: AFM image of a partial lateral collapse of 35 nm lines with 110 nm height and 70 nm pitch for an incompletely cured OrmoStamp replicated stamp. The height scale ranges from black: 0 nm to white: 110 nm.

the replicated OrmoStamps combines the best properties of both worlds: semi-flexibility with acceptable hardness.

Collapse can only occur when a contact of two adjacent lines is forced by some sort. This can happen during imprinting or transfer printing, where high pressures are applied, which could result in shear forces. Yet in most cases, the contact can already be triggered by the wetting of the surface. Small liquid droplets can cause high forces due to surface tension during evaporation, as depicted in Figure 4.6 (a)). Consequently, a wetting of the surface has to be prevented for critical configurations. Especially after the UV-Curing step, this has to be considered, as the full hardness of the material is only achieved after the hardbaking step. Additionally, an ASL lowers the risk of collapse.

Roof collapse (shown in Fig. 4.6 (d)) is relevant for large separations between patterned areas or large distances between structures. It is particularly relevant for nTP where roof collapse does lead to unwanted metal transfer. Using Equation 4.3 with OrmoStamp® line stamps with 200 nm width and 100 nm height while applying an imprint force of $\sigma = 30$ bar, the critical distance is in the range

of 10 μm, which is orders of magnitude larger compared to the values for the stamps used in this work. Roof collapse is relevant when including large contact pads or several device layouts on one imprint stamp. Here the distances are easily reached, and the problem must be solved with supporting posts in the intermediate areas[27].

4.4 Summary

An imprint mold replication process was developed based on OrmoStamp material. The main advantages compared to conventional working stamps made out of PDMS are the very high feature resolution and the more suitable UV-light curing process of the stamp material on the master mold instead of thermal curing, which results in a highly increased fabrication throughput. Additionally, the avoidance of standard nanostructuring methods like e-beam and UV-light exposure, reactive ion etching as well as any kind of solvents or developers on the substrate during the nTP procedure make this process ideally suited for organic electronics where the organic materials tend to degrade rapidly under the influence of harsh conditions. In summary, this will open up opportunities for a wide range of applications of metal nanostructures in science and engineering, such as energy conversion, sensing on solids and flexible substrates.

5 Nanoimprint lithography for nanostructured device fabrication

5.1 Introduction

In this chapter, a theoretical background of nanoimprint technology is given and process parameters that dominantly influence a successful imprint are discussed. For subsequent etching of the substrate, the patterned resist can directly be used as a mask, while for metal deposition a more advanced method is necessary. For this purpose, a lift-off nanoimprint process is developed by introducing a second resist layer acting as a sacrificial lift-off resist. The fabricated metal nanostructures are characterized in terms of shape retention, morphology, and homogeneity over large areas. Parts of this chapter are reprinted from[13] with the permission of AIP Publishing.

5.2 Fundamentals of nanoimprint lithography

The imprint process is based on a complex squeeze flow of viscous material. With the thin imprint polymer layers used in NIL, a small vertical displacement of the stamp result in a large lateral flow of the polymer.

Assuming, that the polymer film has an initial thickness h_0, while the height of the stamp protrusions is h_p (figure 5.1 (a)). After the polymer completely filled all cavities of the stamp, the thickness of the residual layer is reduced to h_r, which is the remaining polymer film between the substrate and the elevated structures on the stamp (figure 5.1 (c)). When regarding the polymer as incompressible (thus conserving its volume), the residual layer height can be directly deduced from the fill factor ν of the stamp pattern by applying the continuity equation.

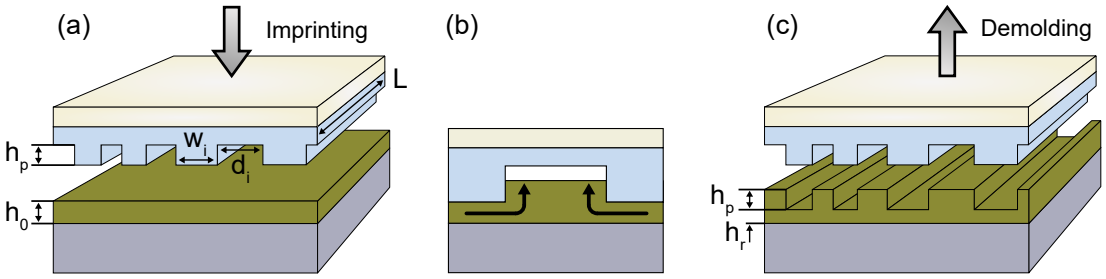

Figure 5.1: Sketch of NIL with the geometrical definitions (a) before imprinting, (b) during imprinting, and (c) after demolding. Resist structuring is achieved by a squeezed flow of thermoplastic or UV-curable polymer.

The fill factor is the ratio of the area covered by the protrusions to the total stamp area.

$$h_r = h_0 - (1 - \nu) \cdot h_p \tag{5.1}$$

This equation is only valid for constant fill factors. Arbitrary layouts result in a locally varying residual layer thickness and thus in a challenging removal of this layer. As the subjacent substrate surface must be opened up at any position, the etching depth must be chosen according to the maximum residual layer thickness.

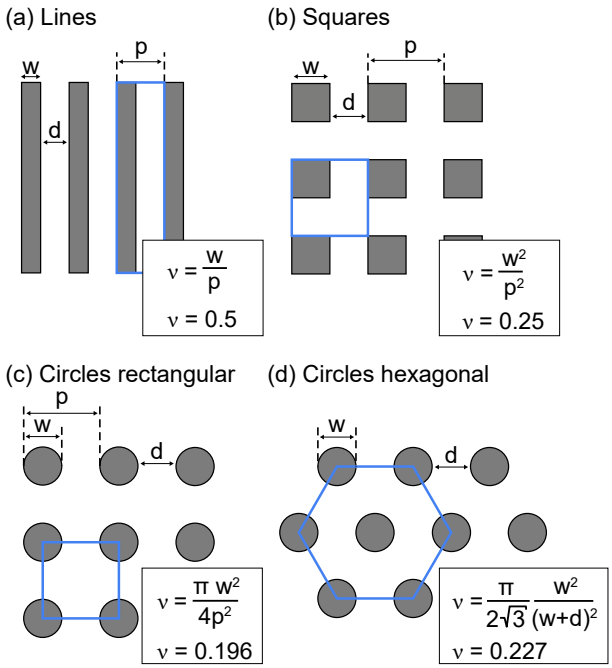

Figure 5.2: Fill factors calculated for different stamp layouts used in this thesis. The formula for the fill factor ν used in the Stefan equation is given in the corresponding boxes, as well as the values for the fill factor for the case where the width w is equal to the inter distance d. Here, the pitch p is defined as p=w+d. The unit cell of each layout is outlined with blue lines.

The fill factor is essential for defining the needed initial imprint resist thickness, and as a consequence also the final residual layer thickness and calculating its value is the starting point of every NIL experiment. The precise control of the residual layer as a critical parameter was one of the challenges in order to achieve high-resolution structures. This comes along with a precise method to apply homogenous layers of resist with nanometer thickness resolution. The formula to calculate the fill factor for the most commonly used stamp layouts can be found in figure 5.2. Here, the fill factor ν is calculated depending on the width of the structure and their pitch (which is defined as the sum of the structure width and their inter distance).

5.2.1 Squeezed flow of imprint polymer during molding

A convenient way for modeling the squeezed polymer flow underneath the stamp protrusions is by solving the Navier-Stokes equation with nonslip boundaries and treating the polymer as an incompressible liquid of constant viscosity. For a line-shaped stamp, this results in the following expression, which is known as the Stefan equation[36] (Equation 5.3).

$$\frac{1}{h^2(t)} = \frac{1}{h_0^2} + \frac{2F}{\eta_0 l w^3} t \tag{5.2}$$

With a constant imprint force F, line-width w, length l, and polymer viscosity η_0.

Inserting the final thickness (residual layer) $h_r = h(t_f)$ and assuming a constant pressure $p = F/(wl)$ under each stamp protrusion (this is unequal to the applied imprint pressure, but scales up with a lower fill-factor) will result in the total embossing time for a complete filling of the stamp cavities (of a line-shaped stamp).

$$t_f = \frac{\eta_0 w^2}{2p} \left(\frac{1}{h_r^2} - \frac{1}{h_0^2} \right) \tag{5.3}$$

And additionally for a stamp with cylindrical protrusion with radius R

$$t_f = \frac{3\eta_0 R^2}{4p} \left(\frac{1}{h_r^2} - \frac{1}{h_0^2} \right) \tag{5.4}$$

Analyzing this equation leads to some interesting conclusions. First, the imprint duration will decrease for smaller (more narrow) stamp structures. Therefore, smaller features (smaller values of w) are easier to be imprinted than larger

macroscopic ones, as long as limitations of the polymer material itself do not affect the embossing. Figure 5.3 shows the imprint duration for a line stamp with 50% filling factor (pitch = 2 times the line width) and 100 nm structure height. An initial imprint resist height of 70 nm was assumed, resulting in a residual layer thickness of 20 nm. These are typical values used during the thesis. Standard imprint conditions are chosen: An imprint pressure of 30 bar (converts to 60 bar below the protrusions of the stamp) and 165°C temperature. The needed imprint times for a complete filling of all cavities of the stamp range from less than a second (for line width below 60 nm) up to 285 s for 1μm wide lines and beyond. When imprinting contact pads of several hundred micrometers, this resist flow limitation can be an issue.

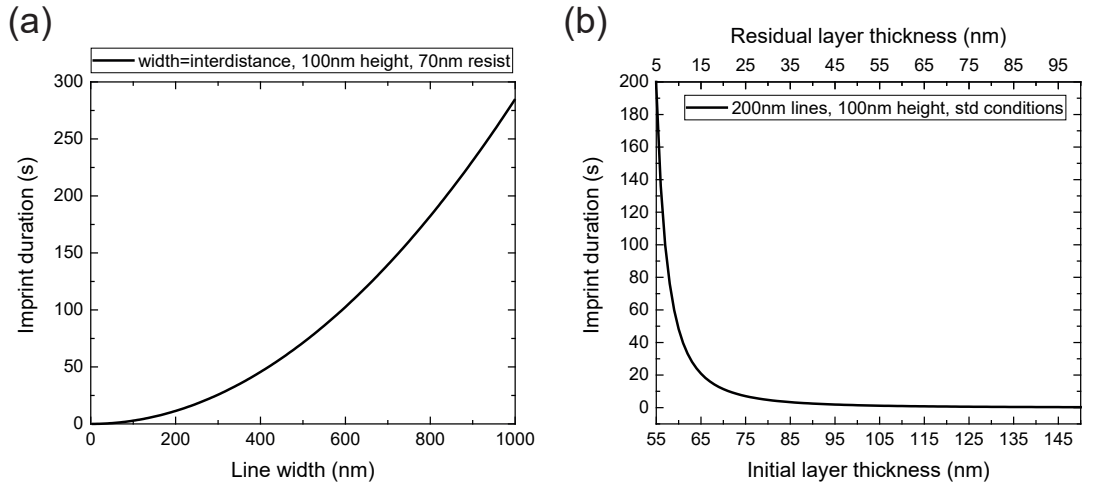

Figure 5.3: Calculated imprint durations for varying parameters. Standard conditions (30 bar imprint pressure, 165°C process temperature) are used with a line-structured stamp where the line width is identical to the cavity width (line inter distance) with a fixed protrusion height of 100 nm. (a) imprint duration for increasing line dimensions for an initial imprint layer thickness of 70 nm (resulting in a residual layer thickness of 20 nm). (b) imprint duration exemplarily shown for 200 nm lines with respect to the initial imprint resist thickness. A layer thickness of 50 nm corresponds to a non-existing residual layer. Values for the residual layer starting from 5 nm are shown.

Table 5.1: Calculated imprint durations for a complete filling of line stamp cavities with different feature dimensions. 50% fill factor, 100 nm structure height, 70 nm resist thickness and standard imprint conditions.

Line width	Imprint duration
50 nm	0.71 s
200 nm	11.4 s
500 nm	71.2 s
1 mm	79154h = 9 years

A direct consequence can be derived from this finding for the case of a complete filling of the stamp cavities (full contact over the total stamp area). For a further vertical displacement of the stamp, the polymer then has to flow from the center to the very borders of the stamp. In this case, w becomes extremely large (the dimensions of the total stamp), and the flow practically stops (Table 5.1). However, there is a limited polymer flow close to the borders of the stamp accompanied by a deformation of the stamp and a slightly thicker resist layer close to the edge of the structured area, as depicted in figure 5.4.

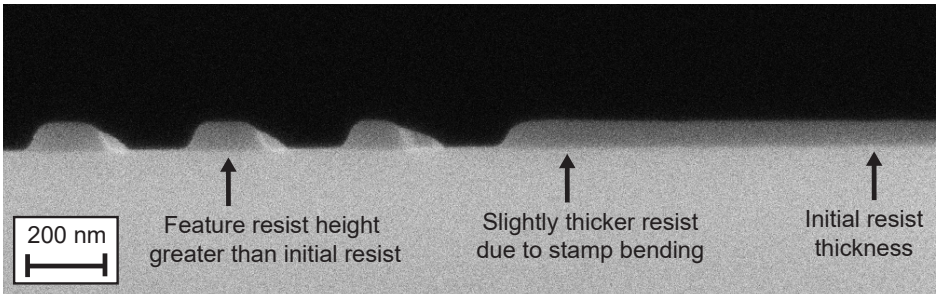

Figure 5.4: SEM image of an imprinted and RI-etched resist at the boundary of the structured area. The height of the polymer structures is greater than the initial imprint resist layer, as part of the cavity height is added to it due to polymer reflow. The same can be observed right at the edge of the structured area. After some hundred nanometers distance, the layer thickness changes back to the original value due to a slight stamp bending.

As a result, the imprint process is hardly affected by a too long printing duration. Even if the theoretical imprint duration is only some seconds, extending the process to several minutes will not change the outcome. In this work, the printing duration of 4 min was usually not changed as it is orders of magnitude longer than needed.
A second result of the Stefan equation is the only weak influence of the embossing pressure on the processing time. If an imprint is not successful, increasing the pressure most likely will not improve the result. As an upside, an expensive nano-imprint machine due to high-pressure components is in principle not needed.

A simple way to drastically reduce process times to mold polymer layers can be achieved by increasing the polymer thickness. For thicker films, the squeezed polymer flow is more unaffected by the friction at the boundaries (substrate and stamp surface). However, this will directly increase the residual layer thickness, and minimizing this residual layer is one of the key concepts when optimizing all process parameters while keeping the imprinting duration reasonably short. To fill all cavities of the stamp, according to equation 5.1, an initial layer thickness of $(1-\nu)\cdot h_p$ is needed. When further increasing the height of this layer, the residual

layer height increases exactly the same amount. To benefit from reduced process times, this thickness can easily reach the dimensions of the pattern (structure height or width) of the NIL stamps. This would result in severe problems when using etching methods to open up the substrate surface. Even with dry-etching methods (section 3.4) a perfect anisotropic etching profile cannot be achieved, thus deep polymer etching also leads to lateral shrinking of the structures. Consequently, a very thick residual layer will result in a shape change (or complete removal) of the imprinted structures during the etching step. In this work, the aim was to obtain a residual layer's thickness of less than 20 nm.
The viscosity of the resist has the most significant effect on the printing time. Although the viscosity is only a linear parameter in the Stefan equation 5.3, the material parameter itself can vary by orders of magnitude (figure 5.5). First of all, when choosing a polymer as an imprint resist, the zero shear viscosity does generally increase with increasing molecular weight of the molecule. It is expected that smaller chains, which are typically present as coils, can move more easily in small cavities of the imprint molds. In addition, the viscosity of every imprint resist can be reduced by increasing the process temperature.
As mentioned in section 3.1.2, the used polymers have a glass-liquid transition or glass-transition temperature. Theoretically, all materials have a glass transition temperature[37]. It is the gradual and reversible transition from a hard ("glassy" state) into a viscous or rubbery state as the temperature is increased. The glass-transition temperature is always lower than the melting temperature (if one exists). It is not considered as a phase transition, and it is not sharp, but it is rather a phenomenon that by convention occurs at a certain viscosity threshold[38]. Even beyond this threshold, the viscosity can be lowered with increasing temperature (figure 5.5). This is a result of the increasing ability of the chains to move freely, while entanglements and van-der-Waals interactions of the chains are reduced.

The used imprint polymer mr-I 8000R and mr-I 8000E (Micro resist technology, Berlin) in this thesis are thermoplastic resists and have a glass-transition temperature at $T_g = 105°C$ (The designation 8020 (which is also used in this chapter) only indicates a pre-dilution of the polymer 8000, where standard spin-coating conditions result in a film thickness of 200 nm). Above this temperature, their viscosity can be reduced by order of magnitude just by increasing the temperature by roughly 10 K. Figure 5.5 shows the decreasing behavior of the viscosity with increasing the temperature. Here, the data points are extracted from the manufacturer's datasheet. It is then fitted using the Williams-Landel-Ferry equation,

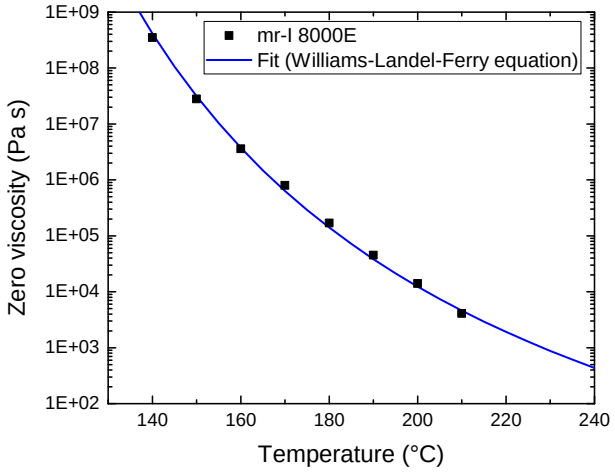

Figure 5.5: Zero viscosity of the imprint polymer mr-I 8000E. The data points are extracted from the manufacture's datasheet. The fit is based on the Williams-Landel-Ferry equation. Reprinted with permission from "micro resist technology GmbH".

which is an empirical equation usually used for polymer melts or other fluids that have a glass-transition temperature (equation 5.5). The parameters C_1, C_2 [K], T_r [K], and η_M [Pa s] are empirical parameters obtained via regression. Typically, T_r is set to be the glass-transition temperature of the polymer, in this case, $T_r = T_g = 105°C$. The parameters C_1 and C_2 then become very similar for a wide class of polymers. The fitted values here are $C_1 = 18.5$, $C_2 = 58\,\mathrm{K}$ and $\eta_M = 3.8 \cdot 10^{15} Pas$.

$$\eta\left(T\right) = \eta_M \exp\left(\frac{-C_1\left(T - T_r\right)}{C_2 + T - T_r}\right) \tag{5.5}$$

From this fit, a reduction of the polymer viscosity by nine orders of magnitude between the glass-transition temperature ($T_g = 105°C$) and the process temperature of $T_p = 165°C$ can be derived. Thus, temperature as a process parameter plays the dominant role in the Stefan equation 5.3 and the NIL process by changing the viscosity $\eta_0\left(T\right)$.

5.3 Lift-off nanoimprint lithography

Nanoimprinting lithography is an elegant way to pattern resist layers with sub-50 nm structures. For etching purposes, this film acts then as a mask to transfer its pattern into the substrate. In the field of energy conversion applications, typically metallic nanostructures are needed. Here, the minimal lateral dimensions of the structures (and as a result the thin layer thickness of the imprint polymer) are a problem.

Performing physical vapor deposition (PVD) directly on the target substrate under high vacuum conditions leads to well-defined metal/substrate interfaces and smooth metal surfaces, which is very important for electrocatalytic applications where these properties are crucial. The most commonly used method in microtechnology to fabricate metal structures is the lift-off technique. Here, the substrate material is coated with a sacrificial material (e.g., photoresist) and patterned to open up the surface of the substrate at predefined spots. Then, a defined thin film of metal is deposited over the whole area of the substrate, only having direct contact with its surface inside the openings. When the sacrificial layer is washed away with a solvent, it will also remove unwanted metal on top of it, leaving only the patterned metal structures on the substrate behind.

Usually, also the sidewalls of the sacrificial layer get covered during the deposition step, which will prevent the solvent from dissolving the resist when a closed film has been formed. To avoid this problem, rather thick resist films or the formation of a sidewall undercut are necessary to separate the metal film on top of the resist from the parts on the substrate. Using optical lithography, this is achieved with an image reversal photoresist in a negative process (section 3.1.1). An example of such shaped AZ5214E resist (Microchemicals, Germany) can be found in Figure 5.20(a).

With nanoimprint technology, this is by default not possible. A patterned stamp with such a shaped sidewall would be inevitably impossible to demold from the imprint resist as the resist will fill up these undercut areas during the imprint process and, as a result, will be fixed to the stamp after the hardening step. This is why, in this sense, perfectly vertical sidewalls are the most optimized ones that can be achieved. In reality, there is always a slight slope formed during the etching step of the master mold fabrication. Hence, a direct lift-off process with standard NIL is only possible for very thin metal layers, and it is highly likely that one has to deal with common defects like unwanted metal retention between the patterned structures and ear defects on their metal surface.

To overcome these limitations, a method was developed to generate an artificial

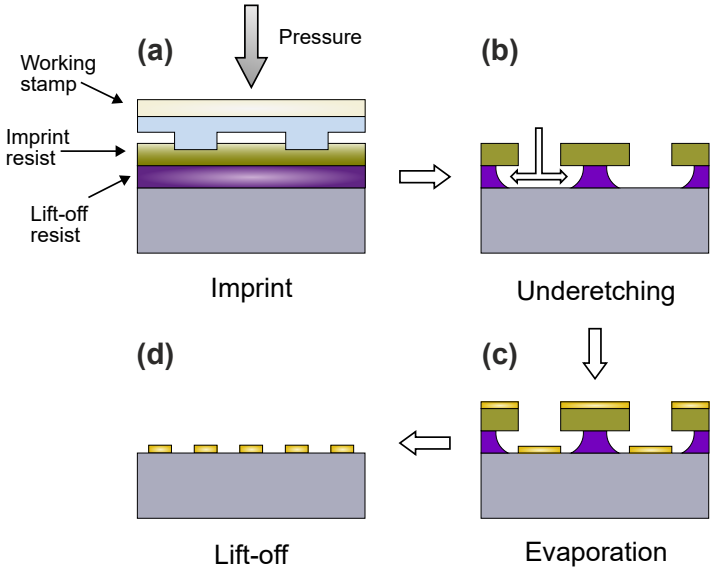

Figure 5.6: Sketch of a bi-layer lift-off nanoimprint process. (a) An additional layer of resist is introduced as a lift-off resist, and the imprint polymer is patterned with NIL (b) After removing the residual layer of the imprint using RIE, the LOR is partially developed leading to an underetching of the imprint resist. (c) A metal layer is evaporated. The undercut results in a separation of the metal film on the substrate to that on the resist. (d) All of the resists are removed with a solvent, only leaving the metal pattern on the substrate behind. Reprinted from [13] with the permission of AIP Publishing.

undercut by establishing a bi-layer lift-off imprint process (LO-NIL). A second layer of resist is introduced between the substrate and the imprint polymer acting as a lift-off resist (LOR). A sketch of the polymer layer stack and the process can be found in figure 5.6. First, after cleaning the substrate, the LOR is spin-coated on the substrate. After a soft-bake step to remove all solvent and to harden this film, the imprint resist layer is applied using common spin-coating procedures and parameters followed by a soft-bake. The imprint stamp is placed on the substrate and an imprint process is performed. As the protrusions of the stamp do not penetrate the LOR, it therefore remains unaffected by this step (figure 5.6 (b)). Reactive ion etching is then used to remove the resulting residual layer of the imprint resist and will also partially etch into the LOR layer. The more the LOR is thinned in this step, the shorter is the needed etching time later on, to form the undercut. However, long (not perfectly anisotropic) RI-etching may result in a widening of the nanostructures, which must be avoided.

The partial lateral removal of the LOR can be achieved with either a dry-etching or a wet-chemical method. This will lead to an undercut of the imprint resist, and thus to an artificial negative slope of the sidewalls. This etching step has to be highly selective to only remove the LOR, leaving the imprint resist unaffected.

Now, the sample is ready to be coated with a thin metal film. The metal film on the substrate will be separated from the layer on top of the resist even if the sidewalls of the pattern are partially coated as well (figure 5.6 (c)). As a final step, the sample is immersed in a suitable solvent to remove both resist layers, and by that, also the unwanted metal film (figure 5.6 (d)). This step can be carried out in an ultrasonic bath at higher temperatures if needed. After cleaning the surface with isopropanol or DI-water, the process is completed and the sample is ready for further processing steps or measurements.

5.3.1 Material requirements for a bi-layer resist approach

Finding the best resist combination for this type of process is quite a challenge. Many requirements must be met and are listed in the following. Some of which must be fulfilled and some are just a nice-to-have.

1. It must be possible to spin-coat both layers on top of each other without intermixing. This does require the LOR to be resistant to the thinner of the imprint polymer.

2. The resulting minimal film thickness of the LOR should be below 20 nm without de-wetting from the substrate.

3. The soft-bake of the imprint resist should not alter the LOR properties (temperature stability).

4. The imprint process should leave the LOR unaffected, especially concerning temperature and pressure.

5. Additionally, the LOR must be stable during the imprint process, such as no flow towards the stamp cavities occurs. This implies that the glass-transition temperature of the LOR is much higher than the one of the imprint polymer.

6. The LOR can be selectively wet or dry-etched over the substrate.

7. In the best case, the LOR can be selectively dry-etched over the imprint resist. This way, a complete removal of it is possible while shape retention of the pattern is given. Also, this would enable an all-dry-etch process, which should be very stable.

8. Development (underetching) of the LOR must be selective over the imprint polymer.

9. The developing rate must be reasonably stable, and the time-scale for this process must be practicable (the used dilution of the developer can easily adjust this)

10. A solvent must be found to completely remove the polymer layer from the substrate surface during the lift-off process. In the best case, it also removes the imprint polymer.

The following combination of resists is found to meet most of the requirements: PMGI SF6 from Michrochem, USA is used as a lift-off resist, which is diluted with G-thinner from the same company. mr-I 8020R from Microresist, Germany, is used as the thermal imprint polymer and ma-T1050 as its thinner. In the following sections, characterization of the resists and processes are performed and proves the resist types to be well chosen.

5.4 Fabrication and Characterization

5.4.1 Thin film layer thickness characterization

The polymer materials used as resists in this work have an excellent resistance to developers and wet and dry etching processes. However, they are sensitive to mechanical influences (e.g., scratching). This makes it difficult for thickness measurement methods where a stylus/tip is used in contact mode like in surface profilometers. There, typically the surface is getting scratched, and the resulting measured thickness is then lower than expected. With AFM, it is possible to measure in tapping mode and with reasonably low forces where the characterization of polymer layers is possible. However, this method is time-consuming. A convenient way to determine the layer thickness of thin transparent films is by using ellipsometry. Here, the refractive index $n(\lambda)$ of one or multiple polymer layers, the substrate, and the environment (typically air (n=1)) have to be known, and a rough assumption about their thicknesses must be made. The exact values are then measured using a laser by the change of polarization upon reflection or transmission and by comparing it to a model. This method is especially interesting for thin films, as it is a contact-free characterization method, and the result is intrinsically an average over the laser spot area, making it a very stable technique while multiple measurements on a single spot are not needed. Additionally, the

measurement itself takes just few seconds.
The value of the materials refractive index depends on the used laser wavelength, which has to be used in the model. For most materials, this value can be looked up in literature or online databases. For the imprint polymer mr-I 8000R and PMGI SF6 the values can be calculated by using Cauchy-parameters from the manufacturer datasheet and the following equation 5.6.

$$n(\lambda) = A + \frac{B}{\lambda^2} + \frac{C}{\lambda^4} + ... \tag{5.6}$$

Usually, it is sufficient to use a two-term form of the equation.
For the UV-imprint resist NDK UV-01, those parameters are not given and thus were determined using interferometry during this thesis. Interferometry is an optical, non-invasive characterization method, which can be used when neither the film thickness nor the refractive index value is precisely known. A thin film is spin coated on a substrate with known material properties. Light from a nearly monochromatic source is focused perpendicular on the sample surface, the intensity of the reflected light is then measured for a wide wavelength range. The light reflected by the upper and lower boundaries of the thin film interferes with one another, thus the resulting intensity pattern is determined by the phase difference between these two waves. Waves that are in phase will undergo constructive interference, while waves that are out of phase will undergo destructive interference. By using samples with different film thicknesses, the measured data can be fitted to get both the Cauchy-parameters and the film thickness of the resist layers. Here, a fitting tool developed by Alexander Andrejew (TUM) was used, which is based on Mondry et al.[39]. Three thicknesses (815 nm, 955 nm, and 1356 nm) were measured and fitted simultaneously. A measurement and fit are exemplarily shown in figure 5.7. The fit matches very well the experimental data. At a lower wavelength, light is absorbed by the UV-curable resist. This leads to a deviation in peak height from the fit as it does not include an imaginary part of the refractive index. However, at the point of interest (laser wavelength $\lambda = 632.8nm$), absorption is minimal to none present.

The used refractive index values and Cauchy parameters are listed in table 5.2.

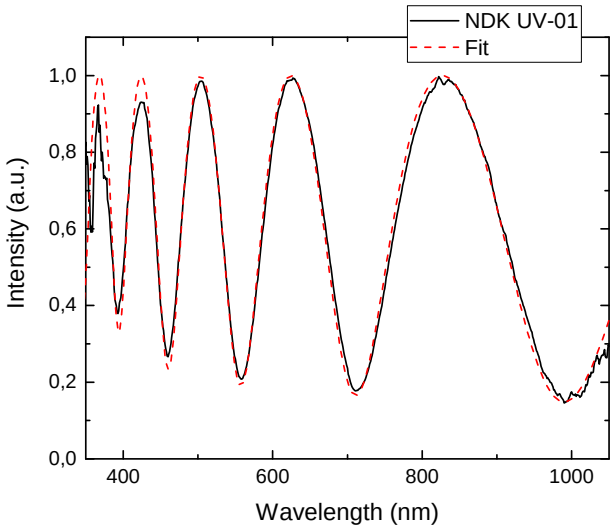

Figure 5.7: Measurement and fit of an 815 nm thick film of UV-curable imprint resist NDK UV-01. The fit is performed by Alexander Andrejew (TUM).

Table 5.2: Refractive index values at 632.8 nm and Cauchy-parameters for used materials and resists. Values for materials marked with an asterisk are taken from the corresponding manufacturer datasheet.

Material	Refractive index n	Cauchy-parameters A	B (nm^2)	C (nm^4)
mr-I 8000R* [40]	1.5667	1.547	7900	0
PMGI SF6* [41]	1.5382	1.524	5176	$2.105 \cdot 10^8$
NDK UV-01 [42]	1.531	1.508	9400	0
mr-UVCur21* [43]	1.48252	1.473	1600	$8.8 \cdot 10^8$
Ormostamp [44]	1.50461	1.491	5600	$2 \cdot 10^7$
Silicon [45]	3.874 (k=-0.016)			
Silicon-oxide [46]	1.465	-		
Gold [47]	0.184 (k=-3.43)			
Aluminum [48]	1.153 (k=-6.69)			

5.4.2 Spin coating

The correct coating procedure is essential for a homogenous and well-defined resist thickness. In principle, a variety of coating methods are possible. Using spray coating, a solvent-rich resist gets atomized into small droplets, and the spray will form a growing resist film on the substrate. This technique can be used with almost any kind of substrate. However, the obtained surface roughness can be comparably high. With dip coating, the substrate is pulled out of a resist-filled basin vertically with a defined speed. It is a non-complex technique, but the thickness of the film may vary over the dimension of the substrate. Roller coating is especially useful with flexible substrates. Here a coated roller transfers resist

to a substrate. The roller is covered with resist just by partially immersing it in a resist-filled basin or by additionally using knife coating, where a blade is used at a defined distance to the roller, leading to a constant and defined thickness of the film. Here, the resist gain is almost 100%, however, it might not be a practical method for small and hard substrates.
The most widespread coating type to get thin-film polymer layers is spin coating and is mainly used in this work. First, the flat substrate has to be thoroughly cleaned to remove any particle as these would result in defects in the final thin film. Cleaning is performed in acetone in an ultrasonic bath for 10 min followed by rinsing with isopropanol. To further remove organic contaminations, the substrates are treated with oxygen plasma in a barrel etcher (200 W, 2 min). Here, it is essential to know the properties of the polymer used for spin coating. If it is a polar molecule, then the generated hydroxyl group on the silicon surface (which are polar itself) favors the sticking of the resist to the substrate. For non-polar resists heating the substrates on a hotplate above 100°C is a more expedient solution to remove adsorbed water molecules.

Then, a small amount of resist polymer is applied at the center of the substrate. This was done using a syringe with a 0.25 micron PTFE filter to remove any particles above this size, avoiding particle defects in the final layer. The substrate is then rotated at high speed in order to spread the coating material by centrifugal force. The viscosity of the resist and the angular speed of spinning determines the final thickness of the layer. This process is very fast (less than a minute) and produces very smooth surfaces. The rotation speed can be easily adjusted, and the viscosity of the resist can be reduced by mixing it with a solvent used as a thinner liquid. While spinning, the excess resist is removed from the substrate. Simultaneously, parts of the thinner evaporates (typically about 90%) leading to a higher viscosity of the resist and a stop of the thickness change. After the spin coating, a soft-bake is performed to remove nearly all of the thinner liquid.

Knowing the exact resist layer height is essential for subsequent etching processes. When working with imprint structures with very small lateral dimensions, a strong overetching can lead to a lateral reduction in size when the etching process is not perfectly anisotropic. The layer thickness after the coating process must therefore not only be well known, but also the variation of this thickness between several samples should be as minimal as possible. Thus, a thorough characterization of this process is fundamental.

Table 5.3: Spin coating layer thickness fit parameters for mrI-8020R.

Dilution	Parameter a	Exponent b
undiluted	11701	0.5
1.0/1.0	4709	0.5
1.0/2.0	3918	0.5
1.0/3.0	3550	0.5
1.0/4.0	2470	0.5

The thickness of the resulting resist layer on the substrate was measured with ellipsometry using a laser ($\lambda = 632.8nm$). The experimental data is shown in figure 5.8 for the used imprint polymer mr-I 8020R and lift-off resist (LOR) PMGI SF6 for angular rotation speeds between 1000 rpm and 6000 rpm. Different dilutions of the initial resist were used using the thinner ma-T 1050 and G-thinner for the resist mr-I 8020R and PMGI SF6, respectively.
Typically, such spin-coating curves can be characterized by the following well known (simplified) law[49–51]:

$$h = a\omega^{-b} \tag{5.7}$$

where ω is the angular rotation speed, and a typical value of the exponent is $b = 0.5$.
This expression is used for fitting the measured data points to theory. The experimental data of the imprint polymer mr-I 8020R nearly perfectly matches the fit (figure 5.8 (a) after softbake (100°C - 1 min)). The values of the exponent b are very close to the expected value of 0.5, so it is reasonable to fix it to this value leaving only one free parameter defining the dilution of the resist. The fitted parameters for each dilution are listed in table 5.3. The layer thickness on silicon substrates was homogenous throughout the whole sample surface (11x11 mm and 20x20 mm), and the edge bead was very small. In comparison, spin coating the LOR showed a slightly more unstable result. First, the homogeneity varied from sample to sample. While the sample center had almost identical thicknesses when using constant spin coating parameters, it changed gradually close to the sample edges (up to 3 mm). Figure 5.8 (b) shows the layer thickness for the lift-off resist after soft bake (255°C - 3 min). Here, the fitted parameters using equation 5.7 are changing for different dilutions. The values are given in table 5.4.

Knowing the exact thickness of the LOR and the imprint polymer is highly important, thus it was measured for each sample individually. A statistical representation of the data is shown in figure 5.9 for one of the standard parameters.

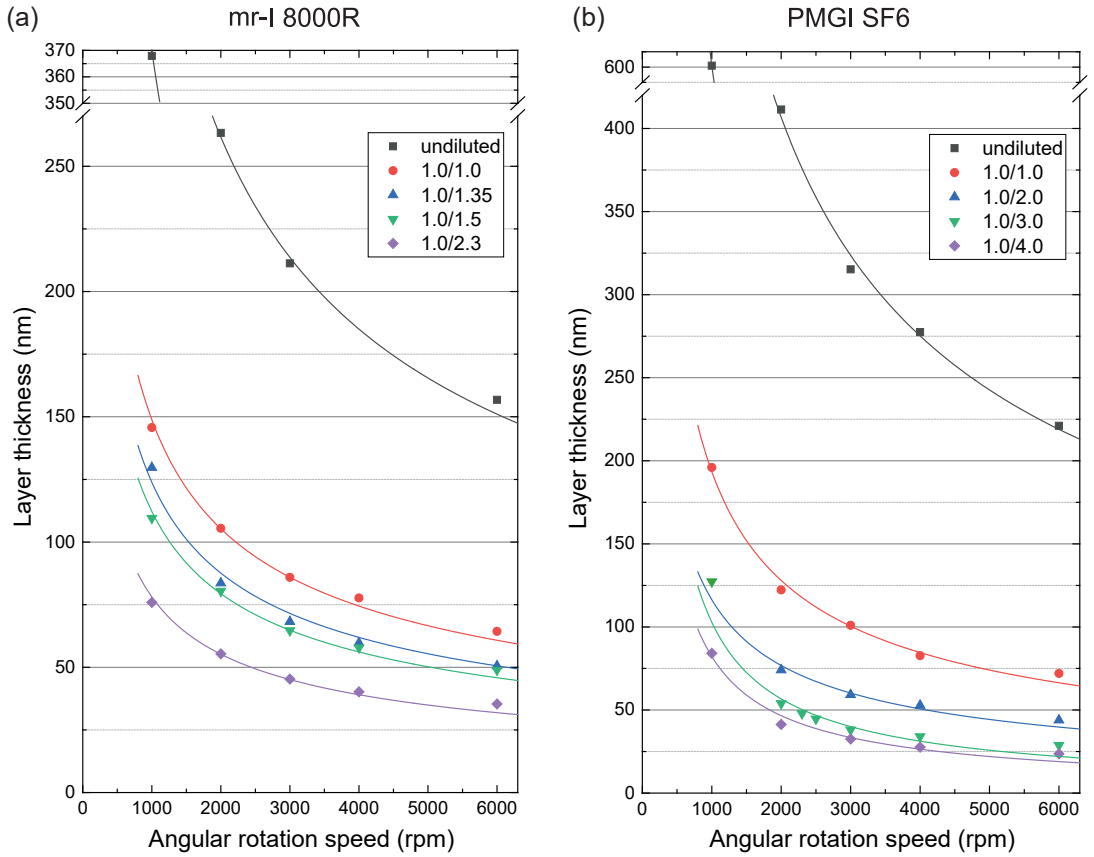

Figure 5.8: Resist layer thickness after spin coating and after soft bake for different rotation speeds. The base polymer is diluted with the corresponding thinner to get various concentrations for (a) imprint polymer: mr-I 8020R (Thinner: ma-T 1050) and (b) Lift-off resist: PMGI SF6 (Thinner: G thinner). Parts of the data points were already published in[52].

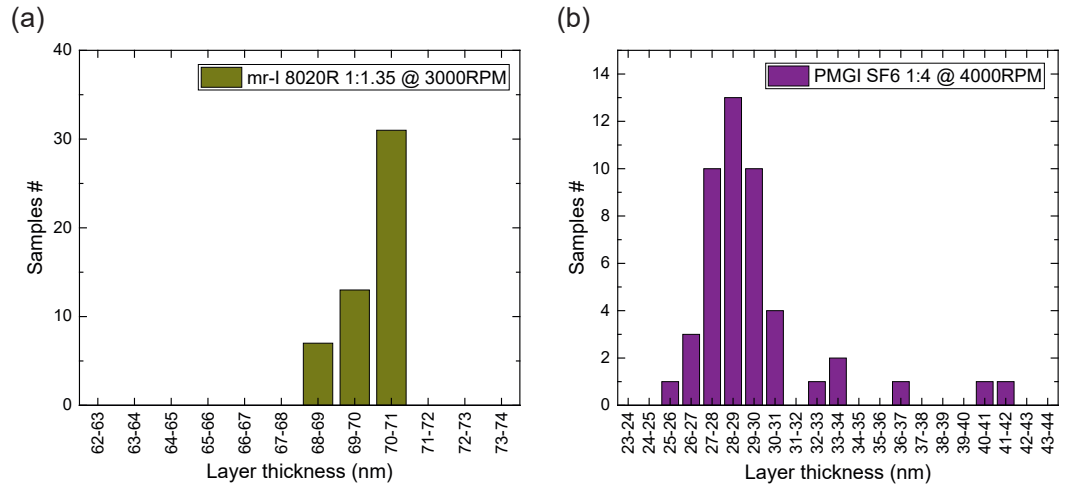

Figure 5.9: Layer thickness statistics for a single constant dilution and rotation speed. (a) imprint polymer: mr-I 8020R (Thinner: ma-T 1050) and (b) Lift-off resist: PMGI SF6 (Thinner: G thinner).

Table 5.4: Spin coating layer thickness fit parameters for PMGI SF6.

Dilution	Parameter a	Exponent b
undiluted	29548	0.56
1.0/1.0	11970	0.60
1.0/2.0	7345	0.60
1.0/3.0	38885	0.86
1.0/4.0	23515	0.82

Spin coating the imprint resist mr-I 8020R shows very stable results, where the variation of the final thickness is typically below 1 nm within one fabricated sample set. More considerable variations were only noticed between different process days. However, it was still minimal (below 3 nm). The LOR is slightly more unstable in this sense, and the thickness variation is larger even for the same sample sets. Furthermore, it is possible to obtain a final thickness far from the expected value, as depicted in figure 5.9 (b), which then can not be used anymore for further processing. Cleaning and pretreatment of the substrate have an important role on the result. In most cases, the thickness variation is still acceptable and can be addressed by measuring the layer thickness for each sample and adjusting the etching or developing time individually.

5.4.3 Residual layer characterization

If no dewetting of the imprint polymer from the substrate surface occurs, there will always be a residual layer left on the substrate below the stamp protrusions. This is caused by the more and more limited ability of the polymer to flow underneath the protrusions towards the stamp cavities when the layer thickness decreases (Cf. equation 5.3). The thickness of this remaining layer determines the parameters for subsequent etching steps for its removal. As unnecessary overetching will also lead to partial lateral etching and a change of the nanostructure shape, characterizing the exact thickness of this layer is a crucial step.

For this purpose, imprinted samples using each master stamp type were fabricated. The residual layer of the imprint polymer after the imprint process was characterized using AFM as follows: First, the structured area of the imprinted polymer is scratched using a scalpel to remove it from the underlying silicon surface. This process does not damage the silicon surface. It is helpful to perform a slight sideways motion during the scratching. With that technique, excess of the polymer mainly accumulates only on one side of the scratch, which is needed to

find a suitable spot for the AFM measurement. Also, performing the scratch parallel to the structure direction (if line-shaped) favors a straightforward evaluation of the layer thickness. Then, an AFM image is taken on the edge of the scratch. Such an AFM measurement can be found in figure 5.10. Here a line stamp with 200 nm lines and 400 nm pitch was used. The scan direction is perpendicular to the lines in tapping mode. From an extracted profile (marked in the image), it is possible to determine the residual layer thickness accurately (here, 19.6±0.5 nm). In addition to the AFM measurements, the substrate is cleaved afterward perpendicular to the structure direction, and side-cut images of the imprint are taken using SEM. However, with SEM, it is hardly possible to determine exact layer thicknesses for non-conductive materials due to a surface charging effect caused by the e-beam itself. Nevertheless, it was used to check the efficacy of the imprint on a larger scale.

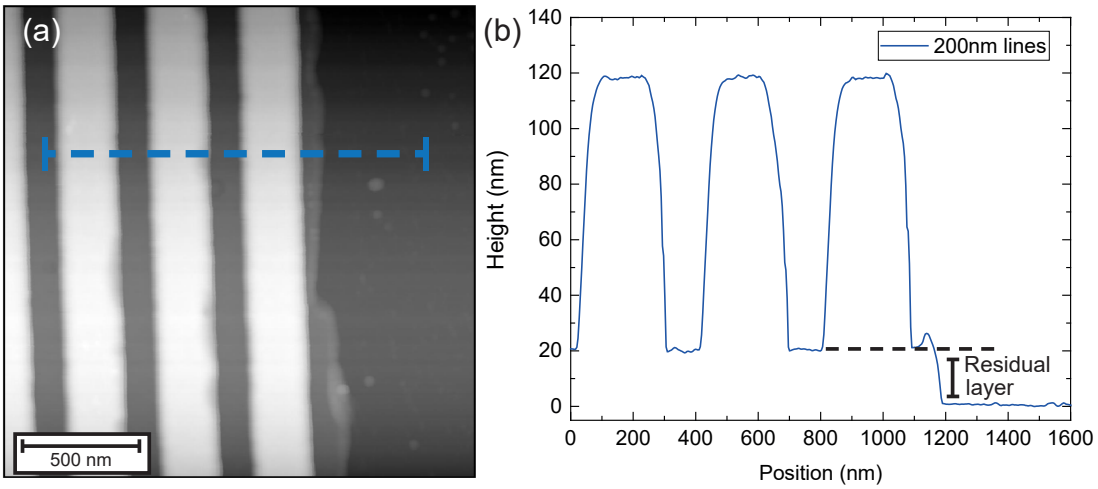

Figure 5.10: Residual layer measurement using atomic force microscopy. A silicon wafer with thermal imprint resist (mr-I 8000R) is structured using a 200 nm line stamps (400 nm pitch). Parts of the resist are scratched with a scalpel. The residual layer thickness is the height between the layer thickness in the line cavities and the substrate.

Table 5.5: Residual layer thicknesses for selected stamp layouts (L=lines, P=pillars).

Stamp structure	Polymer structure height (nm)	Initial layer thickness (nm)	Residual layer thickness (nm)	Calculated value (nm)
L200	92.4	60.2	24.7	16.4
L200	94.5	48.7	3.8	3.9
L200	94.5	60.8	22.8	15.9
P75	87.2	80.5	15.1	10.4
P200	87.5	81.0	17.3	15.4

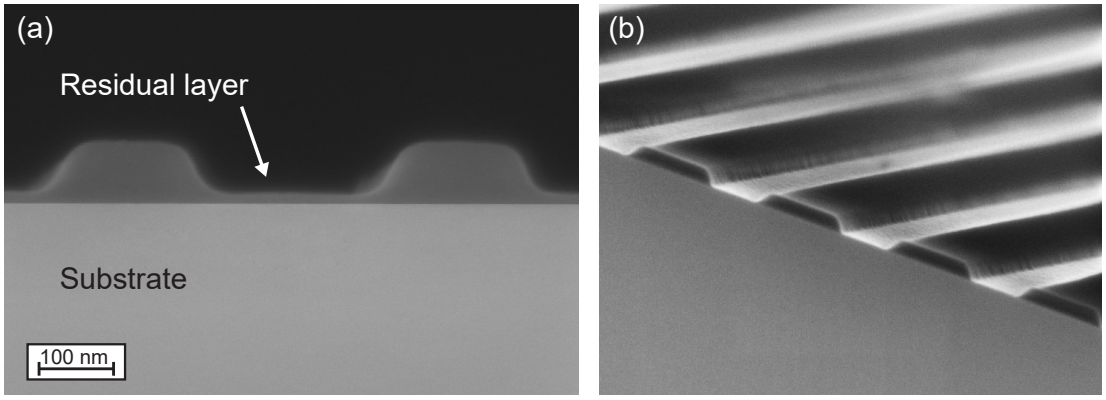

Figure 5.11: Residual layer measurement using scanning electron microscopy. A silicon wafer with thermal imprint resist (mr-I 8000R) is structured using a 200 nm line stamps (400 nm pitch). The substrate is cleaved perpendicular to the line-shaped nanostructures, and a side-view image is taken (a) after the imprint. The residual layer is visible on top of the substrate. (b) after RI-etching. The residual layer is removed and the subjacent substrate surface is opened.

The residual layer thickness measurements showed a slightly larger residual layer as calculated with ideal shape parameters. The stamp layout deviated from the ideal case by terms of edge curvature, which reduces the fill factor (see section 5.2). An additional factor is the not perfectly vertical sidewalls. During etching of the master and the two-fold replication to produce the working stamp even small deviations from the optimal case are decreasing the cavity volume. Both effects are resulting in a thicker residual layer, which has to be taken into account during its removal.

5.4.4 Residual layer removal

The residual layer has to be removed with minimal lateral etching of the nanostructures. For having a highly anisotropic etch characteristic, chemical dry-etching is typically used. In the following different approaches are tested for their applicability of residual layer removal of purely organic polymers.

Oxygen plasma used for thin polymer film etching

Barrel etching A barrel plasma etcher (section 3.3) removes organic polymers when oxygen is used as process gas. The advantage here is a high selectivity against the silicon surface. Also, the ignition of the plasma is very stable, while a relatively slow etching rate offers reasonable control over the etch depth. An etching rate of 7.8 nm/min (0.13 nm/s) was measured for an rf-power of 300 W with a gas flow of 74 sccm. However, a barrel etcher is typically used to remove thin contamination layers only or to activate a substrate surface by the generation

of hydroxyl groups. It was found that the etching rate may change daily, thus a calibration sample is needed before a process run (yet, this was done anyways). Samples are not actively cooled during the etching process, thus they heat up during the process. This can be a problem when the temperature rises above the glass transition temperature of the imprint polymer. The maximum temperature was measured using Testoterm thermometer strips. The maximum temperature was reached after 3-6 min and was determined to be 54±5°C for a power of 200 W. For low rf-powers of 100 W, the temperature is 40±3°C and does rise to values of 60±5°C for 600 W. All these values are far below $T_g = 105°C$ of the used imprint polymer. A major disadvantage of this dry-etching method is the rather low anisotropic etch behavior, thus the imprinted structures are almost equally etched laterally and vertically. As a consequence, a barrel etcher was only used to remove very thin residual layers or when metal substrates are used, which should not be etched with RIE because of contamination issues.

Reactive ion etching The dry etching method RIE is instead used to remove the residual layer of the imprint polymer after the pattering step (see section 3.4) as it favors a more vertical etch profile. A Plasmalab 80 from Oxford was used during this work. However, even with optimized parameters, it is hardly possible to reach perfect anisotropy. This is why the etching rates and characteristics are first analyzed. First, oxygen-only as process gas is used due to the organic-only containing resists. This enables a residual-free removal of the polymer. Also, it is perfectly selective to silicon and silicon oxide. A low forward power of 35 W was used with an oxygen flow rate of 30 sccm at a pressure of 15 mTorr. These parameters resulted in a DC bias of 150 V (leading to a directed vertical acceleration of the oxygen ions towards the substrate). The etch rate of the imprint polymer mr-I 8000R was determined to be 1.15 nm/s. This rate is very stable throughout the process but yet slightly too large. As the forward power is set to a minimal value to reduce the etching rate, the ignition of the plasma gets less stable and takes up to 3 s, while the etch duration of a 15 nm thick residual layer only takes 13 s itself. This results in an unwanted uncertainty of a maximum of 19% (for these values).
Liquid nitrogen can actively cool the substrates, which reduces the chemical etching speed. In Table 5.6, the etch rates are given. When cooling down from room temperature to -27°C, the etch rate is reduced to 0.99 nm/s.

However, the additional cooling step (and heating step afterward) does extend the processing time significantly and does not justify the lower etch rates. Instead,

Table 5.6

Temperature	Etchrate (nm/s)
25°C	1.15
-14°C	1.10
-27°C	0.99

a plasma chamber clean was performed before the first etching step stabilizing the plasma ignition, while also a test sample was etched first to determine the etch rate.

Additionally, the etch rate for the lift-off resist PMGI SF6 is of interest, as discussed at the beginning of this chapter. In the best case, the LOR can be selectively etched both against the imprint polymer and the substrate. If only selective against the substrate, the etching rate of the LOR should be larger than the imprint polymer. This enables a very short wet-chemical development time as the vertical removal of the LOR is then mostly covered during the dry-etching step, thus the LOR development is only needed to create a lateral undercut (figure 5.6 (b)). The etching rate of the LOR is determined to be 1.58 nm/s, when using identical parameters as mentioned above for the imprint resist. This is slightly larger than the etching rate of the imprint polymer (1.1 nm/s), but not significantly. In particular, it is not sufficient to entirely remove the LOR vertically. The LOR must be thicker than the metal height of the final nanostructures (typically 20 nm) in order to guarantee the separation of the metal layer on the substrate to the imprint polymer on top of the LOR. Taking the measured rates as a basis, the imprint polymer would also get etched almost the same amount as the LOR. As a consequence, the dimensions of the structures would change, if not perfectly anisotropic.

Feature dimension tuning

Feature dimensions are predefined (and fixed) by the master mold, which is single time written with e-beam lithography. This is a cost-intensive and time-consuming process, which usually has to be carried out individually for every size variation of a sample layout. Using pure oxygen as a process gas, it is possible to tune the lateral dimensions of the nanostructures during the fabrication process (figure 5.12). Oxygen ions will certainly also etch sidewalls to some extent, thus increasing the diameter/width of the openings over time.
This was tested using a pillar stamp with 75 nm diameter. After imprint, the

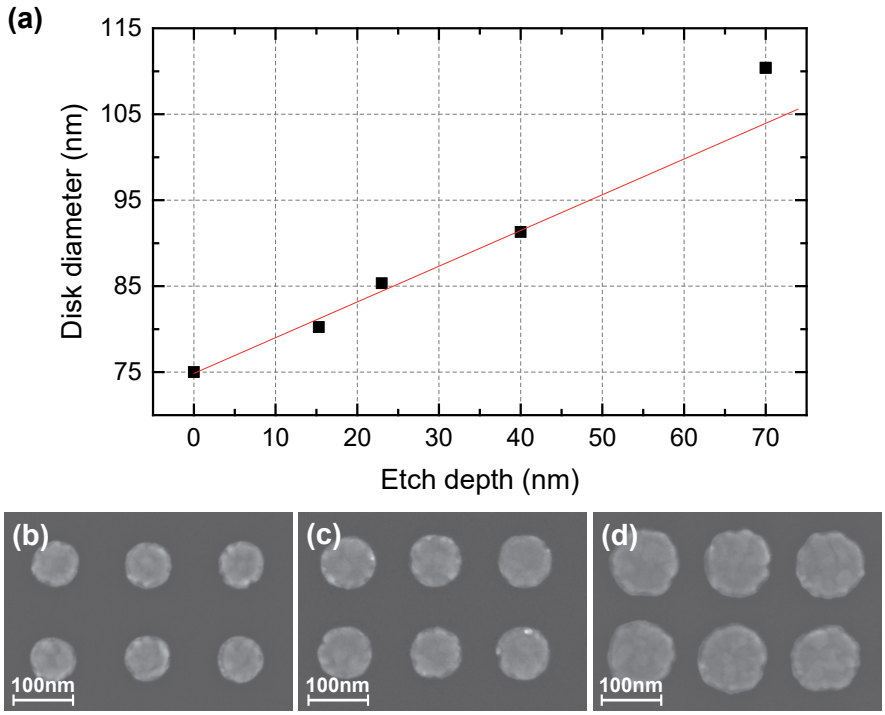

Figure 5.12: (a) Feature size tuning during oxygen reactive ion (RI) etching. The diameter of the Ti/Au disks was tuned during RI etching to (b) 75 nm, (c) 90 nm, (d) 110 nm as shown in SEM images of lift-off samples fabricated with a 75 nm pillar stamp. Adapted and reprinted from Nagel et al.[13] with the permission of AIP Publishing.

residual layer was etched with pure oxygen gas in a RIE process (35 W forward power, 150 V DC-bias, 30sccm, 15 mTorr). The etch duration was varied to cover different etch depths. A thin metal layer was then evaporated on top of the sample, and nanodisks were fabricated by a lift-off method. The diameter of the final Ti/Au nanodisks was measured using SEM.

With this tuning, it is possible to increase the feature diameter of initially 75 nm up to a value of 120 nm (figure 5.12 (a)), which is an increase of 45 nm (+60%). SEM images of an exemplary diameter tuning from 75 nm to a value of 90 nm and 110 nm can be found in (figures 5.12 (b)-(d)). With an etch depth of 25 nm, the diameter is widened by 10 nm (thus, the structures are laterally etched 5 nm on both sides). The anisotropy of pure oxygen RI-etching is therefore 5:1.

This method is extremely beneficial, e.g., for plasmonic applications where fine-tuning of the dimensions of metal nanodisks enables precise resonance frequencies control.

Anisotropic RIE optimization

The removal of a residual layer in the thickness range of 15 nm, would lead to a widening of the structures by 8% (or 6 nm) for 75 nm disks when using pure

oxygen plasma. Reducing the residual layer will directly lead to optimized shape retention, however a fixed over-etching time has to be included in the calculated duration to cover for residual layer thickness variations over the sample and also uncertainties in plasma ignition and etching rates of the RIE process. To get nanometer precision, an optimized anisotropic etching is required.
RI-etching typically consists of a physical and chemical part. The physical part is based on bombardment of the surface with the accelerated ions generated in the plasma. The kinetic energy of the ions will result in an ion sputtering and removal of the surface atoms. By choosing the right process gas, the formed ions in the plasma can chemically etch the sample surface. As it is not an instantaneous process like physical etching, the ions can move after hitting the surface before they undergo a reaction, thus also removing material from vertical sidewalls. Typically, physical etching is more directed and thus more anisotropic. A convenient way to improve anisotropy is to use a chemically inert gas like argon that only has a physical etching component. Also, increasing the acceleration voltage (DC self-bias voltage) results in a more directed etch profile. The DC voltage can be increased by lowering the chamber pressure or by increasing the rf forward power. A different approach to increase the etch anisotropy can be achieved by cooling the sample (cryogenic RIE) in order to limit chemical reactions and ion movement after touching the cooled surface, which produces isotropic etching.
These methods have been tested and showed an improvement in anisotropy compared to the standard oxygen RIE process. Increasing the rf forward power from 35 W to 200 W leads to a DC bias increase from 150 V to 540 V and, as a result, increasing the anisotropy from around 5:1 to 6.9±1.8:1. However, the high rf-power has the disadvantage of a very high imprint resist etching rate, which makes it hard to control. Using liquid nitrogen for cooling while keeping the rf-power at 35 W had an even better effect on the anisotropy, reaching a value of 9.3±3.3:1. Cryogenic RIE is therefore a better solution, with the disadvantage of a longer process, while the value for anisotropy is still not sufficiently high.

As a solution to this problem, a two-gas RIE process for organic materials was developed, inspired by deep reactive ion etching (DRIE) of silicon using a Bosch-process[53], where a short etching step is followed by the deposition of a passivation layer, which protects all open surfaces from further etching (figure 5.13). During the following etching phase, the directional ions that bombard the substrate vertically are attacking the passivation layer at the bottom of the trenches (but not along the sides).

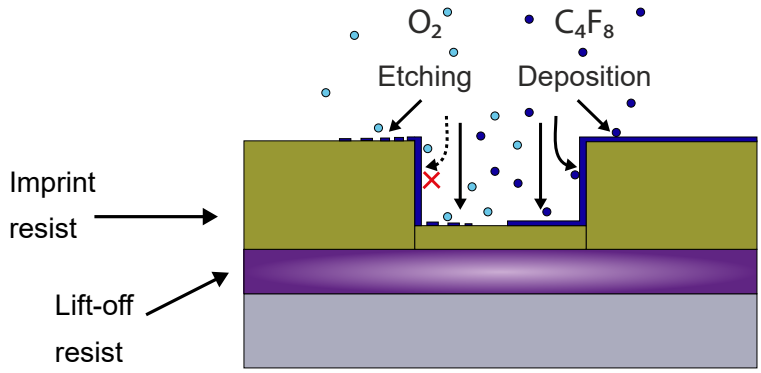

Figure 5.13: Sketch of a two-gas passivation and etching RIE process. C_4F_8 forms a passivation layer on all open surfaces. Accelerated O_2 ions will remove this protection layer only on horizontal surfaces, thus enabling further etching at the bottom of the patterned trenches.

For organic resists etching, a mixture of oxygen (O_2) and Octafluorocyclobutane (C_4F_8) is used. The oxygen will chemically etch the organic content, while the C_4F_8 source gas is supposed to yields a substance similar to Teflon protecting sidewalls of the nanostructures (figure 5.13). In contrast to the Bosch-process, the etching and deposition step is carried out simultaneously.

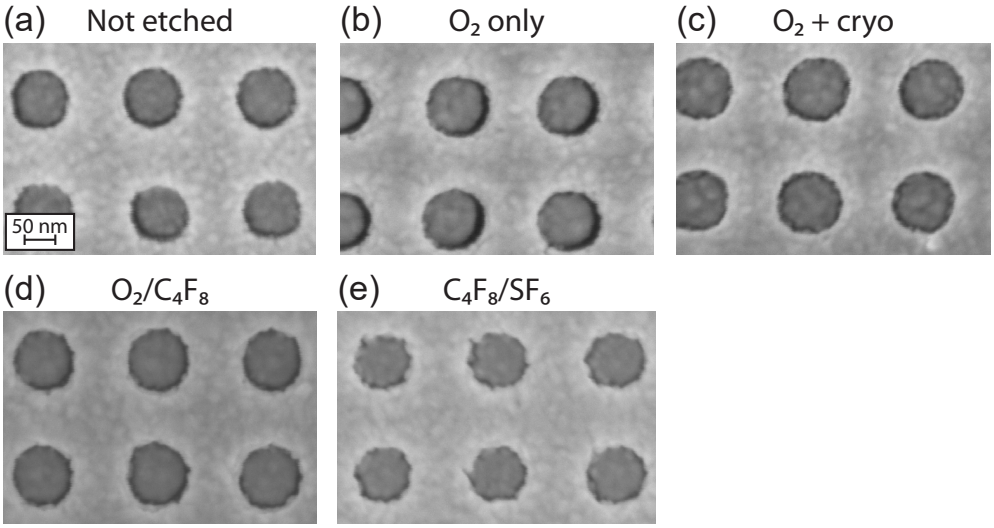

Figure 5.14: SEM images of nanoimprints using a 75 nm pillar stamp in mr-I 8020R polymer and etched with different RIE settings: (a) Unetched (b) O_2-only (200 W, 30 sccm, 540 V DC-Bias); dH=29 nm; anisotropy 6.9:1 (c) O_2-only + cryogenics (35 W, 30 sccm); dH=31 nm; anisotropy 9.3:1 (d) O_2/C_4F_8 (200 W, C_4F_8: 27 sccm - O_2: 25 sccm, 468 V DC-Bias); dH=25.6 nm; anisotropy 15.2:1 (e) C_4F_8/SF_6 (15 W, C_4F_8: 30 sccm - SF_6: 20 sccm, 109 V DC-Bias); dH=24.5 nm; anisotropy 31.7:1.

Different gas flow rates and rf-powers were tested and the result was characterized using SEM, AFM, and Ellipsometry with a special interest in the shape

change caused by the etching. Figure 5.14 shows SEM images of different etch treatments applied to samples imprinted with a 75 nm pillar stamp into mr-I 8000R. All samples were coated with a thin gold layer in order to get a stable SEM image. In figure 5.14 (a) the imprint just after imprinted is shown. Pure oxygen-only processes can be found in (b) and (c), while in the latter cryogenic cooling is applied. Figure 5.14 (d)+(e) shows procedures, where passivation gas is additionally used. The respective process parameters are given in the caption of the figure. It is apparent that the structure edges are very smooth using oxygen only as a process gas. The edge roughness does increase when growing a passivation layer and also for intense etching steps. This is why the C_4F_8/SF_6 combination was not used for device fabrication.

Excellent results are achieved with an O_2 flow rate of 25 sccm, a C_4F_8 flow rate of 27 sccm and a rf forward power of 200 W. This results in a stable plasma ignition while maintaining a reasonably low imprint polymer etch rate. The edge roughness is a little bit larger than using pure oxygen, but still on a high-quality level.

For a 25 nm deep etching using this process, the anisotropy is measured to be above 15:1. However, these values have substantial error bars typically around ± 7. For some etch tests the anisotropy is even above 30:1, yet with error bars larger than the anisotropy value itself. This has two reasons: First, there is an almost non-existing diameter increase during the RI-etching using the passivation layer approach. In most cases, the diameter only increases from 74 ± 1.8 nm to 75 ± 1.8 nm to be 1 ± 2.6, thus the increase is within the error bar of the measurement and may be larger or even negative. Also, the calculated uncertainty is larger than the diameter increase itself, which has an even more significant influence on the calculated anisotropy when approaching values for the diameter increase close to zero, as it is calculated as the half diameter increase divided by the etch depth. Secondly, the anisotropy also depends on the etch depth. While the passivation layer is both grown and etched during the process, only C_4F_8 deposition takes place after the end of the process. This leads to a dominant growth of the protective layer. As a result, for very small etch depths, the diameter change is minimal or can even be negative, as the growth of the layer decreases the diameter of the nanostructures. For longer etch durations, lateral etching is getting more and more dominant.

As a consequence, anisotropy should only be compared when having similar etch depths, and the calculated values are more reasonable for extensive etch depths. Also, there is an optimum etch depth range for perfect diameter retention, which

is between 10-25 nm. For deep trench etching, a step-wise process with separated deposition and etching steps might be advantageous. Then, during the deposition step, oxygen should be replaced with a different and inert carrier gas like argon.

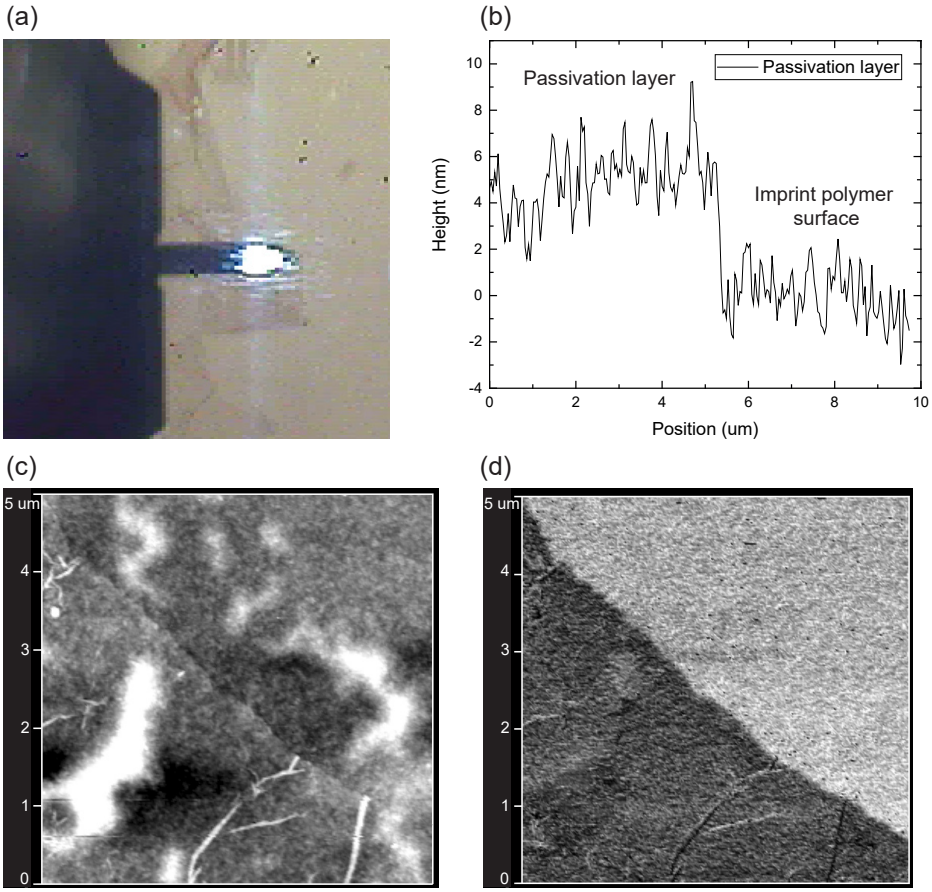

Figure 5.15: Characterization of the RIE grown passivation layer using C_4F_8. The passivation layer was partially removed using wet chemical etching. (a) Camera picture during AFM measurement. The passivation layer is visible next to the AFM cantilever. (b) Extracted height profile. The layer thickness is about 4-5 nm. (c) AFM image of the height measurement. (d) PhaseTrace image of the measurement shown in (c). The change in surface composition is clearly visible as the phase changes during the measurement in tapping mode.

Passivation layer characterization The formed passivation layer that remains on the polymer surface is characterized using AFM. As it also acts as an inhibition layer for further wet chemical etching or developing steps, it must be removed from the LOR. For characterization, a sample with a PMGI SF6 layer is etched with the two-gas RIE procedure and the resulting passivation layer is cracked and ripped apart using a diluted developer (AZ 400K). A picture of the sample surface is shown in figure 5.15 (a) during the AFM measurement. The passivation layer is visible as a slightly darker part of the surface next to the can-

tilever of the AFM. Figure 5.15 (c) gives the image of the height measurement. Here, the change between the passivation layer and the opened LOR surface is hardly noticeable, because the thickness of the passivation layer is small. Phase imaging, a special AFM analysis technique can be used to make this change more visible.

Phase Imaging refers to the monitoring of the phase lag between the signal that drives the cantilever oscillation and its output signal. It is the oscillation "delay" of the cantilever compared to the driving signal while moving up and down (in and out of contact with the sample). Phase Imaging provides complementary information to the topography image, revealing the variations in the surface properties of the sample. It is sensitive to variations in composition, adhesion, friction, visco-elasticity as well as other factors. It is therefore especially useful for this application as the fluorine-containing passivation layer has a different adhesion property compared to the LOR polymer. Figure 5.15 (d) shows the phase image of the same measurement. The different material compositions are now clearly visible. The height profile was extracted at this boundary (figure 5.15 (b)), and the thickness of the passivation layer was determined to be around 4-5 nm.

Reactive ion etching homogeneity

The etching depth must not only be very precise in etching rate, but also in homogeneity across the wafer. The substrates fabricated for electrochemical applications typically had a size of 11x11 mm^2. However, up to nine samples were etched simultaneously in a single RIE process. Thus, the etch depth was characterized on a full 2-inch silicon wafer. First, a thin layer of imprint polymer mr-I 8020R is spin-coated on the wafer and soft-baked with standard parameters, and the resulting layer thickness is measured using ellipsometry (figure 5.16(a)) at 25 individual points depicted in the figure as black dots.

Figure 5.16(b) shows the measured etch depth after RIE. A highly homogeneous etch characteristic is given. For a 42 nm deep etching, the standard deviation over the entire wafer is only 0.38 nm or 0.9%. Even the minimum to maximum difference is only 1.4 nm (3.3%) and is most likely caused by a shifted measurement point between the initial layer and the etched wafer rather than a variation in RI-etching rate. As a consequence, several samples can be etched simultaneously in a single dry-etching run.

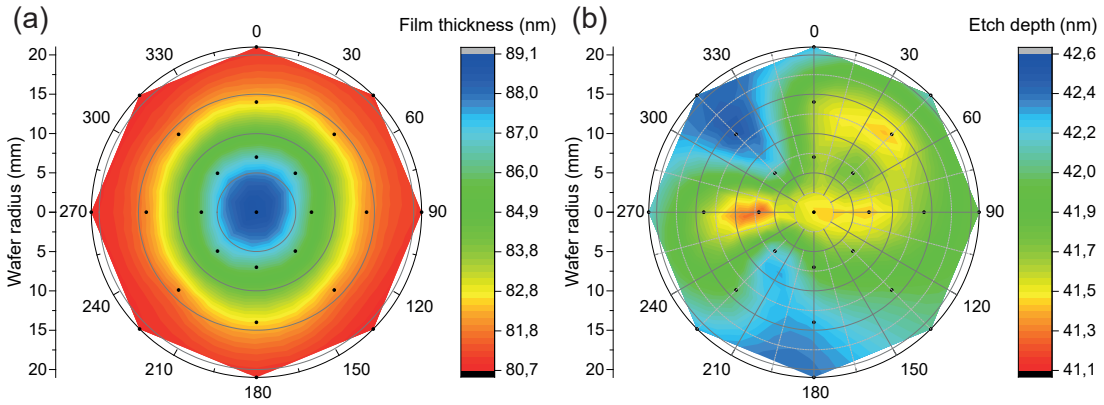

Figure 5.16: Reactive-ion etching homogeneity measurement of the imprint polymer mr-I8000R on a 2-inch silicon wafer. (a) Initial film thickness distribution (b) Etch depth after oxygen RI-etching. The 25 measurement points on the wafer are marked with a black dot.

5.4.5 Undercut formation by lift-off resist etching

The formation of an artificial negative slope of the imprinted polymer profile is achieved by a lateral undercut etching of the lift-off resist. Wet chemical etching is applied for this reason, as it is typically isotropic. First, a suitable chemical has to be found, which selectively removes the LOR against the imprint polymer and also the substrate. AZ 400K from Microchemicals GmbH, Germany fulfills these requirements (in the following referred to as developer). It is based on buffered potassium hydroxide (KOH) and can be easily diluted with DI-water to reduce its etch speed. While silicon can be etched with high concentrated potassium hydroxide, the etch rate of diluted AZ 400K is negligible, and thus the selectivity is high. The etch rate of the imprint polymer mr-I 8000R was tested. Even with undiluted AZ 400K no thickness change of the imprint polymer could be observed. As a consequence, the selectivity of the developer is high, both against the substrate and the imprint polymer.

Soft-bake temperature influence on the development rate The development rate was determined by measuring the etch depth of the LOR over time with ellipsometry. For all measurement points, the developer AZ 400K was diluted with DI-water in a 1:5 ratio. This dilution is chosen to get a stable process with a low systematic error caused by uncertainties with the initial dipping and final rinsing step. The lower the development rate, the smaller is this error. On the other hand, the total development duration should not be too long for obvious reasons. An etch rate around 1 nm/s is suitable for meeting all requirements.

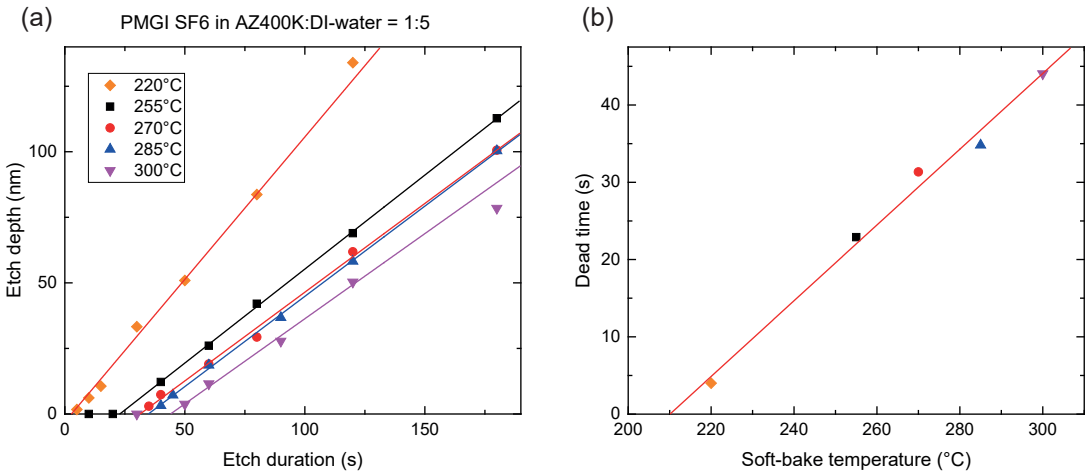

Figure 5.17: Soft-bake temperature-dependent development rates of the LOR PMGI SF6 in AZ 400K:DI-water=1:5. (a) Plot of the etch depth against the etch duration. For soft-bake temperatures above the glass transition temperature of the polymer (T_g=180-210°C), the development rate stabilizes with only a slight decrease in rate with increasing temperature. (b) For soft-bake temperatures above T_g, an inhibition layer is formed resulting in a dead time of the development, which is linearly dependent on the baking temperature.

The soft-bake temperature has a direct influence on the etch rate[54]. The bi-layer process can be effectively controlled with the LOR soft bake time. Spin-coated layers of polymer always have a certain remaining solvent concentration. The soft-bake reduces this content, thus hardening the resist and reducing the development speed. In figure 5.17 (a) the etch depth over time for different soft-bake temperatures is given. For baking temperatures below 210-230°C, the development rate strongly depends on the soft-bake temperature, while for temperatures above 250°C the rate stabilizes to a value of around 0.71±0.02 nm/s when using a 1:5 AZ 400K dilution. The soft-bake time has a minor influence on the development rate as long as it removes the solvent as intended[52].
Figure 5.17 (a) also indicates a dead-time of the development rate. While for soft-bake temperatures below 210°C the etch depth is directly proportional to the etch duration, the etching does not start right away for higher temperatures but is zero for a certain amount of time. This dead time was extracted from the graph and plotted against the soft-bake temperature. As can be seen in figure 5.17 (b), starting from a non-existing dead-time at around 210°C, this duration then linearly depends on a further increase in baking temperature. For the used developer concentration of 1:5 it can be calculated as

$$deadtime[s] = 0.49 \cdot T[^\circ C] - 103 \tag{5.8}$$

The value of 210°C matches exactly the glass transition temperature of the lift-off polymer. When heated above this value during soft-bake, such that it passes through T_g, the film coating becomes denser and further decreases the undercut rate[54]. Secondly, the rate stabilizes and nearly gets constant. Also, an inhibition layer will be formed on top of the polymer surface, which first has to be removed when the sample is immersed in the developer solution and causes this dead time.

The inhibition layer negatively influences a controlled removal and undercut formation in LO-NIL. Although the dead-time can be included when calculating the perfect development duration, it is in principle better to remove the layer before this step. However, it does promote the non-intermixing of LOR and imprint polymer. In the presented LO-NIL procedure, the RIE step to remove the residual layer of the imprint polymer most certainly also etches inside the LOR layer. In fact, in an optimized process, it removes as much of the LOR layer as possible while maintaining shape retention of the nanostructures. As a minimum, the RIE step must be long enough to at least remove this inhibition layer of the LOR of 4-5 nm thickness.

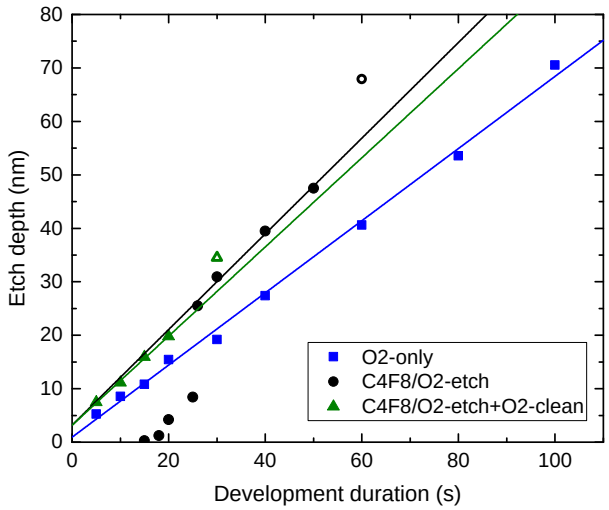

Figure 5.18: Influence of reactive ion etching on the development rates of the lift-off resist PMGI SF6 using AZ 400K (1:5). The LOR was soft-baked at 255°C for 3 min. With oxygen-only RIE the inhibition layer formed during soft-bake is removed, and development starts without delay (dead time). With a C_4F_8/O_2 mixture, a passivation layer is formed, also resulting in a dead time. A short pure-oxygen cleaning step can remove this passivation layer. The fit of the C_4F_8/O_2-Etch series only includes data points where the passivation layer is already removed. Data points with an open symbol were also excluded.

Influence of reactive ion etching on the lift-off resist development rate

The removal of the inhibition layer on the LOR surface can be achieved just by

etching far enough inside the LOR when using the dry-etching method to remove the residual layer of the imprint polymer. However, the RI-etching of the LOR itself can change the development rate. Figure 5.18 shows the etch characteristic with oxygen gas-only and with the passivation process described in the previous section. Therefore samples were coated with LOR and soft-baked at 255°C for 3 min. A pure oxygen etching process was performed with standard parameters (35 W forward power, 150 V DC-bias, 30 sccm, 15 mTorr), but the result is also valid for any other parameter set as well. Here, the inhibition layer is completely removed, resulting in the non-existence of the dead time. The development rate of the LOR is 0.68±0.02 nm/s and thus matches the measured rate without RIE of 0.71±0.02 nm/s. In contrast, with the 2-gas approach using a C_4F_8/O_2 mixture, the inhibition layer caused by the soft-bake of the LOR is also removed. However, the passivation layer, which is formed during the RIE process, still results in a dead time of the development (black circles in the graph) of around 16-20 s. Furthermore, the development rate of the LOR after the removal of this layer is 0.89±0.06 nm/s, thus slightly higher than before. This rate was determined by a fit using only the data points after the removal of the passivation layer, where the development rate is constant. A solution to this problem is to perform a short pure oxygen gas cleaning step directly after the RI-etching step of the sample just by changing the process gas during the RIE process. As the passivation layer thickness was measured to be 4-5 nm thick (5.15 (b)), this step was set to be 5 s long under standard conditions. The development after including this flash cleaning step is marked with green triangles. Again, no dead time is present, and the development rate was determined to be 0.83±0.03 nm/s, thus identical within the error bars to the RI etching without the cleaning step.
Both for the pure O_2 and the C_4F_8/O_2 case, the development rate is slightly higher in the very first seconds (y-axis intercept greater than zero). This is attributed to the surface roughening of the polymer due to the RIE, which is consistent with the larger offset using the C_4F_8/O_2 samples. As discussed before, the 2-gas approach leads to a larger surface roughening compared to the pure oxygen case (figure 5.14). The origin of the generally higher etch rate remained unclear. It is assumed to be either a change of the polymer material or a change in developer efficiency caused by the fluorine content.
In the following, a short oxygen cleaning step was always performed when using C_4F_8/O_2-RIE, and the development duration was adjusted to the slightly higher etch rate.

Figure 5.19 shows a LOR development series of an imprint with a 75 nm pillar

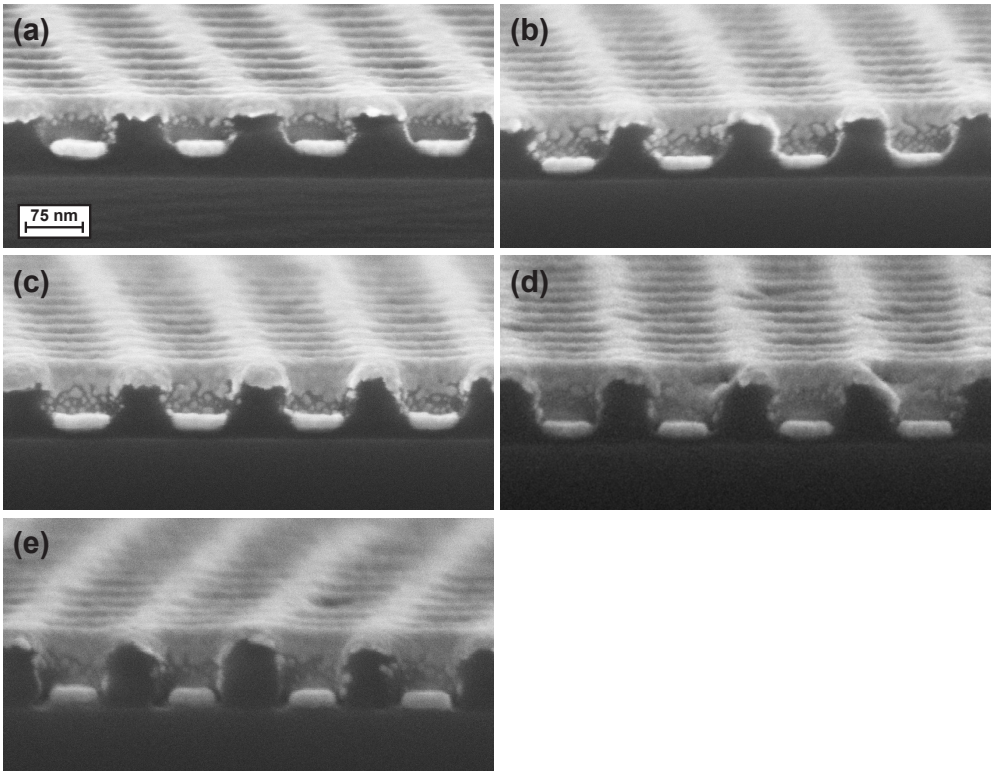

Figure 5.19: SEM images of LOR development of imprinted 75 nm pillars with a subsequent thin gold film deposition. (a) Imprint only (b) Imprinted and RI-etched (residual layer removal) (c) Short development step in AZ 400K (d) Medium long development time. A thin LOR residual layer is still visible (e) Sufficiently long development time. The LOR layer is completely removed in the openings and partially lateral etched forming an undercut.

stamp characterized using SEM. After the process, a thin metal film is evaporated on the samples (bright parts). Figure 5.19 (a) shows the as-imprinted thus unetched case. In (b), the residual layer of the imprint polymer is removed with RIE, where the LOR is also partially removed. In (c), the LOR is shortly developed with AZ 400K in a 1:5 dilution. The metal structures are still embedded in the LOR polymer. Sub image (d) shows the case, where the LOR is nearly removed. Only a thin residual layer is present. (e) The LOR is completely removed, and the imprint polymer is partially underetched. The metal structures on the substrate are clearly separated from the layer on top of the polymer.

Figure 5.20 shows the difference of undercut profile formation in photolithography (a) and LO-NIL (b). In photolithography, the sidewall slope is formed by a declining UV-exposure dose of the resist resulting in a change of development rate in z-direction. Figure 5.20 (b) shows a side view of the artificial undercut formation in LO-NIL using a bi-layer process. The LOR is laterally etched, and a clear separation of the metal layer is visible. Here, the LOR thickness is around

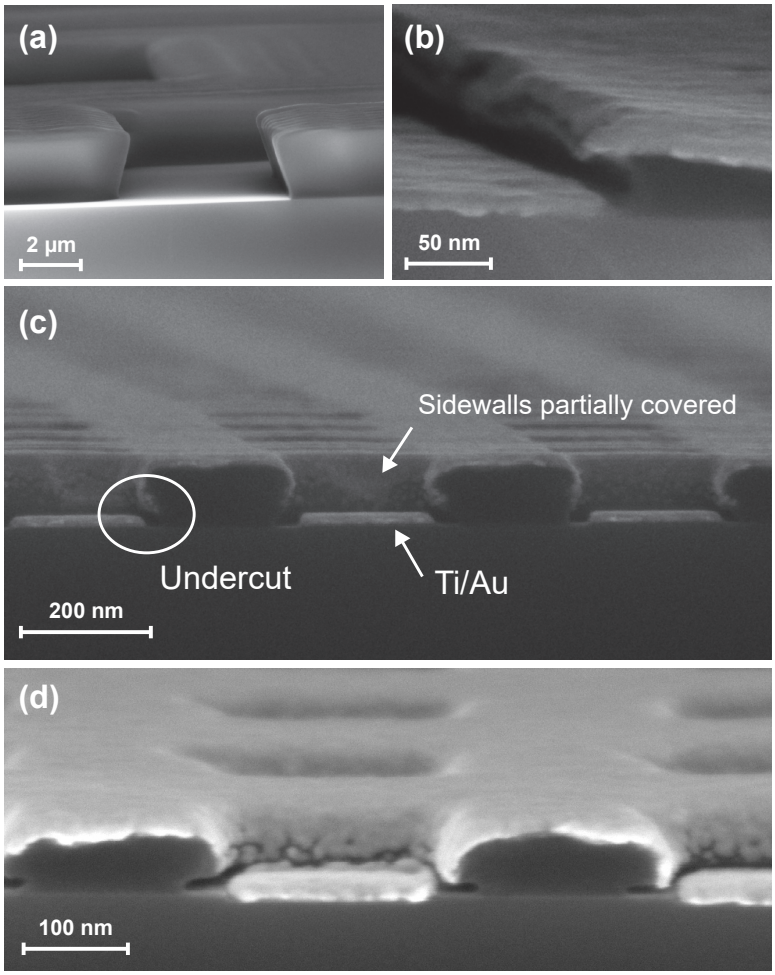

Figure 5.20: SEM images of (a) typical negative sidewall profile of an image reversal resist in optical lithography. (AZ5214E, Microchemicals) (b) Artificial undercut of a bi-layer lift-off system formed by LOR lateral etching. The separation of the metal layer (bright layer) on top of the resist and on the substrate is clearly visible (c) Section of a 200 nm square bi-layer NIL structure before lift-off. Although a partial coverage of the sidewalls of the imprint polymer with the evaporated metal is present, metal layer separation is given. (d) Longer development times lead to a stronger undercut formation (200 nm squares). Adapted and reprinted from Nagel et al.[13] with the permission of AIP Publishing.

30 nm. For longer development times, the undercut gets more pronounced and the lift-off gets typically more stable (figure 5.20 (d)). The SEM image highlights the typical T-shape of the polymer.

The feature inter-distance is the limiting parameter of development time. The lateral LOR etch must be smaller than half the inter-distance (polymer width). Otherwise, the LOR is completely removed. For minimal distances, this critical length is in the same range as the LOR thickness (typically starting with the 45 nm structures fabricated in this thesis). Therefore, the LOR height within the imprinted openings of the resist has to be reduced during the RI-etch step to be

smaller than this critical value.

5.4.6 Metal layer lift-off process

Lift-off after metal evaporation is performed in N-Methyl-2-pyrrolidon (NMP) using an ultrasonic bath, which is heated to 60°C. Typically, lift-off in photolithography is performed in acetone. While the imprint polymer mr-I 8000R can be dissolved in acetone, PMGI SF6 used as a LOR stays unaffected. In fact, acetone can be used to clean the sample only from the imprint polymer layer, when the imprint or the spin-coating process went wrong. The lift-off has to be carried out in a fume hood and with convenient protection as NMP has a teratogenic effect!

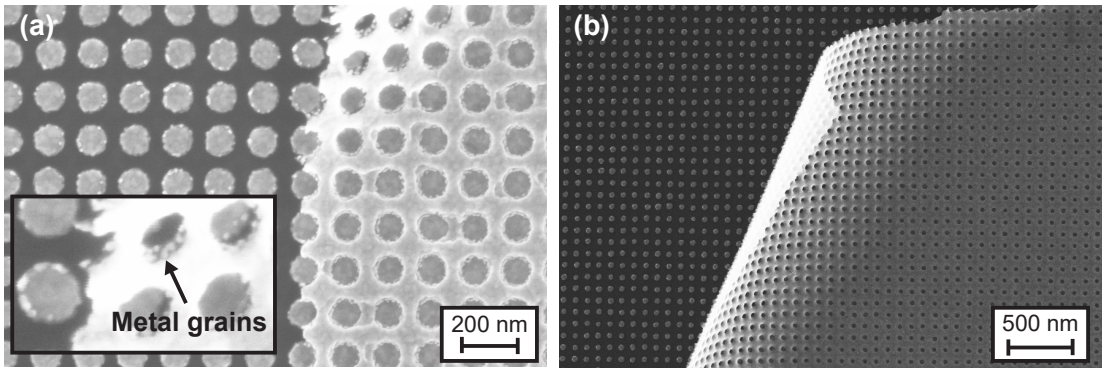

Figure 5.21: SEM images of lift-off process for (a) tuned 75 nm disks. Here, the LOR was slightly too thin, resulting in grain defects on the metal structures. These grains are formed during evaporation on the sidewalls of the imprinted polymer (as can be seen in the inset) and stick to the nanostructures when having contact, thus appearing only at their edges. (b) 45 nm metal disks are formed after polymer dissolution in NMP solvent and metal layer peel off.

In figure 5.21 SEM images of the metal layer peel-off are given. In subfigure (a), the LOR was too thin and consequently the metal layer on top of the resist was not completely separated from the parts on the substrate. As a result, the final metal nanostructures have edge grain defects. These grains are formed during evaporation on the sidewalls of the imprinted polymer (as can be seen in the inset) and stick to the nanostructures when having contact.
The lift-off can take a few seconds up to several minutes, depending on the LOR and metal layer thicknesses. Afterward, the samples are rinsed with acetone and isopropanol and dried using compressed nitrogen.

In figure 5.22 a PVD homogeneity measurement is shown. Especially for nTP experiments, the metal thickness is crucial as it directly influences the yield. A 2-inch silicon wafer was full-scale patterned with micrometer-sized structures using

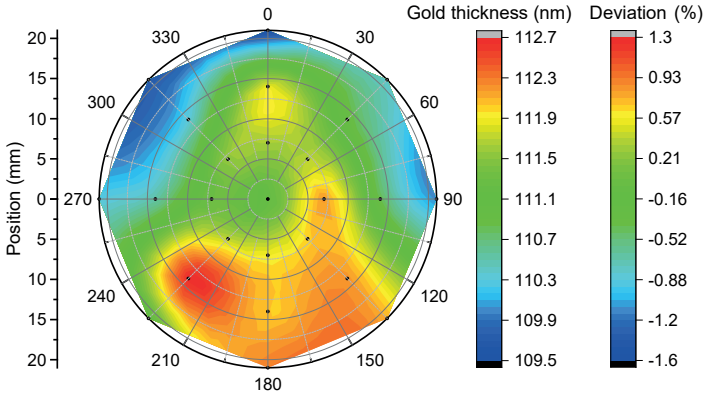

Figure 5.22: Physical vapor deposition homogeneity measurement of gold layers on a 2-inch silicon wafer. A total layer thickness of 111 nm was targeted. The 25 measurement points on the wafer are marked with a black dot.

optical lithography. After PVD, a lift-off was performed, and the metal layer was measured using a stylus profilometer. The individual measurement points are marked with black dots. The sample holder was not rotated during the deposition process. As can be seen, the thickness has a gradient from one side of the wafer to the other end. Overall the thickness deviates by around ±1.5%. A typical metal electrode in this thesis had a thickness of 20 nm; thus, the deviation is in the range of ±0.3 nm, which is acceptable. To improve homogeneity, the substrate holder should be continuously rotated during evaporation to reduce this effect substantially.

5.4.7 Characterization of metal nanostructures fabricated with lift-off nanoimprint technology

The final metal nanostructures were characterized regarding process yield, lateral dimensions, height, morphology, and defects using SEM and AFM. The yield was almost exclusively above 99.9%. It was found that the yield was either that high or the process did not work at all when the LOR layer was not removed completely. Additionally, point defects within the metal array were little to none present. Figure 5.23 gives a representation of a LO-NIL process using a 75 nm pillar stamp. Sub-figure (a) shows a rather large scale overview of the 5x5 mm^2 patterned area close to one corner. The brighter part of the image is covered with gold nanodisks. The area marked red in (a) represents the dimensions of the zoomed-in image of Sub-figure (b). Here, no defects in the more than 11000 disks can be found. The overall yield of the sample exceeded 99.99%. The single gold disks (figure 5.23 (d)) are having nice roundness, homogeneity, and little edge defects.

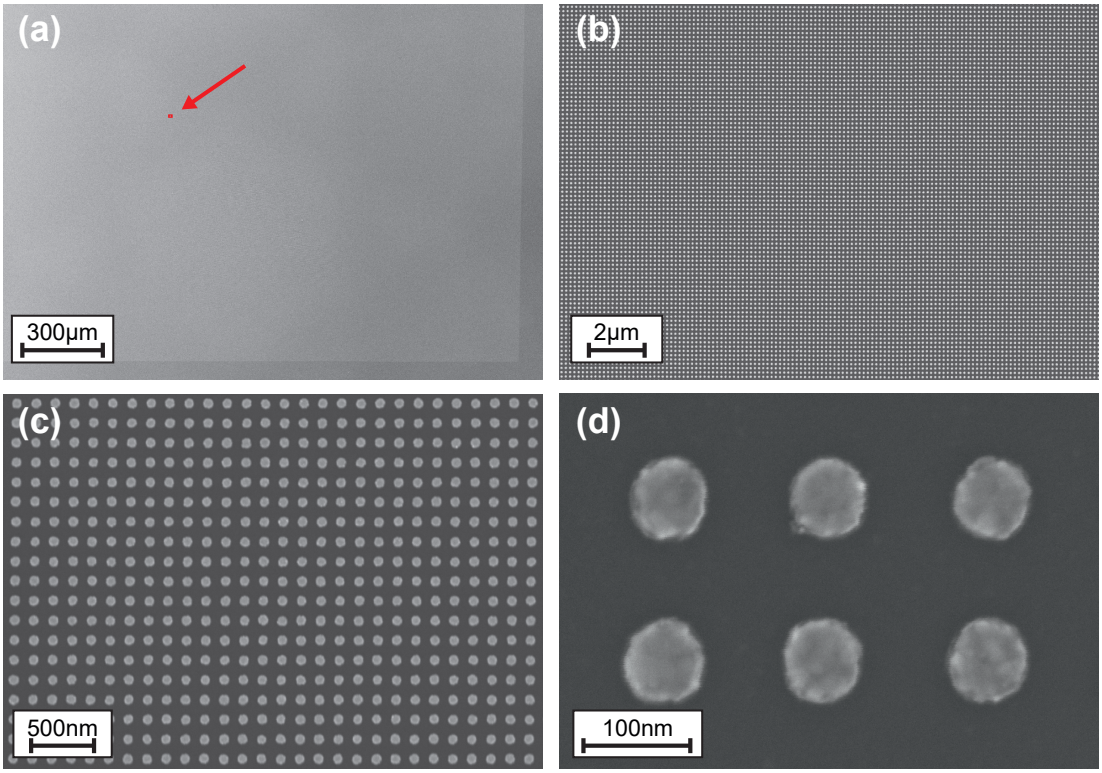

Figure 5.23: Large area SEM images of fabricated 75 nm Au disks with LO-NIL. Images (a)-(d) show parts of the 5x5 mm^2 structured area with different magnifications. The area marked red in (a) represents the dimensions of image (b). The total yield of the sample exceeded 99.99%. Adapted and reprinted from Nagel et al.[13] with the permission of AIP Publishing.

The lateral dimensions were characterized for almost every sample fabricated. In Figure 5.24 the size distribution for non-tuned 75 nm disks is presented. 12 out of 23 samples (52%) had disk diameters within only a 1 nm range (75±1 nm). Furthermore, for 20 out of 23 samples (87%) the disk diameter was exact within a 2 nm range. Surprisingly, one sample showed a decrease in diameter by 5 nm, resulting in only 70 nm disks. This can be explained with an imperfect RIE process, where the deposition of the passivation layer was much faster compared to the standard rates and especially compared to its concurrent etching. Due to the layer growth, the diameter of the imprinted openings decreases. However, this behavior was only rarely observed.

A not to be underestimated advantage of LO-NIL is the possibility to work with very thick metal layers. Just by adjusting the LOR thickness, the metal layer can be increased by typically the same amount. If the lateral underetching is not limiting this thickness, the LOR can be widely tuned. A test sample with 200 nm squares were fabricated, and an in total 61.8 nm thick titanium (3 nm)/gold stack was evaporated. Still, the lift-off was easily possible. Figure 5.25 shows a slightly

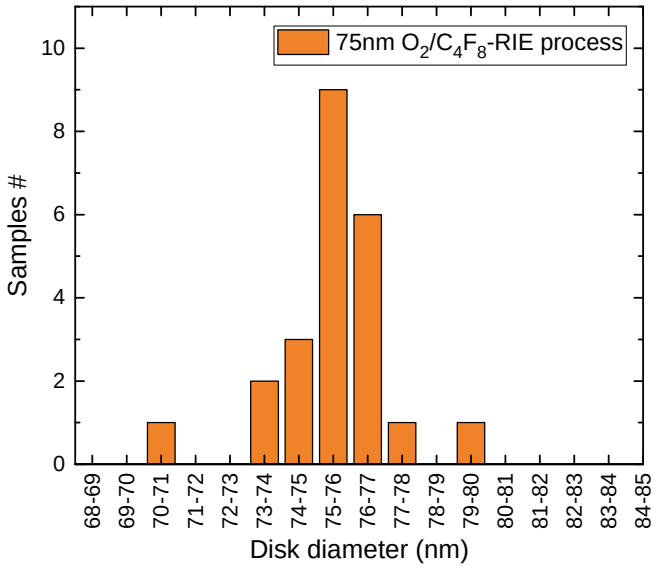

Figure 5.24: Size statistic chart of fabricated metal disks using LO-NIL with initially 75 nm diameter. The passivation RIE process with C_4F_8/O_2 gas mixture is used, and the diameter is determined using SEM.

tilted SEM image of the edge of the fabricated sample. While metal layers that are thicker than 100 nanometers were not needed during this thesis, these kinds of thicknesses are generally required for low resistive interconnects and mechanically stable contact pads. With bi-layer LO-NIL it is possible to reach thickness values above 100 nm, although the wet-chemical development of the LOR will limit the minimal feature size accordingly.

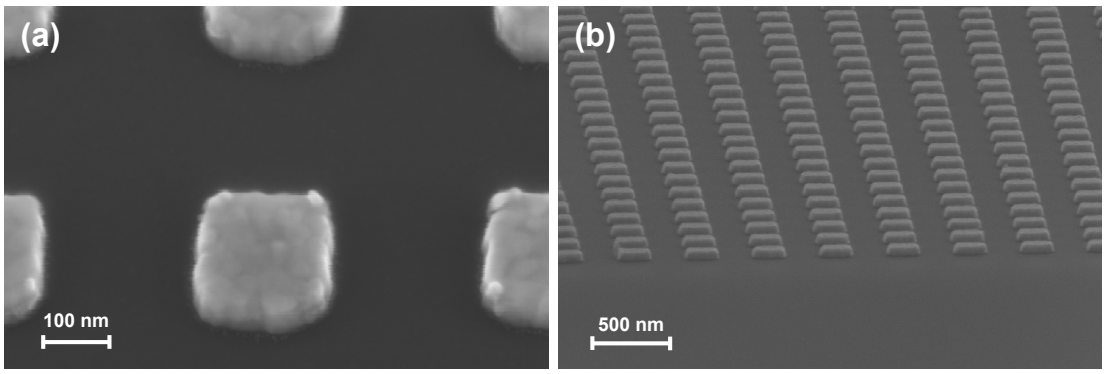

Figure 5.25: SEM image of a comparably thick metal layer lift-off. 200 nm squares with 61.8 nm metal (Ti/Au) layer thickness are fabricated. The images are taken with a slight tilt of the SEM stage.

All-dry-etching lift-off process

The disadvantages of a wet-chemical underetching of the imprinted pattern can be overcome by introducing an all-dry-etch LO-NIL process. Here, the under-

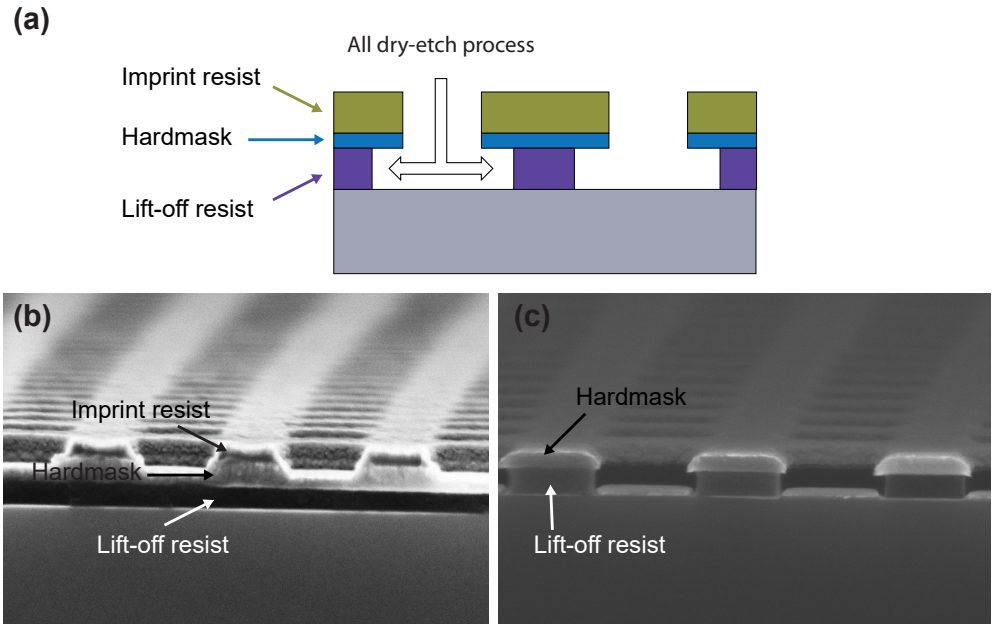

Figure 5.26: All-dry-etch LO-NIL method. (a) Sketch of a tri-layer LO-NIL process, where an intermediate hardmask is used as an etch-stop layer. (b) Sidecut SEM image of a tri-layer process with 200 nm squares. The image is taken after imprint and RIE of the imprint resist and partially etched hardmask. (c) After the pattern is etched through the hardmask layer, the LOR is vertically removed with pure oxygen RIE and also laterally etched to form an undercut.

etching is also performed with RIE, which in general is a more controlled and (more important) a partially anisotropic process. The reason for choosing the wet-chemical approach is the excellent developer selectivity of the LOR versus the imprint polymer. For an all-dry-etching step, a polymer and process gas combination is hard (or even impossible) to find that fulfills the requirements (listed at the beginning of this chapter). In fact, it is even hard to find materials where the RI-etching rates are very different. If found, this would enable large LOR thicknesses and thus deep trench etching, and if also selective against the substrate (which is easier to achieve) the underetching can be performed slowly and controlled. Especially when taking the directed RIE process into account, which results in an underetching rate much slower than the vertical one. This means that this kind of process would enable very thick metal layers and also very small feature dimensions and inter distances.

An approach to overcome the limits of organic polymers is to use organic-inorganic hybrid polymers or to introduce an inorganic hardmask between the imprint polymer and the LOR in a tri-layer process (figure 5.26). In the following, silicon oxide is used as a hard mask. After spin coating the LOR followed by a hardbake, a thin silicon oxide layer is sputtered on top of the polymer. As silicon oxide is not affected by oxygen RIE, this layer can be in principal really thin, however,

it must be thick enough to form a closed layer during sputtering. On top of this hardmask, the imprint polymer can be spin coated and imprinted as usual. A side-view SEM image of the stack with a partially etched hardmask is shown in figure 5.26 (b) using a 200 nm square structured stamp.
The etching can be performed in a single RIE run just by changing the process gases in between. The imprint residual layer and the LOR can be etched with pure oxygen plasma. When the hard mask surface is opened up, the process gas is switched to a SF_6/C_4F_8 combination to etch through the silicon oxide followed by a final pure oxygen etching step to remove the LOR vertically and additionally laterally. Here, the vertical etch rate is much faster than the lateral one. This leads to rather vertical sidewalls, which additionally makes this approach more stable regarding small feature sizes. In Figure 5.26 (c) the vertical LOR sidewalls are visible. As the duration is long compared to the residual layer etching step, the imprint polymer is most likely completely removed here, and the metal is evaporated directly on the patterned hard mask rather than on the imprinted resist. Figure 5.26 (c) shows a sample after metalization and right before the lift-off step. Due to the possible thick LOR layer, the metal on the sample surface and on top of the sacrificial layer is clearly separated.
However, this process has some drawbacks. First, sputtering a hardmask does need an additional processing step, which should be avoided if possible as it is a source for errors, although the introduction of this additional step leads to the elimination of the wet chemical step. The main issue is found to be the hardmask thickness. If too thick, removing it must be highly anisotropic to avoid feature size increase. The bigger problem was the very high edge roughness of the nanostructures. Either the silicon oxide forms larger grains due to the sputter coating or its RIE resulted in such degeneration effects. If a tri-layer LO-NIL is needed, these steps have to be optimized (e.g., spin-on hardmask). As the bi-layer LO-NIL technique worked well for all required samples and structure dimensions, it was chosen to be the primary fabrication process, and the tri-layer approach was developed as a proof-of-principal.

5.5 Summary

In this chapter, a bi-layer lift-off process with nanoimprint technology was developed. A sacrificial layer was introduced between the substrate and the imprint resist, enabling the formation of an artificial undercut of the imprinted pattern in an additional developing step. With this procedure, metal lift-off of thicker

layers is possible with less to none defects and high yield. Furthermore, feature dimensions can be adjusted intrinsically within the RIE process when using pure oxygen plasma, thus reducing the number of needed master stamps. Just by changing to a 2-gas mixture of C_4F_8/O_2, a high-resolution, high-accuracy process can be achieved, where 87% of the nanostructures only deviate by less than 2 nm from the original master stamp.

6 Nano-transfer printing for direct electrode patterning

6.1 Introduction

In this chapter, nano-transfer printing (nTP) is performed and optimized towards sub 50 nm feature resolution and tested for its applicability in electrochemistry, organic electronics, and standard semiconductor device fabrication. As a purely additive printing technique, nTP only deposits metal at predefined locations. It can generate complex patterns with nanometer resolution over large areas in a single process step. What makes nTP particularly interesting is the separation of the patterning and everything which comes along with it (typically, it involves chemicals and solvents) from the actual device. This is especially important for applications where harsh conditions should be avoided (e.g., organic electronics). Besides, it is a very cheap patterning method, which can be easily scaled from the micrometer range to a full wafer level. Our institute has already demonstrated ultra-narrow gaps with etched MBE molds[55] and transfer printed functioning MIM (metal-insulator-metal) tunnel diodes[56]. Stamps for nTP processes are usually one-time-only use due to residual metal on the stamp after printing. Compared to standard silicon stamps used when starting the work for this thesis, a comparatively high number of samples were produced using replicated stamps. The stamp replication technology presented in the previous chapter is used for this purpose, opening up for large scale devices and reliable results since many samples for every parameter set can be fabricated and examined.

Silicon was mainly used as a model substrate because the developed photoelectrochemical cell (PEC) in section 7.5 exactly matches this design and also due to its importance in the semiconductor industry and research. In principle, a variety of substrate materials (glass, plastics, organic polymers, just to name a few) can be used the same way as presented in the following procedure for metal transfer printing with replicated stamps, and some examples are presented at the end of

this chapter.
Parts of this chapter have already been published and taken from these publications.[13,16,57]

6.2 Adhesion principles of nano-transfer printing

Nano-transfer printing is an advanced nanopatterning method, utilizing differences in adhesion strength of metal layers to different surfaces and materials, which should be greater on the receiving substrate than on a structured stamp relief[58].

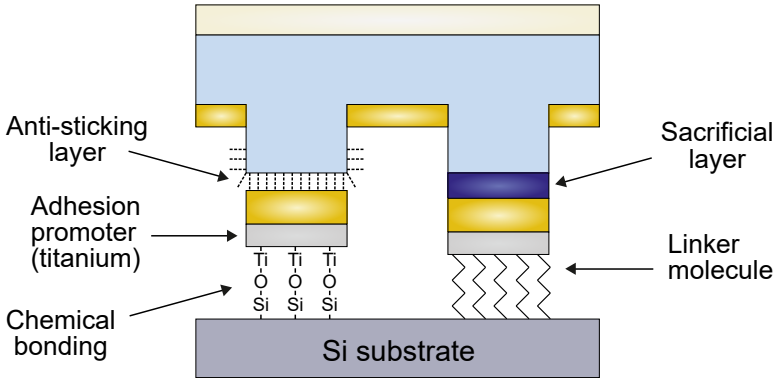

Figure 6.1: Examples of adhesion manipulation in nTP.

The key element for a successful transfer is the control of the adhesion forces. First, it seems reasonable to minimize the force towards the stamp and to maximize it towards the substrate. As the substrate surface is mostly predefined by the device or sample, manipulation options at this part are somewhat limited, yet not impossible. The adhesion properties of the stamp can be intrinsically defined by choosing the right mold material. In addition to that, it can be artificially lowered by introducing an anti-sticking layer, as described in section 3.5. It has to be mentioned that it is not sufficient to have only slightly stronger adhesion forces towards the substrate. The substrate surface is flat in most cases, while the stamp has a 3D relief. This not only results in a larger surface area and thus higher forces, but also a metal overgrowth of the stamp protrusions during the evaporation step can take place, resulting in a clamping effect.
In contrast to using ASL for the reduction of stamp adhesion, it is possible to use adhesion promoters on the substrate side. For metal evaporation, this is typically done by adding a thin layer of chrome or titanium after gold evaporation. In this

work, titanium is typically used. This will result in an antisymmetric metal stack with the adhesion promoter layer only getting in contact with the substrate.
To increase the metal stack adhesion to the substrate, remaining contaminations are removed. If possible, it is additionally treated with an oxygen plasma to remove carbon-based content further, but also to help the bonding by generating hydroxyl groups[59,60]. It was presumed that hydroxyl (-OH) groups on the metal surface (titanol), which is formed in an oxygen plasma with subsequently exposing the surface to air, and hydroxyl groups on the silicon substrate (silanol) undergo a condensation reaction at the contact resulting in permanent Ti-O-Si bonds (figure 6.1)[58]. However, this has not yet been proven incontrovertibly.
Yet, interfacial chemistry can still be used in the form of making use of SAMs as covalent "glues". Just like ASL, similar molecular endgroups can be used for binding to the silicon substrate. Instead of a Teflon-like endgroup a gold binding one can be used, which is typically based on a molecule consisting of a sulfur atom. Loo et al. used 3-mercaptopropyltrimethoxysilane (MPTMS) to transfer gold structures with PDMS stamps[61]. A major drawback of this approach is the need to use chemistry on the sample and a linker molecule can harm the electrical properties and most likely affect its applicability in electrochemistry.

The use of a sacrificial layer between stamp and evaporated gold can be beneficial for a complete transfer. When the stamp is in contact with the substrate, a suitable solvent can dissolve this layer resulting in an easy peel-off. The disadvantage again is the need for chemistry on the substrate (although solvents should not be a problem as long as the substrate does not consist of bio-materials). With this technique, the unwanted metal parts in the cavities of the stamp structure will also be stripped from the stamp. Thus, thorough rinsing of the sample after printing is needed.
In addition to the optimal design of the stamp, the materials themselves and their morphology can be influenced during the nTP process, for example, by changing temperature and imprint pressure.
In some cases, even one of the presented approaches can be used to increase transfer yield. For others, several approaches have to be combined. In this thesis, besides oxygen plasma cleaning, an ASL on the stamp surface and titanium as an adhesion promoter was used for transfer-printing gold structures for electrochemical applications. By this, contaminations of the device surface were minimized and it should be possible to transfer the nTP protocol to any other system.

6.3 Optimization of the nano-transfer printing process on silicon substrates

The stability of OrmoStamp working stamps, together with their uniformity over large areas, enables transfer printing of various structures with challenging aspect ratios and feature sizes. Electrocatalytic systems, in particular, can benefit from sub 100 nm electrode dimensions. An investigation of the nTP approach used in this feature size regime is presented in the following.

With decreasing feature size towards the nanometer regime, controlling the nTP procedure accurately gets more and more important. The boundary length, on which a metal overgrowth leads to larger and larger mechanical sticking forces towards the stamp increases drastically compared to the surface area of the metal, which gets in contact with the target substrate. Hence, a precise knowledge of the process parameters and their effect on the transfer yield is crucial for implementing nTP as a stable and high throughput nanostructuring method. In the following, a thorough investigation and optimization of these parameters are performed by a quantitative analysis of transfer printed Au/Ti-layers in order to be able to evaluate the stability of the nTP method using replicated semi-flexible stamps.

6.3.1 Fabrication

In this part of the work, a silicon master stamp with pillar-shaped structures of 75 nm in diameter, 150 nm pitch, and 100 nm height was used on a five by five mm square structured area. This offers the possibility to investigate the nano-transfer print (nTP) process of structures in the sub-100 nm range as well as the homogeneity and stability of the transfer over a comparably large area. According to the procedure stated in chapter 4.2.2, the master mold was replicated twice in order to obtain a positive working stamp. Silicon p^+-type <100> wafers with native oxide were used as substrates (SiMat).
If not one of the nTP parameters was varied for parameter influence analysis, the following standard nTP procedure was being performed.

1. Metallization: The ready-to-use stamp is coated with a layer of 15 nm gold at an evaporation rate of 3Å/s and an evaporation pressure of $8 \cdot 10^{-8}$ mbar and a 3 nm layer of titanium at a rate of 1Å/s at $4 \cdot 10^{-8}$ mbar. This step is performed in a high-vacuum e-beam physical vapor deposition system

(Leybold 560). The thin titanium layer improves the adhesion of the gold layer to the target substrate (silicon).

2. Cleaning: The target substrate is cleaned in an ultrasonic bath with acetone and isopropanol for 5 minutes rinsed afterward with isopropanol and thoroughly dried with pressured nitrogen. Right before the transfer printing step, the substrate is preconditioned in an oxygen plasma for 6 minutes (200 W, 60 Pa, 100 sccm O_2). After metal evaporation, the up-facing titanium surface on the stamp is treated with an oxygen plasma for 3 minutes (200 W, 60 Pa, 100 sccm O_2). The used plasma treatment for device fabrication should be lower (100-200 W, 1 min)

3. Transfer printing: The stamp is placed with the metal layer facing downwards onto the target substrate and put into a pressure chamber (Obducat, NIL machine). A uniform pressure of 1 MPa is applied via compressed nitrogen. Now, the temperature is raised stepwise to reach 200°C. Then, the pressure is raised to its final value of 3 MPa and this condition is kept for 4 min.

4. Separation: Finally, the stamp is lifted from the substrate. Metal directly in contact with the substrate will adhere to it rather than to the stamp surface.

6.3.2 Characterization

The quality of nTP can be evaluated by introducing the yield factor, which is defined as follows

$$\text{yield} = \frac{\text{number of transferred structures}}{\text{total structures on stamp}} \cdot 100 \tag{6.1}$$

Images of transferred pillars were taken using an SEM (Zeiss NVison40), the number of transferred structures were counted using the image analysis software ImageJ and related to the total numbers of pillars on the stamp in the corresponding area. With this analyzing tool, the evaluation of the images can be semi-automated (shown in figure 6.2). Here, the SEM image is first cropped to an area with a well-known amount of maximum possible structures. Then the image is converted to a black and white image using a threshold method (the resulting image may still have to be inverted afterward). Finally, the build-in "'analyze particle"' algorithm can be used to count and outline the actual trans-

ferred nanostructures (6.2(b)). Particles overlapping with the edges of the image are neglected.

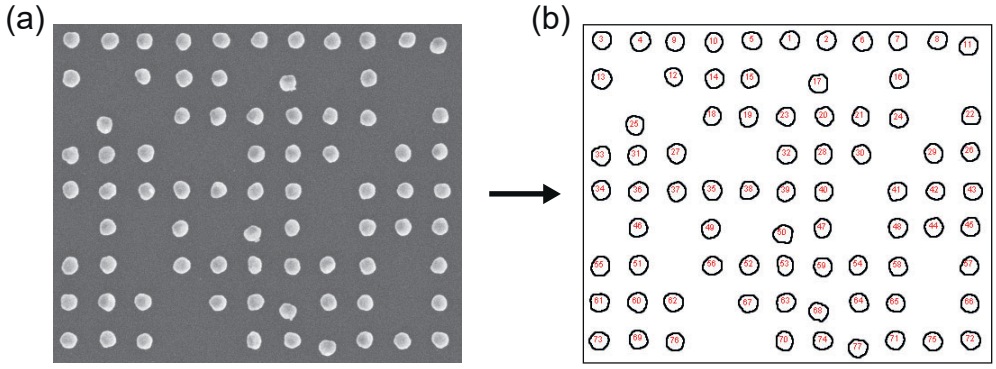

Figure 6.2: Evaluation of nTP yield by counting transferred nanostructures in a defined area of a SEM image typically consisting of above 2000 pillars. (a) subsection of such a SEM image. (b) the structures are outlined and counted by the software ImageJ.

For quantitative analysis, each image consisted of about 2000 pillars, and for each sample, five images in total were taken and evaluated (one in the center and one near to each corner of the squared structured area).

6.3.3 Influence of process parameters on the yield

To gain insight into the behavior and stability of nTP under process parameter changes, all relevant parameters were varied, starting from the standard nTP process mentioned above. The process parameters printing duration, applied pressure, and temperature during the nTP, were chosen to be investigated as well as the pretreatment of substrate and stamp using oxygen plasma activation. A statement about the stability and reproducibility of the process could be made since several samples for each parameter set were evaluated due to the easy working stamp fabrication using OrmoStamp® technology. The result is shown in figure 6.3 (a)-(d). In each subfigure, fixed parameters are listed in the lower right corner.

Temperature Influence

The dependence of yield on the temperature during the nTP process is given in figure 6.3(a). At room temperature, no metal transfer could be observed. It can be seen that the transfer of nanopillars with a diameter of 75 nm only occurs above temperatures of about 50-60 °C. There is a substantial increase in the yield with increasing temperature reaching values above 99% at 250°C over the whole

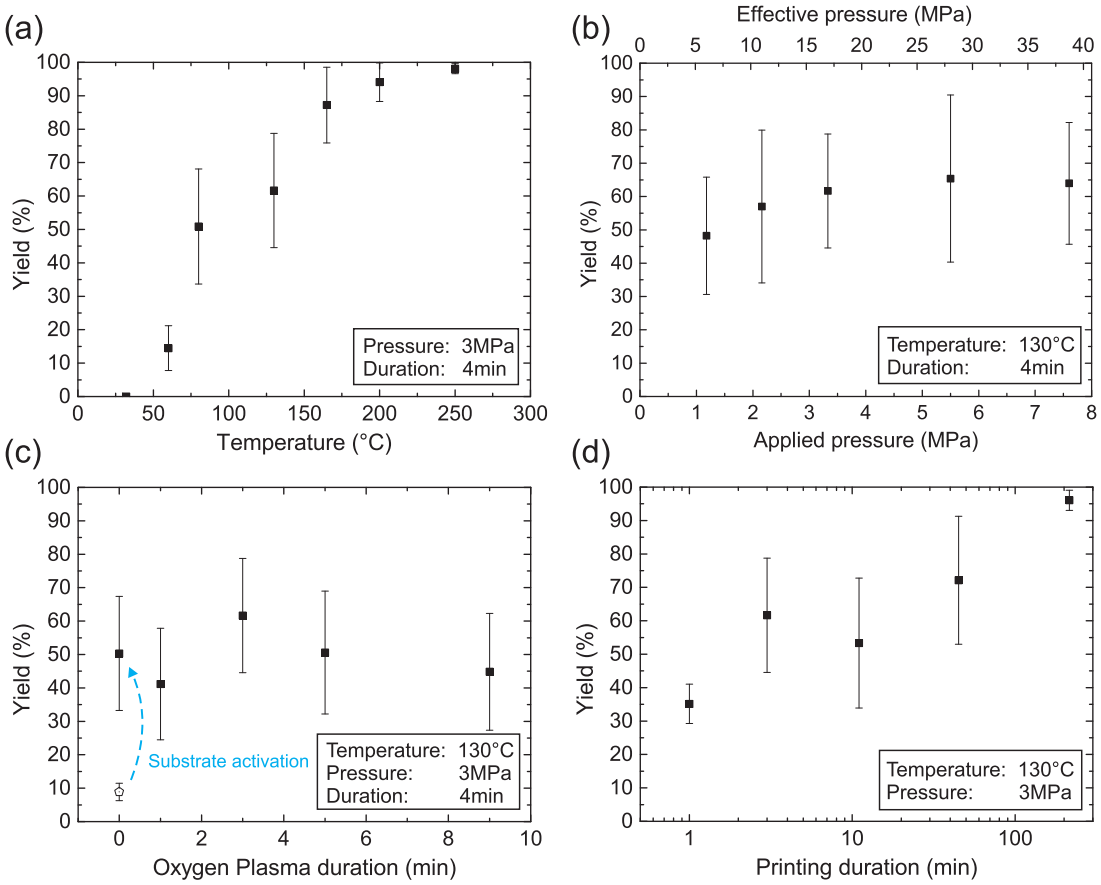

Figure 6.3: Nano-transfer print of 75 nm Au/Ti metal pillars. The resulting transfer yield is shown as a function of (a) temperature during the imprint process, (b) applied gas pressure and the calculated effective pressure below the pillar structures, and (c) oxygen plasma pretreatment duration of the stamp (while keeping a constant substrate activation duration of 6 min). An attempt with neither substrate nor stamp activation is marked with an open symbol, (d) duration of the nTP process. Constant parameters are listed in each sub-figure. Adapted and reprinted from [16].

transferred area. Thus, temperature is one of the main parameters to improve the nTP process considerably. For common nanoimprint stamps made out of silicon or quartz, high temperatures are not an issue, which is not generally the case for polymer materials. According to the manufacturer's instructions (micro resist technology GmbH), OrmoStamp® is chemically and physically stable for long-term thermal treatments up to 160 °C and short term stable up to 270°C[29]. Temperatures up to 250°C were applied in the experiments, yet no changes or damage to the stamp were identified. However, high temperatures with very long process durations could affect the properties of OrmoStamp® and should be avoided. Possible contaminations on the target substrate due to the nTP process are discussed in section 6.7.

The values in the mid-temperature range (80°C, 130°C, 165°C) have a large error bar. While the yield is quite consistent from sample to sample, the yield at the

different measurement points of one sample tends to have a larger uncertainty. A yield of only 51% for the 80°C samples is already indicating an unstable process; thus, it is not surprising that this could lead to spots on the target substrate with very low or even no transfer at all.
While printing temperature might be the dominant factor for a successful nTP, the conditions for examining the rest of the parameters must be carefully chosen. When sticking to the standard conditions with an optimized temperature of around 200°C, it is possible that effects from the variation of other parameters can't be identified. Consequently, in order to be able to evaluate the influence of other process parameters on the transfer yield, a temperature of 130°C was chosen in the following since changes in a specific parameter can lead to a measurable shift of the yield in this temperature regime (6.3(a)). If not explicitly mentioned otherwise, all following variations were carried out in an Obducat nanoimprinter at this temperature with an applied pressure of 3 MPa for 4 min.

Pressure

The imprint pressure of the Obducat nanoimprinter was varied between 1.1 and 7.6 MPa (figure 6.3(b)), corresponding to an effective pressure underneath the protrusions between 6.0 and 38.7 MPa due to the fill factor of the stamp of about 19.3% (75 nm pillars, 150 nm pitch). With increasing pressure, only little improvement in the yield can be observed. Especially when respecting the rather large error bars caused by the lower temperatures used in this series. It can be assumed that sufficient pressure is mainly needed for the formation of intimate contact between the Au/Ti film and the silicon substrate. The experiments suggest that a pressure of about 1 MPa already leads to adequate contact, and it can be assumed that even smaller pressures are feasible. Haeberle showed in his thesis, that transfer printing can also be successful even without any applied pressure when using larger structures with soft and flexible PDMS stamps[27].
This finding is a requirement to perform nTP also on unstable substrates and materials, for which high mechanical stresses can be critical.

Transfer Print Duration

Transfer prints with different process durations have been investigated (figure 6.3(d)). Note the logarithmic scale of the time axis. A significant increase in transfer yield with increasing process time was found. Starting at low yields for 1 min (35.1± 5.8%) and 3 min (61.7± 17%), values of 96.0±3.0% that are comparable to those at a raised temperature above 200°C can be reached applying

only 130°C for a longer time (215 min). Yet, the duration of the process needs to be extended to about 2-3 h, which is contradictory to a fast/high-throughput process.

Oxygen Plasma Treatment

An oxygen plasma is used to clean the contact surfaces of the substrate and metal film as well as for the generation of hydroxyl groups on the silicon surface, which was suspected of favoring a chemical bond between Si and Ti on the elimination of water by Loo et.al[58]. In figure 6.3(c), the stamp activation duration (while keeping a constant silicon wafer pretreatment) and its influence on the transfer yield are shown. The result suggests that nTP is hardly affected by the oxygen plasma treatment of the gold/titanium layer. A constant transfer yield was possible even without an O_2-plasma treatment of the stamp. As a consequence, a mild plasma treatment (100-200 W, 1 min) is sufficient.
An attempt without substrate oxygen plasma activation is marked in figure 6.3(c) with an open symbol. As can be seen, with neither substrate nor stamp activation, the transfer is suppressed reaching only yield values below $10 \pm 3\%$, which is significantly lower than using the default recipe preparation. Since the nTP process was started immediately after the evaporation of the metal films on the stamp, a sufficiently clean surface can already be expected. Transfer prints using some weeks old, already-metal-coated stamps show considerably lower quality results. However, after applying 3 min oxygen plasma treatment right before the nTP, the same yield value as with newly evaporated stamps can be achieved. In contrast, substrate activation was always needed for a high yield.

6.3.4 Transfer printing of gold-only nanostructures

The mechanisms that lead to a successful transfer of metal structures are not yet fully covered in the literature. Most publications assume a condensation reaction of titanol and silanol to form a strong Ti-O-Si bond. However, they all refer to a paper published by Loo et al.[58] where the authors just believe this reaction will take place at the -(OH)-bearing interface. An irrefutable proof of this concept has not been presented so far. Still, it is in general accepted as correct and has been seen as the dominant mechanism for nTP in the scientific community.
In this section, the standard nTP process with an antisymmetric Au-Ti metal stack is compared to a transfer print with a gold-only metal layer. The process is identical to the one described in section 6.3.1. Just the titanium layer is replaced

with a gold one to have the same metal layer thickness, which is important regarding the transfer yield. Here, as gold does not form hydroxyl groups, the yield should be considerably lower.

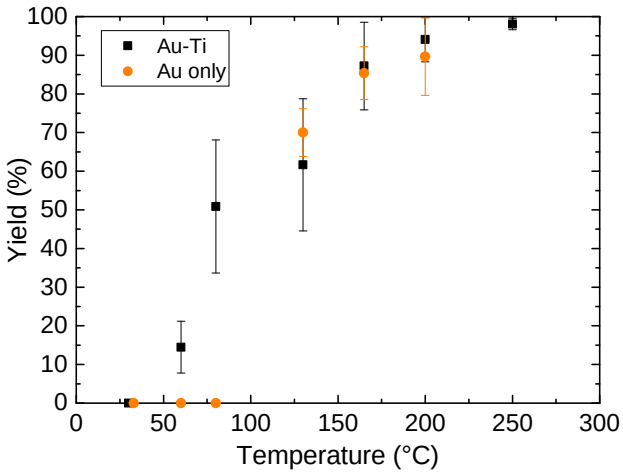

Figure 6.4: Comparison of nTPs of 75 nm Au/Ti and Au only pillars with 18 nm thickness. The resulting transfer yield is shown as a function of temperature during the imprint process. At high temperatures, the yields are equal, while at low temperatures, gold-only samples show no transfer at all.

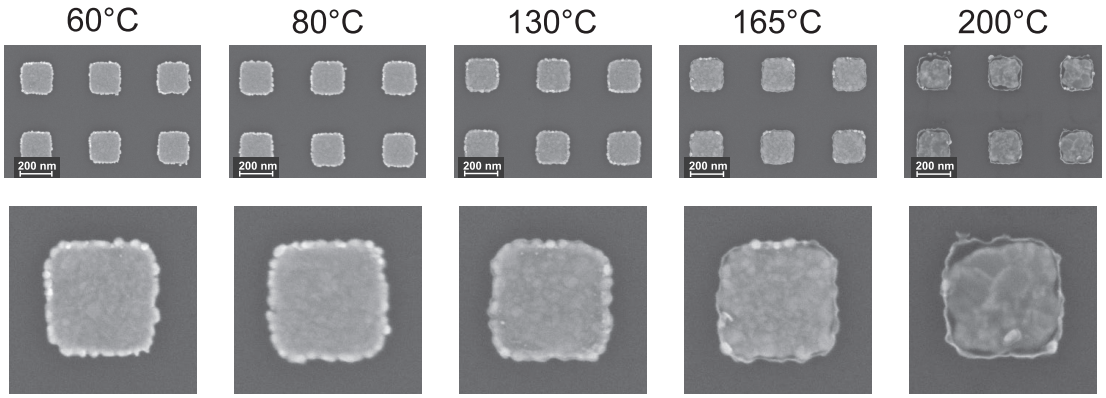

Figure 6.5: Morphology of gold-only nTPs of 200 nm squares with 18 nm metal thickness. Images were taken with SEM.

Figure 6.4 shows the comparison of nTPs of 75 nm diameter disks with 15 nm gold/3 nm titanium and 18 nm gold-only. For printing temperatures above 130°C, the transfer yield of gold-only layers compared to ones including titanium as an adhesion promoter is equal with respect to the error bars. Only in the low-temperature regime, an additional titanium layer has a considerable impact on the yield. To determine the origin of this observation, SEM images of the final

metal structure on the substrate were taken for all different printing temperatures. Here, nTPs with 200 nm squares were performed and used, since changes in the morphology of an individual nanostructure are more prominent and easy to detect. In Figure 6.5 a small overview and a zoomed individual metal square for each temperature are given. Changes in edge roughness and metal cluster size on the surface can be recognized if one carefully compares the SEM images between an increasing temperature step. They are visible when comparing the lowest with the highest process temperature. The metal grain count on the edges of the structure is reduced with increasing temperatures. Additionally, the cluster sizes (typically 1-5 nm in diameter) after evaporation increase at the same time. At 200°C a clear reordering of the gold atoms can be observed.

6.3.5 Discussion

Dissolving an intermediate layer is one way for an easy transfer of metal structures. This would normally include chemical etching, dry etching, or just standard solvents to remove a sacrificial layer. In the experiments presented in this chapter, this approach was not followed because the requirement of using chemicals makes it less versatile and more complicated (using a dry etching method during nTP is even more complex). However, it could be possible that the ASL additionally acts as a sacrificial layer. An end group of this ASL molecule is Polytetrafluoroethylene (PTFE), which can be removed by pyrolysis. It is known that pyrolysis of PTFE is barely detectable at 200°C, and it evolves several fluorocarbon gases and a sublimate[62]. Nevertheless, it is unlikely that this is significant at temperatures below 260°C. The stamp was tested for an intact ASL after nTP by water contact angle measurements, and no change was found, thus the ASL is stable throughout the process and pyrolysis of the ASL is not the origin of the measured increase of transfer yield.

The concept of the formation of a Ti-O-Si bond under the elimination of water is adapted from silicon wafer bonding[63]. Here, two plasma oxidized silicon wafers in contact will undergo this reaction when high temperatures are applied. An intermediate (more complex) bonding stage is reached at around 200°C, and the final Si-O-Si bond is formed at temperatures above 700°C[60]. This finding is in agreement with Howlader et al.[64] He stated a bonding temperature of 600-800°C. In wafer bonding, the out-gassing water is critical. While the first bonding state is water-mediated, this water gets trapped at the interface and will hinder large-scale bonding if not taken care of. In our case of nanostructure transfer, this water would only need to diffuse laterally on the nanometer scale and should not be a

problem. Between 110°C and 150°C adsorbed water becomes significantly more mobile, which will lead to dehydration of the bonding interface and temperatures from 150°C to 600-800°C does little to increase the bond strength.[63] Only above this high temperature, the bond strength gets maximized. Some of these findings are in accordance with the experiments shown in this chapter. The dominant role of temperature during printing is an indicator. However, following this premise does not lead to a higher yield in general. First of all, generating a high density of OH groups on the surface has no observable effect. Using only low intensive and short term oxygen plasma treatment on the substrate and titanium layer showed no difference to high intense treatment, also especially compared to other known methods to create hydroxyl groups like RCA cleaning. During this thesis, samples fabricated with a variety of these methods resulted in equal transfer yields and stability. As shown in Figure 6.3, an oxygen plasma treatment only affected the silicon substrate. While this forms silanol groups, the benefit for nTP can also be attributed to just a cleaning effect by removing carbon bases contaminations. Plasma treatment on the titanium up-facing surface of the stamp results in no improvement of the yield. However, as the titanium surface oxidizes fast already under ambient conditions, titanol groups will also form naturally.

A conclusive disproof of the premise that this condensation reaction plays the dominant role in nTP was performed with gold-only transfer prints. Without a titanium layer and consequently no formation of hydroxyl groups on the surface of the noble metal gold, if the performed experiment results in a comparable transfer yield regarding the standard process, it would be an obvious disproof. The results are surprisingly unambiguous. For higher temperatures, where nTP is more stable, the yield of Au/Ti samples and Au-only ones are equal to the error bars (figure 6.4). Only for lower temperatures, the beneficial effect of titanium as an adhesion promoter comes into play. Here, while Au-only samples show no transfer at all for temperatures below 80°C, it was still possible to have a transfer yield up to 50% using a thin 3 nm titanium layer. The mechanism that causes a successful transfer must be of a different origin.

SEM images of the final gold-only nanostructures on the substrate reveal a change in morphology (Figure 6.5) and a change in surface roughness and grain size. It is believed, that this change of the gold layer favors the high yield transfer. When evaporated on the stamp relief in a vacuum chamber, the metal has the optimal contact and thus the strongest adhesion to the stamp. In addition, the conical overgrowth of the stamp protrusions results in a clamping effect, especially if metal grains growing on the sidewalls of the protrusions get in contact with the

layer on top. A rearrangement of metal atoms will weaken this connection, thus lowering peel-off forces. Although the melting point of bulk gold is 1064°C, melting of gold nanostructures starts at drastically lower temperatures while surface mobility of gold atoms starts even below that limit. Annealing of thin gold layers has been extensively studied. Siegel et al. showed annealing induced changes in morphology and sheet resistance of thin gold layers with annealing temperatures above 200°C.[65] Although the changes below 200°C was observed to be very little, our process environment inevitably promotes changes even at lower temperatures, since added to the temperature high pressures are applied. The SEM images shown in figure 6.5 prove this assumption. There, a change in overall grain size can be observed. Starting from 130°C the grain size starts to grow, which exactly corresponds to the yield improvement at this temperature. Also, the edge grain roughness is reduced. While below 80°C the metal film has to be ripped off when the metal layer is too thick, the rearrangement of gold atoms at higher temperatures already leads intrinsically to a separation of the top metal layer from parts of the sidewalls. This can be detected as the grain defects at the edges of an individual nanostructure are more and more reduced, and the metal boundary is more precise and well-defined. This significantly lowers the adhesion towards the stamp and results in an easy release.
The duration-dependent increase of the yield (figure 6.3) is consistent with this picture. At 130°C, the somewhat unstable process can be improved to reach yields above 96%. While the mobility of gold atoms in this temperature regime is low, extending the printing duration by orders of magnitude can compensate for these limitations. Kane et al. discovered an equal effect when studying annealing effects on gold layers.[66] Changes in gold layers, characterized by measuring sheet resistances, were found during the heat treatment. The identical reduction in resistance at high temperatures could be achieved with low temperatures just by extending the treatment.
The result of this chapter is relevant for devices, where high temperatures would lead to degradation. Although it has to be mentioned, that durations of several hours for a single sample are contradictory to the wanted development of a cheap and fast nanostructuring method.

It is important to mention that the values for the absolute yield very much depend on the target substrate material. However, the basic mechanisms can be applied to other substrate materials as well (as demonstrated in section 6.8.2. As a rule of thumb, nTP on soft materials is easier to achieve. A transfer print

of 45 nm Au/Ti pillars on P3HT (an organic semiconductor) with nearly 100% yield was possible already at 50°C temperature. Soft material adapts well to the surface roughness of evaporated metal and has stronger adhesion properties in general.

6.4 Electrical contact properties and titanium-oxide growth of Au/Ti nTPs on silicon substrates

The electrical contact properties of nTP metal electrodes on silicon substrates are studied in this section. Measurements and samples fabricated with optical lithography defined and directly e-beam evaporated titanium-oxide in this section were carried out by Benedikt Weiler (TUM, Nanoelektronik). Also, when referring to simulations and fits performed by kinetic-Monte-Carlo (kMC) simulations, these are based on his work, which can be found in more detail in his Ph.D. thesis[67]. Parts of this section are reprinted from[57] with the permission of AIP Publishing.

With the standard nTP procedure, plasma activation of the titanium layer is being performed. The influence of this oxygen plasma treatment on the electrical contact properties has to be well-known. Oxygen radicals will certainly oxidize titanium to form an insulation titanium-oxide (TiO_x) layer. This may create issues when charge transfer from the bulk substrate to the metal surface is needed, as is the case in electrochemistry. The oxidized layer must, therefore, be very thin or defect rich in order to minimize negative influences.

The electrical characterization was carried out with a 4-point probe station setup and a low-noise Keithley K2460a. To overcome problems with contacting thin metal layers, a liquid metallic droplet of InGa eutectic was used to ensure a soft contact. All jV-curves shown in figure 6.6 are statistical averages of 15-23 individual measurements. Rather large metal pads were fabricated for these experiments to ensure large currents and thus lower uncertainties compared to nanometer-sized structures. 200 μm x 200 μm-sized Au/Ti/TiO_x-pillars were transferred on a p+-Si substrate. The thickness of the titanium layer was chosen to be 5 nm and 10 nm, while only the 5 nm set is presented in this section. This is slightly thicker compared to the standard nTP process to account for a possibly large TiO_x growth. The titanium layer on the stamp was plasma-oxidized in an oxygen barrel etcher for different durations and powers. To roughly quantify the thickness of TiO_x , the nTP samples were compared to samples fabricated

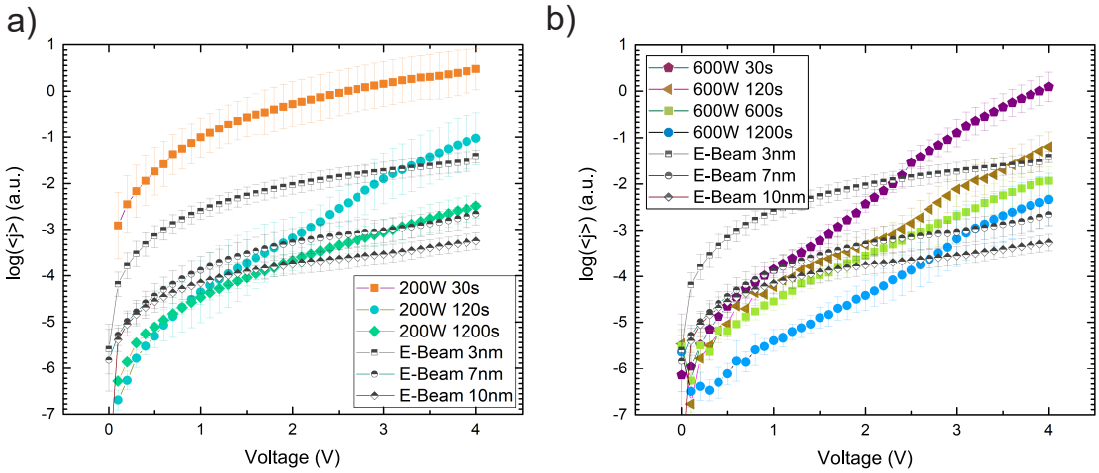

Figure 6.6: jV-characterizations of transfer printed 200μm x 200μm Au/Ti/TiO_x/p^+-Si junctions with negative bias V at the top contact. An initial 5 nm titanium layer is plasma oxidized with different rf-powers and durations and compared to measurements of directly evaporated and optical lithography defined Au/Ti/TiO_x pads with TiO_x thicknesses of 3 nm, 7 nm or 10 nm. This graph is adapted and reprinted from Weiler et al.[57] with the permission of AIP Publishing.

by optical lithography on identical substrates, where the TiO_x layer was e-beam evaporated directly from a precursor by a process like the one reported in[68] instead of being plasma-oxidized grown after evaporation. Samples with 3 nm, 7 nm, and 10 nm TiO_x thickness are shown in figure 6.6. Thus comparing these curves to the plasma-grown nTP MOS-samples allows estimating the oxide thickness for different oxygen plasma activation treatments. In figure 6.6 a clear trend of decreasing current densities with a more intense plasma treatment is visible. This already indicates the formation of an insulation layer between the semiconductor and the metal. Its formation depends on the electrical work of the applied oxygen plasma. The thickness of this layer can be larger than the original titanium layer as oxygen atoms are incorporated in this layer while titanium is gradually oxidized to amorphous TiOx. In literature, a growth factor of about two is reported for annealed Ti films[69], but in theory, up to a factor of 3 is possible. From the comparison, samples with the strongest treatment of 1200 s at 600 W have an estimated thickness of about 13 ± 2 nm. This was confirmed by Weiler et al. with kMC simulations[57].

The main problem of too intense plasma treatment is obvious. It reduces the current density by up to four to five orders of magnitude as electrons have to tunnel through this insulating layer, whereby the probability for this is exponentially dependent on its thickness. Also, it must be noted, that the current density decreases the most with additional plasma work when having the weakest treatment. This is due to the self-limiting character of oxide growth, as oxygen atoms

have to diffuse through the already formed TiO_x, which is more and more limited for thicker layers. However, for samples with the weakest applied oxygen plasma treatment of 200 W for 30 s the TiO_x layer was simulated to be negligibly thin if present at all. This was also concluded from its Schottky behavior, a linear j-$V^{1/2}$-plot for low Voltages followed by a linear ohmic characteristic and finally a space-charge-limited current characteristic with a linear j-$V^{1/2}$ dependency[57]. This usually indicates a metal-semiconductor contact (MS-contact) or MOS-contacts with a very thin and defective interface.
As a result of this experiment, the intensity of plasma activation in nTP for electrochemical and photocatalytic applications should be kept as low as possible (100 W for 1 min should be sufficient). This is in accordance with the finding of the yield experiments presented in the previous sections since activation of the titanium layer plays a subordinate role in nTP. Thus plasma treatment can be adjusted to be low intense without affecting nTP yield and properties. However, for applications where MOS-structures are needed, this is an advantageous method to produce devices with well-defined oxides just by varying oxygen plasma work.

6.5 Nanostructure shape retention

The developed nTP method includes a twofold replication starting from a master mold and additionally a final transfer print. Therefore, it is important to examine how the dimensions of the final shape on the target substrate change compared to the original one. Shape retention of the working stamp nanostructures compared to the silicon master has already been shown in the previous chapter. In figure 6.7, a comparison of (a) the master and (b) the final metal transfer is given. The diameters of the pillar structure just slightly increase from 73.4 ± 0.9 nm (silicon master) to 75.3 ± 1.6 nm (transfer-printed metal) (Table 6.1). This increase is contributed to the expected conic growth of the deposited metal layers during the evaporation rather than a pillar diameter change during the replication process. Also, the measured increase in diameter by 1.9 nm is just close to the uncertainty of 1.8 nm. The thickness of the metal film evaporated on the stamp was measured with an AFM and compared to the transferred metal structure height on the target substrate. In both cases, the same thickness of 20.3 nm was found within an uncertainty of ±0.7 nm. This proves a complete transfer of the metal from the stamp to the target substrate as well as a working anti-sticking layer, which was applied on the stamp surface. Overall, shape retention is almost perfectly given.

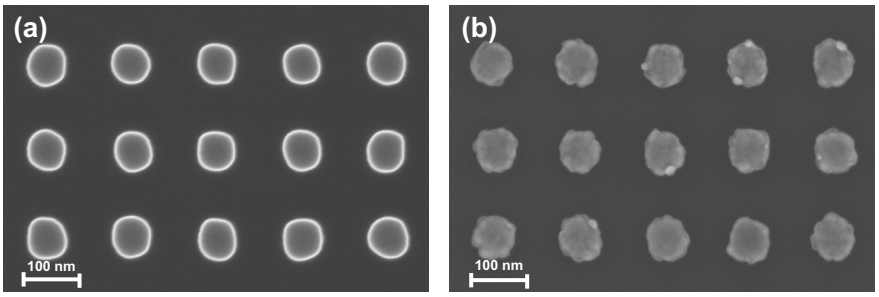

Figure 6.7: Shape retention characterization. SEM image of a pillar structured (75 nm diameter and 150 nm pitch) (a) silicon master and (b) transfer printed Au/Ti pillars. Reprinted from [16].

Table 6.1: Diameter change.

	Master	nTP
Diameter (nm)	73.4±0.9	75.3±1.6
Difference (nm)		1.9±1.8 (+2.6%)

6.6 Common defects and defect tolerance in nano-transfer printing

6.6.1 Defect tolerance using semi-flexible hybrid templates

Even when working in a cleanroom, contamination of surfaces cannot be avoided completely. Already small particles can lead to a breakage of rigid stamps or substrates. The advantage of the used stamps made out of OrmoStamp® is their semi-flexibility. While the polymer can sustain its high aspect ratio pattern on the nanometer scale without roof- or lateral collapse, it is still flexible enough on larger scales to overlay even micrometer-sized particles. This defect tolerance leads to defect areas only in close vicinity of these contaminations (figure 6.8 (a)), thus increasing the yield of the transfer print or imprint. The defect area depends on the height of the particle. As observed, the unstructured distance from the contamination is on the same length scale as their height.

6.6.2 Common defects in nTP

Imperfect nTP conditions can lead to different types of defects. The most common ones are presented in the following.

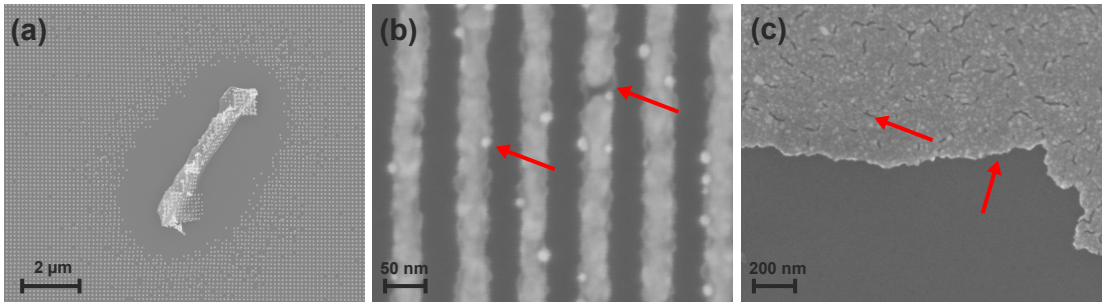

Figure 6.8: SEM images of (a) defect tolerance of nTP (75 nm pillars): The transfer is only hindered in close vicinity of impurities. (b) grain defects on the edges of transfer printed 40 nm wide gold lines and interruptions if the metal layer is too thin. (c) rip-off of large area pads and hole defects within a gold layer. Adapted and reprinted from [16].

Grain defects

Grain defects typically occur only on the edges of the transferred structures. Figure 6.8 (b) shows such defects (marked by an arrow). They are caused by metal evaporated on the sidewalls of the protrusions of a stamp. There, a small amount of metal does not form a closed layer but individual grains. If these grains have contact with the top metal layer, they will stick to it and thus are transferred to the substrate. This is why these defects are only observed at the edges. In most cases, they will not influence the properties of the device. Only if a well-defined and known morphology is needed, the resulting change in surface area and maximum curvature may be an issue.

Change of shape

A change of shape of the final metal structure compared to the master can have different causes. As described in section 6.3.4, gold atom reordering due to high temperatures and pressures can lead to changes from the original shape (figure 6.5), where typically sharp edges are smoothed, and the total surface area shrinks. The reduction of corner sharpness can also be caused by metal evaporation since a lateral growth for thicker metal layers has the same effect.

Hole defects

Hole defects were only found for large metal layers and structures above 500 nm width. It is believed that lateral mechanical stress induced by thermal expansion during the process will result in relaxation by forming these holes. In figure 6.8 (c) an SEM image of a metal pad is given with a high density of such defects. The stress in separated nanostructures is minimal, and consequently, this type of

defect is unlikely to occur.
For a very small feature width below 50 nm, interruptions can take place (6.8 (b)), which are critical for electrical interconnects. It can be avoided by increasing the metal thickness.

Delamination and layer rip-off

On a larger scale, two defect types are often seen: First, if the adhesion towards the substrate is weak, the transferred metal layer can delaminate even if the nTP process was successful. Most commonly, delamination is caused by mechanical stress induced by scratching/touching the surface, but also when post-cleaning a sample by rinsing with acetone/isopropanol.
A layer rip-off can occur when separating the stamp from the substrate after nTP, and it is caused by a weak cohesion of the metal layer. Especially when the adhesion towards the substrate is low or high towards the stamp surface. In figure 6.8 (c), such a defect of a contact pad is given. High-density hole defects can result in an increased probability of this defect occurring.

6.7 Contamination-free sample fabrication for electrochemical applications

As shown in the previous chapters, nTP opens up the possibility to fabricate large areas with sub-50nm metal structures. For usage in electrochemistry, special requirements have to be fulfilled. As electrochemistry and photoelectrochemistry presented in this thesis are, in most cases, heterogeneous catalysis, chemical conversions happen in direct contact with a surface of the fabricated device. Thus, the systems react very sensitively to material changes, surface changes, and surface contaminations. In the following, surface contaminations formed during the nTP process using replicated Ormostamps are examined.
A convenient tool used for this purpose is X-ray photoelectron spectroscopy (XPS), a surface-sensitive quantitative spectroscopic technique. When a specimen is irradiated with a beam of X-rays, XPS detects only those electrons that have actually escaped from the sample surface into the vacuum of the instrument and reach the detector. Photo-electrons generated deeper within the sample must therefore travel through the sample and can undergo for example inelastic collisions, recombination, recapture, or trapping in various excited states within the material. These effects appear as an exponential attenuation function as the

depth increases, resulting in an exponentially surface-weighted signal. The XPS spectra obtained are thus typically from the top 0-10 nm of the material being analyzed, making it especially useful for studying surface contaminations after the nTP process.

If the sample is non-conductive, a calibration of the spectra is needed surface charging leads to a shift of the measured peaks. This is done using carbon-based and oxygen-containing contaminations, which usually all samples contain when exposed to the lab environment. Here, additionally, a silicon dioxide peak was used, since all samples at least partially containing this material, and the resulted peaks are well-defined, because of the rather high amount of SiO_2.

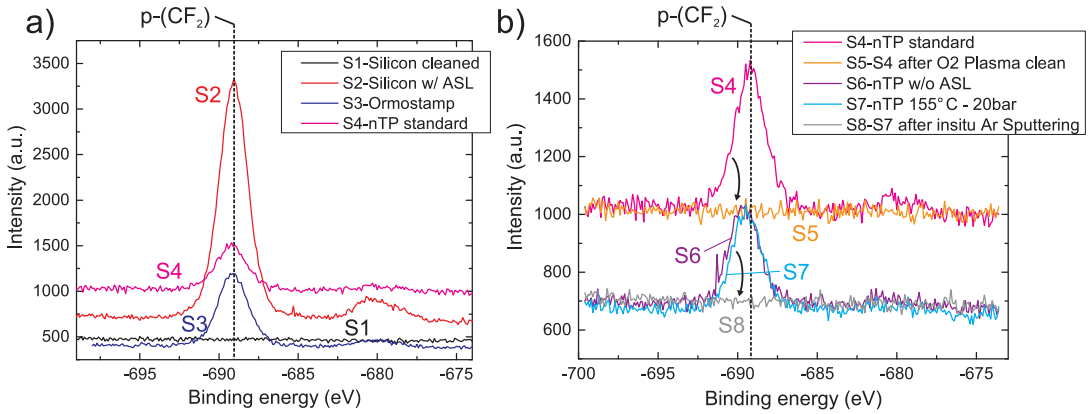

Figure 6.9: XPS spectra of a carbon-fluorine chain (CF_2) peak. The peaks in (a) provide information about the presence of residual anti-sticking molecules. As a reference, a native silicon wafer shows no intensity at this binding energy. (b) study of the cleaning process after nTP. A standard O_2 plasma clean completely removes those contaminations.

Eight samples are shown in Figures 6.9 and 6.10. First, as a reference, an out-of-the-box silicon wafer (including a native oxide layer) is cleaned and is depicted as Sample S1. A second wafer is coated with Perfluorooctyltrichlorosilane (anti-sticking layer) named S2 and a ready to use OrmoStamp working stamp is characterized as Sample S3.

Then, nano-transfer printing is performed using 75 nm Pillars on a 5x5 mm^2 area with evaporated 15 nm gold and 3 nm titanium under standard conditions (200°C, 30 bar, 4 min) without a further cleaning step (Sample S4) and with an additional O_2 plasma cleaning step (200W, 3 min) (Sample S5). To distinguish contaminations originating from the ASL, an nTP using an OrmoStamp without an ASL is performed (Sample S6). In order to estimate the thickness of the contamination layer, a sample (Sample S7) was treated in situ with argon sputtering inside the vacuum chamber while measured with the XPS (Sample S8).

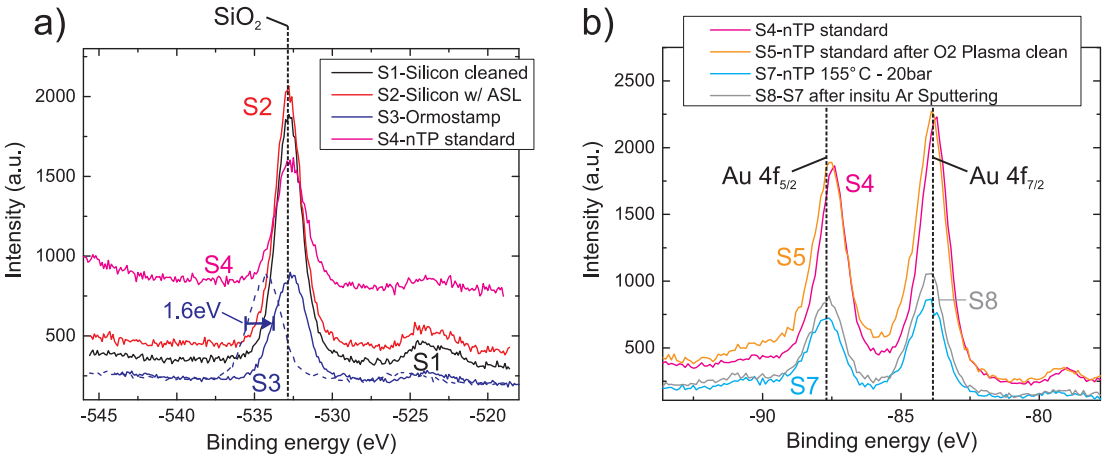

Figure 6.10: XPS spectra of a) a silicon oxide peak and b) a gold peak. The SiO_2 peak was used as a calibrating spectrum of non-conductive materials. The gold peaks in b) prove a degradation-free cleaning method using 2 plasma.

Only the OrmoStamp sample S3 is non-conductive and must be corrected for data evaluation. As shown in figure 6.10 (a), a constant shift of 1.6 eV is present, and the binding energies of the peaks are corrected accordingly. All other samples are already perfectly calibrated.

To identify contaminations caused by the stamp, a unique identifier in the stamp material has to be found. A sulfur peak could be identified in the OrmoStamp material. Yet, this peak was minimal, and it would hardly be possible to get a sufficiently large signal from monolayer contaminations on the sample. The biggest signal originated from fluorine content. OrmoStamp has special molecules implemented, acting as release agents during the demolding step. These molecules have a Teflon-like character and thus are based on polytetrafluorethylen (PTFE) with a high amount of fluorine atoms. The individual peaks at around -689 eV can be found in figure 6.9. The disadvantage of this identifier is the indistinguishability of the stamp material from the ASL, whose endgroup is also based on the same fluorocarbon. To account for this problem, an nTP using a stamp without ASL is performed and discussed later in this section.

Using this peak, the origin of the contamination can be identified. With a blank and cleaned silicon wafer (S1), used as a target substrate for all further nTPs in this experiment, no fluorocarbon content is being found. This is an essential requirement for the interpretation of the measurement and shows that these molecules can not be attributed to lab environment contaminations. As a reference, sample S2 shows a defined fluorocarbon peak, proving the effectiveness of the ASL process.

6.7.1 Discussion

First, the standard nTP process (S4) with the resulting transfer printed 75 nm titanium-gold disks shows a small fluorocarbon peak in the XPS signal (figure 6.9 (a)+(b)). Although the OrmoStamp material should be temperature stable at 200°C and even short term stable at 270°C (according to the manufacturer processing guidelines[29]), a degradation of the stamp material can't be excluded due to the high-pressure environment during printing. As an unstable ASL would result in the same type of contamination, an nTP without ASL is shown in figure 6.9 (b) as sample S6. Again, contamination of the silicon surface was found. Consequently, the contaminations after nTP originate from the stamp material or a combination of stamp material and ASL molecules. This unwanted degradation not only is a general problem for metal nanostructuring. Especially for heterogeneous electrochemical applications, this can have a huge impact on the functionality of the device, as EC is a highly surface-sensitive physical chemistry. While OrmoStamp itself is chemically inert, the surface coverage due to the contamination leads to a shielding effect and unevaluable measurements. To work around this problem, an nTP at lower temperature and lower printing pressure was tested. Yet, reducing the temperature from 200°C down to 155°C and the pressure from 30 bar to 20 bar, respectively, does not have a greater impact on the reduction of contaminations, as shown in figure 6.9 (b). Still, a defined fluorocarbon peak is present. Unable to further reduce the process parameters without affecting the transfer yield (section 6.3.3), the post-cleaning of the samples was examined. Standard solvent cleaning of the sample can't be applied as cured OrmoStamp isn't solvable (only a peel-off can be triggered). Hot piranha etching is an option for removing but not suitable here. First, it could harm the nanostructures, and secondly, it will certainly oxidize the silicon surface. In this work, cleaning based on a dry etching method was chosen, having the advantage of a fast and controllable process. For that reason, it is especially important to know the thickness of the contaminations in order to choose correct etching durations. If the contaminations form clusters, dry etching might not be applicable. This was checked by in situ argon sputtering while measuring with the XPS. Transfer print sample S7 was used for this purpose after the initial XPS characterization. While still inside the vacuum chamber, an argon sputtering procedure was performed corresponding to a removal of <10 monolayers of soft material. Directly after this treatment, the XPS characterization was again performed (Sample S8). As can be seen, the contaminations were removed entirely during this short cleaning procedure, proving the existence of only a very thin contamination layer without

bigger clusters.
Besides using Argon plasma, oxygen plasma cleaning can also be utilized. As this is one standard cleaning process for substrate cleaning, it would be beneficial to stick to this type as it is well known and already used in steps before and after the nTP step. In figure 6.9 (b), Sample S5 shows a standard nTP sample after a mild O_2 plasma cleaning step using a barrel etcher. Like with argon, the sample can be perfectly cleaned from stamp material contaminations. As an important note: Typically, pure oxygen plasma should not be used to etch OrmoStamp as porous SiO_2 will be formed. For such a thin layer this is not an issue, since within a barrel etcher, oxygen plasma not only etches chemically but additionally to some fraction in a physical manner (sputtering).
It is important to check the gold nanostructures for degradation after this cleaning step. Therefore, the gold XPS peak $Au\,4f_{5/2}$ and $Au\,4f_{7/2}$ before and after the process was compared. In figure 6.10 (b) it can be seen that the gold peaks are nearly identical before and after the plasma treatment. In fact, after the cleaning step, they are slightly larger. Although an accurate quantitative analysis of signal peaks of different measurements with XPS is complicated and thus this observation has some error margins, qualitatively speaking it is not surprising that for samples with no nanostructure degradation the peaks after cleaning are larger, since the removal of a surface contamination layer leads to a stronger XPS signal due to a reduced damping caused by it. In addition, images were taken with SEM and AFM, and no change of shape or height of an individual gold structure was observed.
Consequently, an O_2 cleaning step was performed after each nTP, leading to a ready-to-use sample for (photo-)electrochemistry.

6.8 Nano-transfer printing with optimized process parameters

6.8.1 Sub-50nm structures

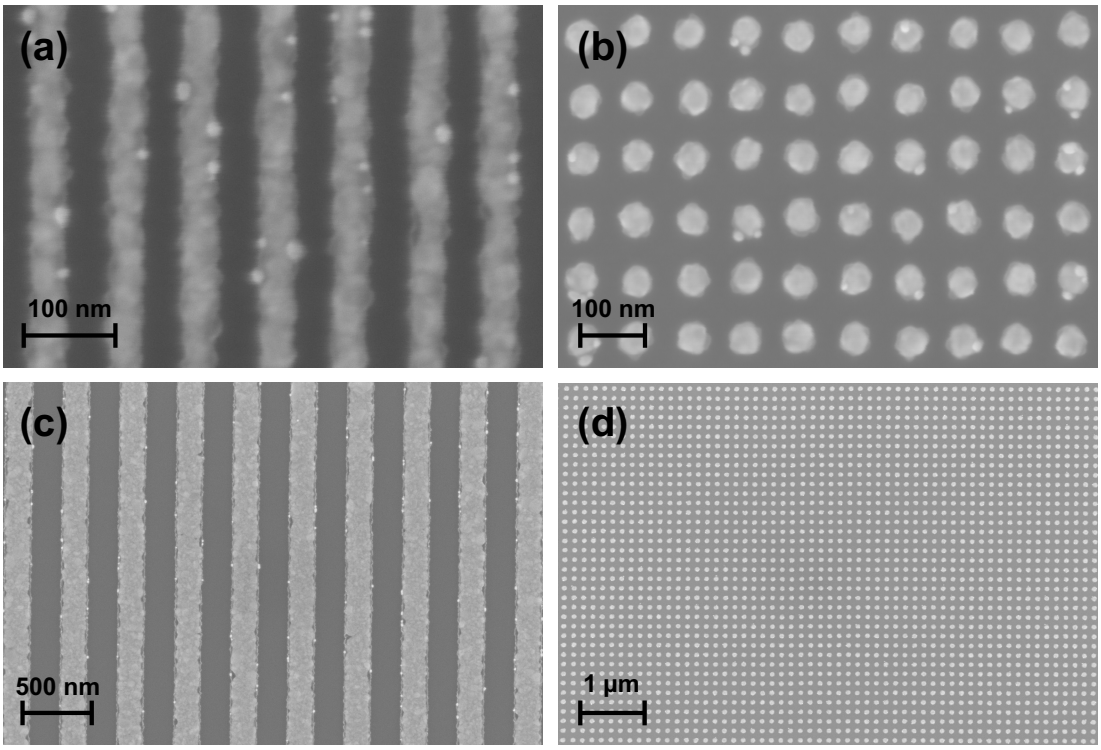

Figure 6.11: Nano-transfer print of various Au/Ti metal structures on a Si substrate with native oxide. (a) 40 nm line width and 80 nm pitch, (b) 45 nm pillar diameter, 90 nm pitch, (c) 200 nm line width, 400 nm pitch, and (d) 75 nm pillar diameter, 150 nm pitch (standard stamp used for process parameters evaluation). Reprinted from Nagel et al.[16]

In figure 6.11, SEM images of transferred Au/Ti lines and pillars with different dimensions are shown. Optimized process parameters found in section 6.3 (200°C, 3 MPa applied pressure, 4 min printing time, plasma activation: 3 min stamp/6 min substrate) were used, and homogeneous transfer of the entire structured area was obtained. Lines with 40 nm width and 80 nm pitch can be easily achieved, demonstrating the potential of the nTP process with cheap semi-flexible replicated stamps in the sub-50 nm range. For electrochemical experiments, lines with widths between 40 nm and 500 nm (width:inter distance = 1:1) were fabricated on a 5x5mm^2 structured area, and circular pillars of 45 nm and 75 nm in diameter (diameter:inter distance = 1:1) as well as squares between 200 nm and 1400 nm width (the inter distances of the squares were designed to match the filling factor of the pillar stamp of approx. 19.6%).

6.8.2 Large Area Transfer Print

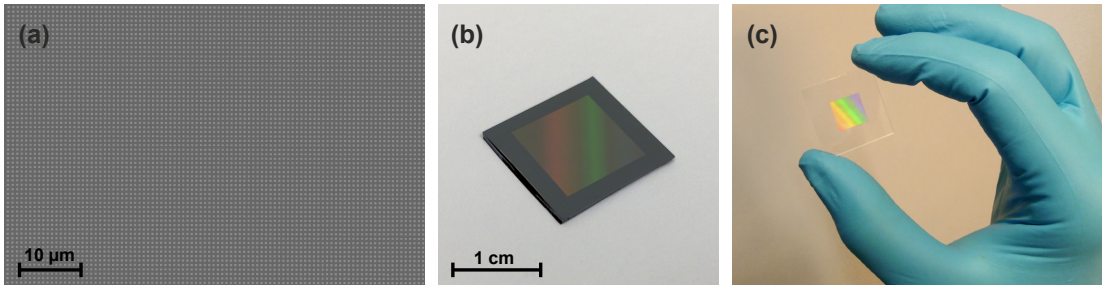

Figure 6.12: Large area nano-transfer print of 350 nm squares on a 1x1cm^2 area. (a) SEM image of part of the sample shown in b. (b) Photo of the full area nTP on a silicon substrate. (c) Photo of an nTP on a glass substrate. Reprinted from Nagel et al. [16]

A great advantage of the developed nTP process is its more or less easy scalability towards large areas. To demonstrate this, a stamp with 350 nm squares was used to transfer its structure over a comparably large area of 1x1cm^2. Figure 6.12 (a) shows a large area SEM image of the nTP on a scale, where single metal squares can still be distinguished. Characterized by SEM, the yield on the entire structured area was analyzed to be above 99.9%, where most of the imperfections were located almost exclusively near the edge of the patterned area. The complete transfer is shown in figure 6.12 (b). Here, firstly silicon with native oxide as the target substrate was used. One can clearly see that the transfer is homogeneous and defect-free also over larger scales. To demonstrate that the same process can be successfully applied to other substrate types, an nTP was carried out on a standard borosilicate glass microscope slide (figure 6.12 (c)). The response and reflection of light in the visible regime with the metal nanostructures indicate an effective transfer.

6.8.3 nTP for organic electronic devices

The nTP technology was also tested with organic electronics. Here, it is especially important to avoid any kind of chemicals on the organic device, which is given with nTP. In figure 6.13, an AFM image of 45 nm gold disks on a layer Poly(3-hexylthiophene)(P3HT) is given, which was part of an organic solar cell made by Morten Schmidt (TUM). The transfer worked perfectly over the entire patterned area of the stamp. It is important to mention that in this case, the sample was only heated to 50°C during the nTP as organic layers may degrade rapidly in an oxygen atmosphere and under high temperatures. However, the yield was as high as for nTPs performed on silicon surfaces at 200°C. The difference originates from the softer organic material, which has an intrinsically higher adhesion to

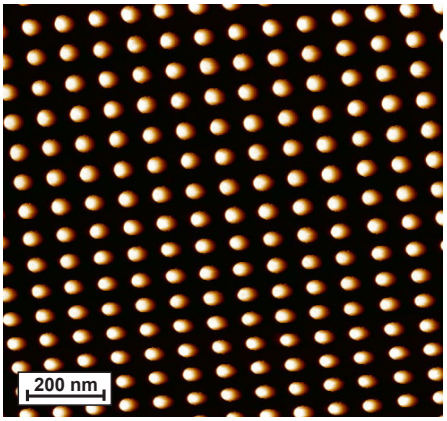

Figure 6.13: AFM image of a nano-transfer print of 45 nm gold disks on a P3HT layer of an organic solar cell. The height scale ranges from black: 0 nm to white: 23 nm.

gold and, in addition, perfectly adjusts to surface and grain roughness of the gold film, also resulting in higher adhesion forces. Polymer layers often have a low glass transition temperature, which can lead to interfacial fusion with the metal electrode[70]. As a result, only very low temperatures are needed for a successful transfer. Nano-patterned layers can also be used to fabricate transparent but highly conductive electrodes[71,72]. A thorough characterization of the organic solar cell and the effects of metal nanoparticles in intermediate layers of such a device can be found in the thesis of Morten Schmidt[73].

6.9 Summary

In this chapter, nano-transfer printing with replicated semi-flexible, hybrid polymer stamps down to 40 nm feature size was demonstrated. Typical problems regarding nTP, such as master reusability, defect tolerance, process cost, and speed, have been solved utilizing this replication technique. Working stamps based on OrmoStamp® material are flexible enough to ensure intimate contact with the underlying substrate over large areas, even in the presence of contaminating particles. Yet, the polymer is rigid enough for printing features in the sub-50 nm regime without lateral or roof collapse of the structures. Temperature and contact duration have been found to be the main process parameters influencing the yield of nTP on silicon substrates. It was found that at temperatures above 130°C, gold atoms will be mobile and get rearranged on the surface, thus minimizing release forces from the stamp. Using the optimized procedure presented in this work, a high yield above 99% has been achieved repeatedly.
Stamp and process-based contaminations on the substrate were found after nTP, which can be removed by a mild oxygen plasma post-clean (100 W for 1 min).

nTP works stable and reproducible, and there is evidence that nTP is only limited by the resolution of the stamp. The transfer quality can be tuned by varying temperature and printing duration. Although it is possible to reduce the applied temperature when using longer process durations, this is contrary to the advantage of a fast nTP process. However, this is a promising approach for temperature-sensitive substrates and, after all, faster and cheaper than conventional nanolithography techniques like e-beam lithography.

7 Photoelectrochemical reactivity of nanostructured electrodes for catalytic energy conversion applications

7.1 Theoretical background of heterogeneous electrocatalysis

In this section, a short overview of the most important electrochemical processes and mechanisms of heterogeneous catalysis is given. The (photo-)electrochemical experiments performed in this thesis are based on heterogeneous catalytic reactions on metal-supported semiconductors. Thus the theoretical background is limited to this particular case. Also, the focus will only be set on an electrochemical half-cell, the most well-known metal-electrolyte interface, which will be discussed in the following.

7.1.1 Electrode potential and electrochemical double layer

Any combination of two electrodes in an ion-conductive electrolyte is called a galvanic cell. On each electrode surface, an electrochemical half-cell reaction takes place, resulting in an electronically neutral overall reaction. Here, reactions are always connected to a charge transfer process. When electrons are emitted from the electrode, it is called the Cathode, and when electrons are collected (positive charge carriers emitted), it is called the Anode. When a molecule accepts an electron from the electrode, it is called a reduction reaction, otherwise, it is an oxidation reaction.

The Nernst-equation First, one of the fundamental equations in EC is the Nernst-equation. It relates the potential of an electrochemical reaction containing oxidized and reduced species to the standard electrode potential, temperature, and concentrations (or activities when not approximated to concentration coefficients) of the chemical species at equilibrium:

$$\Delta E = \Delta E_0 - \frac{RT}{nF} ln \frac{\prod c_{Ox}}{\prod c_{Red}} \tag{7.1}$$

where E_0 is the potential of a reference electrode, R the ideal gas constant, T the temperature, n the number of exchanged electrons in the reaction, F the Faraday constant, c_{Ox} and c_{Red} the concentration of the reduced and oxidized species.
In this thesis, EC measurements are either related to the Standard Hydrogen Electrode (SHE) or Reversible Hydrogen Electrode (RHE). The SHE consists of a platinum wire in a hydrogen purged acidic solution with an activity of $a_{H^+} = 1$. The difference of RHE compared to SHE is that the measured potential is not dependent on the pH-value and can be directly used in the electrolyte as it is corrected by the term: $-0.059V \cdot pH$ at room temperature.

The electrochemical double layer Close to the metal-electrolyte interface, the potential drop can be described by the Helmholtz model or double-layer model (figure 7.1). Ions in the solution are attracted by the applied potential at the electrodes. As the ions in the electrolyte are surrounded by polar water molecules, their nearest approach to the surface is restricted by this shell. Thus they form a packed layer close to the electrode. The potential drop in this Helmholtz plane is linear, while in the diffuse layer, the potential drops exponentially.

As a conclusion of this model, this layer system can be regarded as a parallel plate capacitor, where the final double layer capacitance can be calculated as a series of the Helmholtz capacitance and the diffusive layer capacitance. When changing the applied surface potential, a current will flow originating from charging or discharging of this capacitor.

7.1.2 Kinetics of metal/electrolyte reactions

The reaction rate and thus, the measured current is restricted by several parameters. It depends on the diffusion of reactants in the "bulk" electrolyte, on the chemical reactions themselves (which can consist of multiple intermediate steps), and on adsorption/desorption processes of reactants/products on the metal sur-

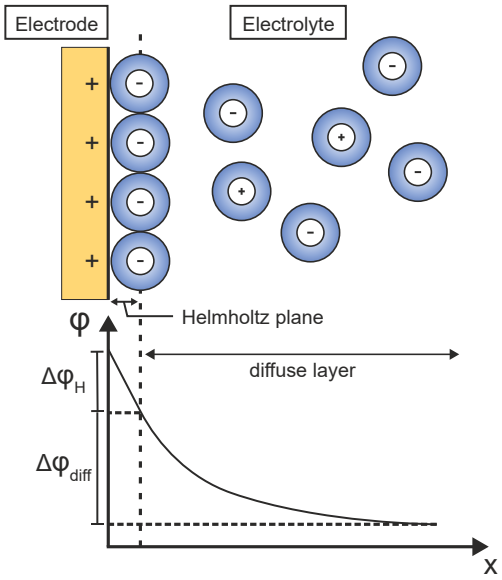

Figure 7.1: Schematic of the electrochemical double layer and the potential distribution at a metal-electrolyte interface. Depending on the applied voltage, the metal is positively (or negatively) charged. Thus anions (or cations) in the electrolyte solution are forced towards the interface. The potential φ drops linearly in the Helmholtz layer and exponentially in the diffuse layer.

face. The charge transfer characteristic can be described by the Butler-Volmer formulation as a function of the applied potential. The total current density j is a sum of the cathodic current density and the anodic one[74].

$$j = j_0 \cdot \left\{ exp\left[\frac{\alpha_o x \cdot n \cdot F}{R \cdot T} \cdot (E - E_{eq})\right] - exp\left[\frac{\alpha_r ed \cdot n \cdot F}{R \cdot T} \cdot (E - E_{eq})\right]\right\} \quad (7.2)$$

with j_0 the exchange current density (A/m^2), E the applied electrode potential, E_{eq} the potential at equilibrium (in the following, the potential difference is called the overpotential), n the number of exchanged electrons, F the Faraday constant, R the universal gas constant, T the temperature and α_{ox} and α_{red} the anodic and cathodic charge transfer coefficient.

The electrode current density is therefore exponentially dependent on the applied overpotential (see equation 7.2). This equation is valid in a well-stirred electrolyte for low current densities where the surface concentration is always equal to the bulk concentration of the reactants. Otherwise, the total current density is limited by different processes. First, the mass transport of the reactants from the bulk solution towards the interface can be a limiting factor. The mass transport typically consists of a diffusion part (caused by a concentration gradient), a migration part (caused by an electric potential gradient), and a convection part (the bulk motion of the fluid). The influence of the mass transport can be reduced by

choosing a highly concentrated electrolyte, by sufficiently stirring the solution, by performing short pulse measurements with a sufficiently long relaxation time between the pulses, or just by using low overpotentials.
Among other factors, the current itself can be limited by increasing resistance or by a limited amount of available charge carriers when a photoelectrode is being used, where a defined photoelectron generation is achieved by an incoming photon flux. In the latter case, the current density will saturate at high overpotentials due to this limitation.

7.1.3 The semiconductor/metal/electrolyte interface

When a metal comes in close contact with a semiconductor, it forms an electrical junction (metal-semiconductor junction (M-S)). It is one of the first semiconductor devices ever built. In contact, the junction can be non-rectifying, forming an ohmic contact, or rectifying by forming a Schottky barrier. The resulting behavior depends on the barrier height of the junction. To build a Schottky diode, the barrier has to be sufficiently larger compared to the thermal energy $k_B T$, which is roughly 25 mV at room temperature. In principle, the type of contact depends on the difference in the vacuum work function of the metal to the vacuum electron affinity of the semiconductor and the doping type of the semiconductor, as listed in table 7.1.

Table 7.1: Contact type of an MS junction.

Semiconductor doping	work function	contact type
p-type	$\chi_{SC}<W_M$	Ohmic contact
	$\chi_{SC}>W_M$	Schottky contact
n-type	$\chi_{SC}<W_M$	Schottky contact
	$\chi_{SC}>W_M$	Ohmic contact

In reality, this assumption of an ideal case often fails. In most cases, one gets current-voltage characteristics that don't follow the theory of an ideal Schottky diode. At the interface, a semiconductor often has a high density of surface states both on an open surface and at the interface with a metal. These states occupy a narrow band of energies, and the Fermi level always lies within this narrow band because it is hard to put enough charge carriers into the surface to fill (or empty) the band. This is called the "Fermi level pinning", which results in almost complete insensitivity to the metal's work function and leads to a barrier height of roughly half the bandgap height of the semiconductor. One solution to

this problem is to introduce an ultra-thin insulating layer, which can drastically reduce this effect[75].
Similarly, an ohmic contact is typically not achieved by just depositing a well-chosen metal on a semiconductor surface. Instead, an ohmic contact can be formed by growing a thin, highly doped semiconductor layer between the metal and the bulk semiconductor. By that, the space-charge region is so thin that it can be neglected as charge carriers are able to tunnel through this barrier (figure 7.2). A second approach is to perform a thermal annealing step after metal deposition so that the metal alloy with the semiconductor or to reduce the unintentional barrier at the interface. Because of the simplicity of the procedure, the annealing step was chosen in this work to fabricate ohmic backside contacts using aluminum both for n-type and p-type semiconductors.

When this MS system is placed in an electrolyte solution, the energy level has to align with the chemical energy level of the solution. The energy diagrams of the semiconductor photocatalysts, the metal, and the redox group in the solution are illustrated in figure 7.2 before and after contact. The Fermi level is close to the valence band for a p-type semiconductor and close to the conduction band for an n-type one. E_{CB} denotes the conduction band energy, E_{VB} the valence band, and E_f the Fermi level of the semiconductor photocatalyst. W is the work function of the metal and E_{redox}, the electrochemical potential of the redox group in the electrolyte. The scheme is drawn for an assumed case, where the work function of the metal is in between the Fermi level and the chemical potential of the electrolyte.

When they come into contact, the electrons and holes flow according to the potential differences and build up a new state, in which E_f , W, and E_{redox} are equilibrated. For gold (or other metal) nanostructures on a photon absorbing semiconductor in a photocatalytic system, the energy states are much fewer than those in the solution. As a result, E_f and W aline with E_{redox}, which itself does not change much. For p-type silicon (figure 7.2 (b)), the electric field in the space charge region actually helps to separate electrons and holes, that are generated by absorbed photons, and the photoelectrons are transferred to the metal catalyst where a chemical reaction is triggered at the interface to the electrolyte. Besides others, this is one advantage of using the catalyst metal to form a Schottky diode.

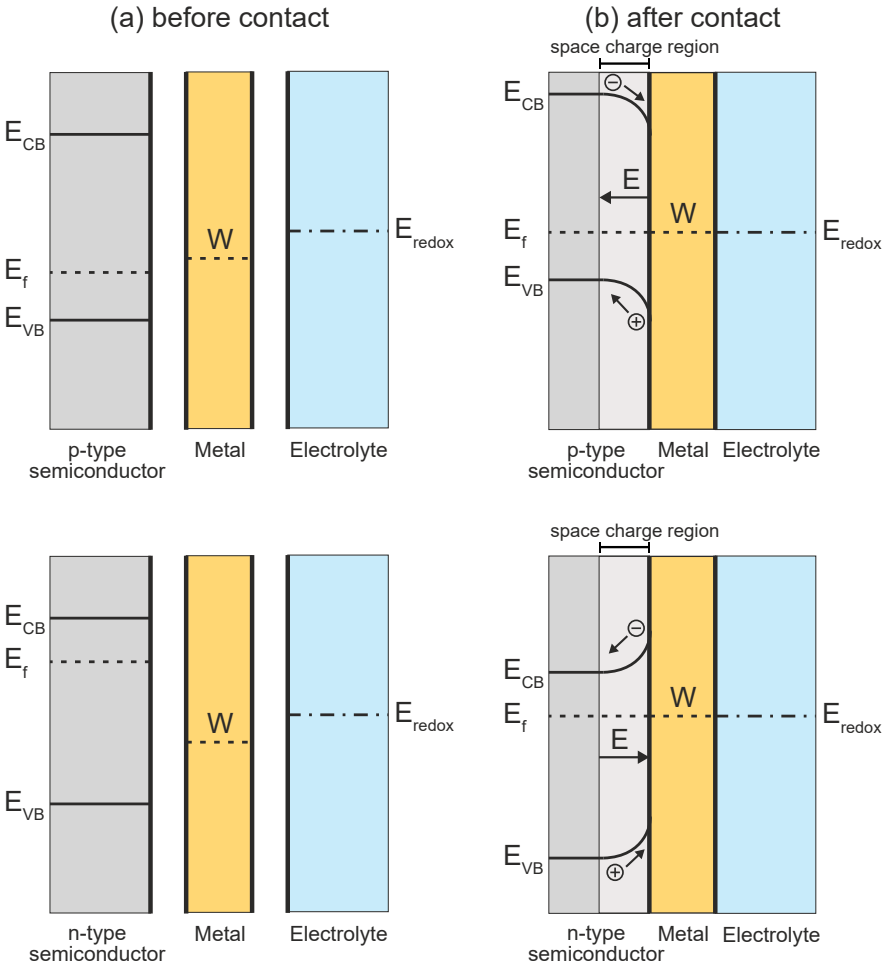

Figure 7.2: Energy diagrams of semiconductor/metal electrodes in different states. (a) before contact and (b) after contact both shown for n-type and p-type semiconductor photocatalysts. E_{CB} denotes the conduction band energy, E_{VB} the valence band, and E_f the Fermi level of the semiconductor photocatalyst. W is the work function of the metal and E_{redox}, the electrochemical potential of the redox group in the electrolyte. The scheme is drawn for an assumed case, where the work function of the metal is in between the Fermi level and the chemical potential of the electrolyte.

7.1.4 Hydrogen reactions and CO2 reduction mechanisms on catalytic surfaces

The hydrogen evolution reaction (HER) and the hydrogen oxidation reaction (HOR) have been intensely studied for many decades. At first glance, the hydrogen reaction seems to be a very simple one, explaining it to be present in many systems. However, as it takes place at the electrode surface it depends very much on the electrode material and the state of the surface, and it is, for that reason, still investigated intensively.

There are two different reaction pathways, while in acid media, the first step of hydrogen evolution is always the Volmer reaction. It is the electrochemical hy-

drogen adsorption H_{ad} on the electrode surface that includes the transfer of one electron:

$$\text{Volmer reaction: } H^+ + e^- \rightleftharpoons H_{ad} \tag{7.3}$$

For the second step, there are two possibilities:

$$\text{Tafel reaction: } H_{ad} + H_{ad} \rightleftharpoons H_2 \tag{7.4}$$

$$\text{Heyrovsky reaction: } H^+ + H_{ad} + e^- \rightleftharpoons H_2 \tag{7.5}$$

Thus, the formation of a hydrogen molecule is achieved by either recombination of two adsorbed hydrogen atoms (Volmer-Tafel) or a combination of an adsorbed hydrogen atom and one in solution with the use of one electron from the electrode (Volmer-Heyrovsky). The overall reaction is $2\,H^+ + 2\,e^- \rightleftharpoons H_2$.

Table 7.2: Half cell reactions and potentials vs. SHE.

Reaction	E_0[V]
$2\,H^+ + 2\,e^- \rightleftharpoons H_2(g)$	0.00
$O_2(g) + 4\,H^+(aq) + 4\,e^- \rightleftharpoons 2\,H_2O$	-1.23
$CO_2(g) + 2\,H^+(aq) + 2\,e^- \rightleftharpoons CO(g) + H_2O$	-0.11
$CO_2(g) + 8\,H^+(aq) + 8\,e^- \rightleftharpoons CH4(g) + 2\,H_2O$	0.17

The formation of carbon fuels (methane, ethanol, ...) and the base chemical ethylene by the chemical reduction of carbon dioxide is more complex than HER. It includes several intermediate steps, where the corresponding reaction pathways are still under research. A short sketch of the most important steps is shown in figure 7.3. Here, "RDS" denotes the rate-determining steps - the slowest intermediate step, which limits the overall reaction rate. The figure is based on the reaction pathways proposed by Kortlever et al.[76] In contrast to the HER, the reaction of CO_2 to CH_4 includes the transfer of 8 electrons from the catalyst metal to the molecule and intermediates.

7.1.5 Sabatier principle in chemical catalysis

The exchange current density of a single reaction is not constant for all electrode surfaces and materials. The strength of the adsorption and desorption step for a given set-up is typically not equal. Thus the overall reaction is limited by the slower process. The Sabatier principle states that optimal catalysis occurs when interactions between catalyst and substrate are of intermediary strength, neither

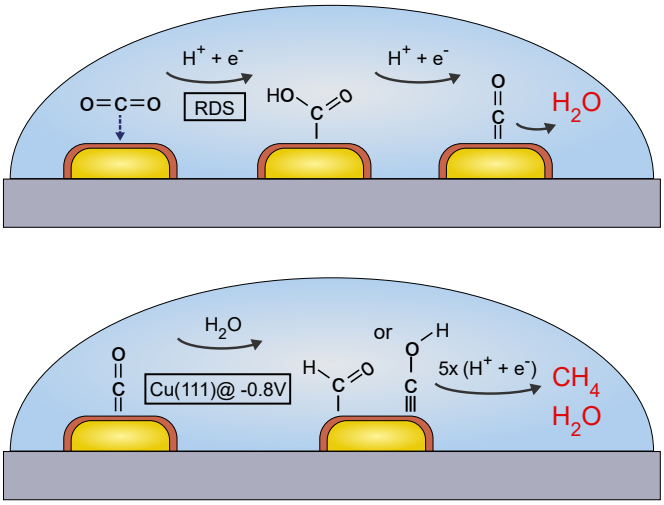

Figure 7.3: Possible reaction pathway for the electrocatalytic reduction of $CO_2 \longrightarrow CO$ on transition metals and intermediate steps to form methane CH_4 proposed by Kortlever et al.[76]

too strongly nor too weak[77]. This can be explained as follows: if the desorption rate is too high (adsorption rate low) for a used catalyst material, the surface concentration of adsorbed molecules is low, thus the probability of an ongoing reaction is low (e.g., in HER, two H_{ad} hydrogen atoms have to be in close contact to form an H_2 molecule(Tafel reaction)). On the other hand, if the adsorption is too strong, the energy required for a desorption step is high, thus the activity is low. The adsorbed molecules will shield the catalyst surface. The Volcano plot visualizes this principle by relating the exchange current density, which is proportional to reaction rate, to adsorption energy or bond strength. In figure 7.4, it is shown for the HER. The Sabatier principle illustrates the dominant role of platinum as a catalyst for HER. It is close to the optimum, where $\Delta G \approx 0$ and the rate passes through a maximum.

7.1.6 Carbon-dioxide reduction on copper surfaces

For the conversion of CO_2 to carbon fuels, copper as catalyst material shows a reasonable selectivity. Hori et al. investigated different materials for the electrochemical reduction of CO_2[79], some of which are listed in table 7.3. It is clearly visible how the resulting products depend on the used catalytic material. Platinum, as an example, has a high-efficiency hydrogen production rate, with a comparably low needed potential. However, it cannot be used for carbon-dioxide reduction. Copper, on the other hand, has one of the highest faradaic efficiencies for reducing CO_2 to methane. However, the selectivity is not very high, as ethylene is almost equally produced. This selectivity also depends on other parameters that

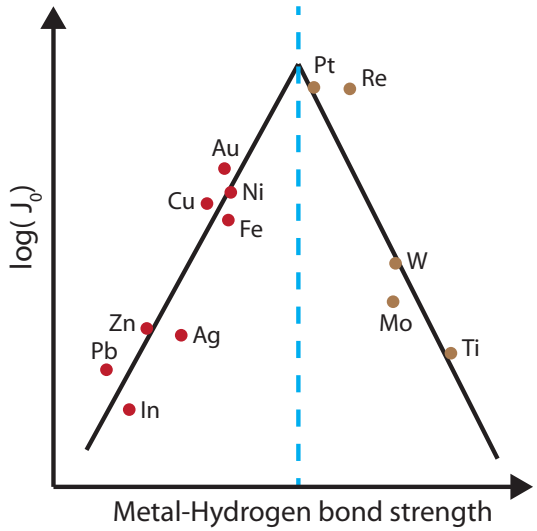

Figure 7.4: Scheme of a Volcano plot for hydrogen adsorption in acid solutions. Reaction intermediates, such as adsorbed hydrogen atoms in the HER, should neither bind too strongly nor too weak on the electrode surface in order to achieve a high activity. Reproduced from Quaino et al.[78]

can be used to improve it. First, the used overpotential can drastically change the activity and selectivity. Hori et al. demonstrated how the selectivity towards methane rises with increasing overpotential while the hydrogen faradaic efficiency decreases. However, this means that the conversion process itself is no longer efficient.

The pH value of the electrolyte has a direct influence on the reaction pathways and, therefore, on the product selectivity. It is assumed that the pH affects reaction intermediates differently[76]. As a result of this finding, product analysis experiments were typically performed in pH buffered solutions.

The preference of single reaction pathways and catalytic activities can also depend on geometric properties of the electrode material, such as surface roughness and cluster size and shape. This approach will be examined in more detail later in this chapter.

Table 7.3: Faradaic efficiencies of various products from the electrochemical reduction of CO_2 on different catalytic materials using a current density of $5 mA/cm^2$. Taken from Hori et al.[79]

Electrode	Potential vs NHE [V]	Faradaic efficiency [%]			
		H_2	CO	CH_4	C_2H_4
Au	-1.14	10.2	87.1	0.0	0.0
Pt	-1.07	95.7	0.0	0.0	0.0
Cu	-1.44	20.5	1.3	33.3	25.5
Pd	-1.20	26.2	28.3	2.9	0.0
Ti	-1.60	99.7	0.0	0.0	0.0

7.2 Stability of nanostructured resist on gold surfaces for electrochemical experiments

Nanostructured electrodes can be used to increase the efficiency of chemical reaction rates[80,81], to alter the selectivity of reaction pathways[79,82,83] or to investigate fundamental processes on the nanoscale. The latter was performed to investigate the spill-over effect of adsorbed hydrogen atoms from a platinum catalyst material towards a gold substrate. A deeper look into the performed experiments and results can be found in the work of Cornelia Ostermayr[84]. The basis of these experiments is the stability of the nanostructures against aggressive acids and especially their long-term stability. This has been investigated in the following.

7.2.1 Experimental set-up and materials

The experiments were carried out in an electrochemical cell with a three-electrode configuration (section 3.6). An Autolab potentiostat (PGStat30N, Metrohm, Germany) was used for potential or current control. All glassware was cleaned in Caro's acid and thoroughly washed with distilled water. A gold wire (99.99% purity) was used as a counter electrode. A mercury sulfate electrode (MSE) was used as a reference electrode and a 1M perchloric acid ($HClO_4$) solution as the electrolyte. The shown CVs are plotted against SHE rather than MSE thus, they are shifted by $E_{MSE(1M)} = 0.675 Vvs.SHE$.

7.2.2 Sample preparation

The working electrodes consisted of a 250±50 nm thick Au layer with a 2.5±1.5 nm chromium layer as an adhesion promoter on a borosilicate glass (Arrandee, Germany). They were cleaned with isopropanol and acetone and rinsed with DI water. For gold surface measurement calibrations, the sample was covered in a spin-coating process with a 1.6 μm thick layer of photolithography resist AZ5214E and structured with a 2x2 mm^2 square opening as described in section 3.1.1.
For nanostructured samples, the gold substrates are covered with imprint polymer (mrI-8020R): Typically, a 1:1.35 solution is used and spin coated with 3000 rpm for 30 s. Depending on the stamp geometry, these parameters were varied slightly to minimize the residual layer thickness. Then, the polymer layer is soft-baked at 100°C for 1 min. A line stamp with line widths between 50-500 nm is used for nanostructuring, where the inter distances of the lines are always equal to their width. The imprint is performed under standard conditions (described in

the previous chapters) to reach 165°C at 30 bars for 3 min. After cooling down, the stamp is then lifted from the substrate, and the residual layer is removed with oxygen plasma in a dry-etching process. Here, it was taken care to minimize over-etching, in order to obtain a maximum and always even thick final layer. A small area of resist on one side of the sample is then stripped with a q-tip and acetone, and a gold wire is placed on the opened gold surface which is connected to the potentiostat. Both the sample and the connecting wire are then covered with Teflon tape (CMC Klebetechnik) while the structured areas of the resist (and thus the gold surface) were left open. Some samples showed a peel off of the Teflon tape close to the structured areas of the resist for long-run measurements. As a consequence, the edges of the hole punched Teflon tape were additionally protected using a chemically inert 2-K epoxy glue. An image of such a sample can be found in figure 7.5.

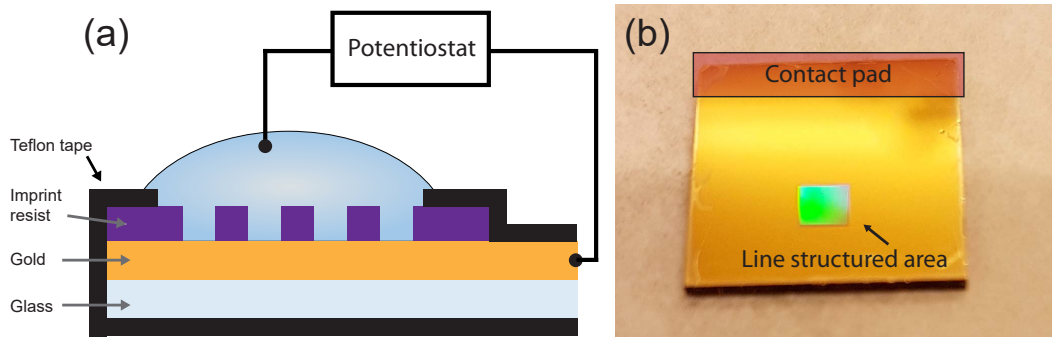

Figure 7.5: Nanostructured electrode sample on a gold substrate. (a) Sketch of the sample layout. Only the patterned area has contact with the electrolyte. (b) The image was taken before covering with Teflon tape.

7.2.3 Electrochemical characterization measurements

The sample was immersed in the electrolyte (1M perchloric acid), and the cell was purged with argon (purity 4.8, Linde, Germany) for 1 hour until all oxygen was removed. Each sample was then cycled several times between -0.08 V and 0.92 V vs. SHE until a stable voltammogram was obtained. This procedure removes contaminations from the gold surface and additionally brings the surface to a defined state, which may have been altered during oxygen plasma treatment to remove the residual layer of the imprint resist.

In figure 7.6, an example of such a measurement is given for an optical lithographically defined sample for a gold surface area calibration. Two prominent

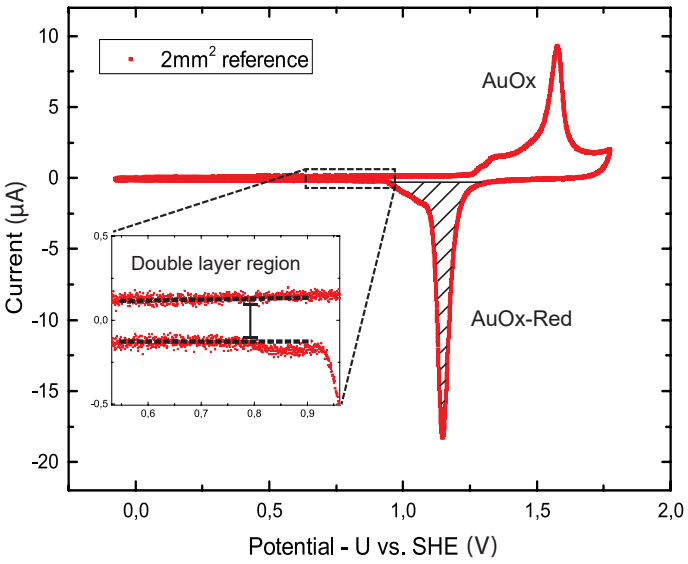

Figure 7.6: Cyclic voltammogram of an optical lithography defined reference sample. There are two prominent peaks for the gold oxidation charge(AuOx) in positive scan direction and one for the gold-oxide reduction charge (AuOx Red). The CV is overlayed with a small and constant double layer (de-)charging current.

peaks are visible. For positive currents and potentials, a current is measured due to a gold oxidation charge transfer. Au oxidation starts at around 1.2V vs. SHE. The oxidation regime exhibits one or more peaks, depending on the properties of the surface, such as crystal orientation. If the potential is increased to higher values, as shown in the figure, oxygen evolution starts to dominate. By integrating this AuOx Peak, the gold surface area can be determined, however, the peak has to be double-layer corrected, in any case. This constant current originates from the charging of the double-layer capacitance (section 7.1), which depends on the scan rate and the surface area.

AuOx reduction can also be used to determine the Au surface area, which is the reversed action as the AuOx process. As this takes place at lower potentials, it is less likely that the current is overlayed by ongoing oxygen evolution reactions (OER). However, the extracted total charge of the reduction peaks also depends on the maximum applied potential during AuOx. Thus, the maximum potential was kept fixed for the calibration and all further measurements.

7.2.4 Stability and usability of imprint polymer as a mask to form nanostructured electrodes

The direct use of imprint polymer as a stable mask to form nanostructured electrodes was tested. The samples are prepared as described above.

First, the open gold surface area was determined through AuOx and AuOx-red peak-integration of taken CVs for Line-structured patterns between 50-500 nm line widths (filling factor 50%) on a 2x2 mm^2 area. This leads to an open gold surface area of 2 mm^2. The determined charge transfer can be converted to an area with the relation $q = 600\mu C/cm^2$, also found in literature[84]. For the calibration sample with a defined opened area of 2 mm^2 (optical lithography) an AuOx charge of 11.33μC and an AuOx-red charge of -12.28μC was measured. This corresponds to a determined area of 1.89 mm^2 and 2.05 mm^2, respectively. Here, the integration of the AuOx peak had a high error, due to the reasons mentioned above. The AuOx-red calibration leads to a conversion value of $q = 614\mu C/cm^2$ being close to the literature one.
Measurements with structured electrodes using the imprinted resist mask showed very stable and similar results for the 100 nm - 500 nm lines. The 500 nm lines had an average AuOx charge of 12.21μC corresponding to a gold surface area of 1.99 mm^2 (using the calibrated conversion factor) and an AuOx-red charge of -12.38μC with a calculated area of 2.02 mm^2. This measurement was repeated after being immersed continuously in 1M $HClO_4$ for 6 hours while performing several measurement cycles. No change was observed. Additionally, the same tests were done in 1M H_2SO_4, proving the same effectiveness of the mask.
The stability was as well checked with SEM images. In figure 7.7, such an image after a long term EC-measurement is presented. Although using only 100 nm wide lines, the mask does not show any form of degradation.

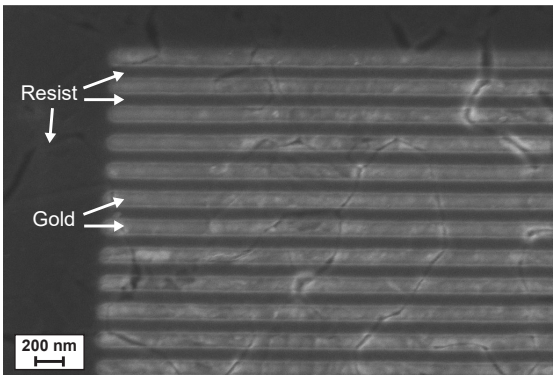

Figure 7.7: SEM image of an imprint resist mask with 100 nm lines and 100 nm inter distance on a gold substrate after being immersed in 1M $HClO_4$ for over 6 hours. The dark areas are covered with resist. The nanostructures do not show any form of degradation after multiple measurement cycles.

However, for the smallest feature sizes of 40 nm line width, the determined gold surface area was larger than the expected value of 2 mm^2. As the structures

themself remained unaffected, the layer thickness of the resist could be the cause of this finding. The stamps used for fabricating these samples have a smaller structure height compared to stamps with 100 nm line width and above due to fabrication problems. As a result, the resist thickness in the non-patterned areas is thinner. SEM images revealed small holes in the closed resist films. It is believed that these holes are formed by a de-wetting effect, as the adhesion to gold is typically very low. As the resist gets thinner, the cohesion of the film gets weaker, leading to the formation of more and more of those holes. This increases the unintentionally exposed gold surface, causing a leakage current. Figure 7.8 shows the CVs of closed films with varying thicknesses of imprint resist and a CV of a reference sample (orange) as a comparison. The leakage current is small compared to the reference. However, it cannot be neglected at some point. The inset of figure 7.8 (a) clearly shows the decrease of leakage current with increasing resist thickness. The evaluated open gold surface areas are shown in Figure 7.8 (b). They are related to the total area of the same sample area. The part of the current, which originates from these defects, increases exponentially with decreasing layer thickness. This has to be kept in mind when designing experiments with directly patterned nanoelectrodes. For standard imprint conditions used in this thesis, the final resist layer is 100 nm and above. Thus the leakage current percentage is small with a value of around 0.1%.
It has to be noted, that this small percentage still can lead to a high error in the measurement, as the imprinted area typically is considerably smaller than the remaining areas of the sample (figure 7.5 (b)). This means, that the area covered by a resist layer can contribute to the total current by a much higher percentage. This finding has been taken care of by sealing the whole sample in Teflon tape, while only the patterned area of the sample is opened up using a small hole punch in the Teflon tape (figure 7.5). When taking care while positioning this tape, the area of the sample with contact to the electrolyte is minimal, and the leakage current can be neglected.

This method of sample fabrication for electrochemical applications is very fast and easy. It has limited process steps. Thus, the risk for contamination is small. It can be used for experiments, where nanostructured electrodes may lead to new physical effects, or to separate and analyze effects which are close to the measurement noise. It has been used in collaboration with the group of Prof. Stimming for research on the topic of hydrogen spill-over effect, studied by Cornelia Ostermayr[84].

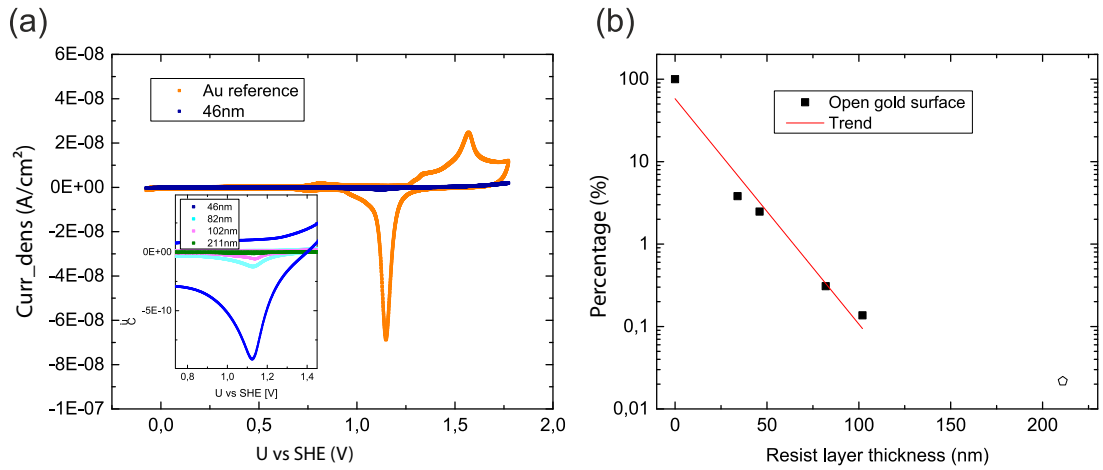

Figure 7.8: (a) Cyclic voltammogram of a gold reference sample defined by optical lithography compared to measurements with closed imprint resist layers with varying thicknesses. For very thin layers, a small gold signal in the CV is present, giving rise to a leakage current. (b) Percentage of measured exposed gold surface with respect to the total area. With thinner layers, the leakage current increases exponentially.

7.3 FEM simulations of light-matter interaction at nanostructured metal electrodes

The response of nanostructured metal arrays on top of a semiconductor substrate to an electric field is examined using a Finite-Element-Method (FEM) simulation model. This model helps to interpret experimental data in the following sections and is additionally useful to optimize structure shape and dimensions towards high E-field enhancements to drive chemical surface reactions efficiently. In this section, the FEM model is presented, and simple design rules of the nanoelectrodes are given.

7.3.1 Localized Surface Plasmon Resonance

A prominent phenomenon when light interacts with metal nanoparticles is the Localized Surface Plasmon Resonance (LSPR). It is the collective excitation and oscillation of electrons of a conduction band in metal in phase with the varying electric field of the incident light (figure 7.9).

As a result, the nanoparticles exhibit enhanced near-field amplitude at the resonance wavelength. This field is highly localized at the nanoparticle surface, making it an ideal effect to be utilized in heterogeneous catalysis. In contrast to SPR, the E-filed decays rapidly away from the nanoparticle into the substrate background. On the one hand, this means that far-field scattering by the particle

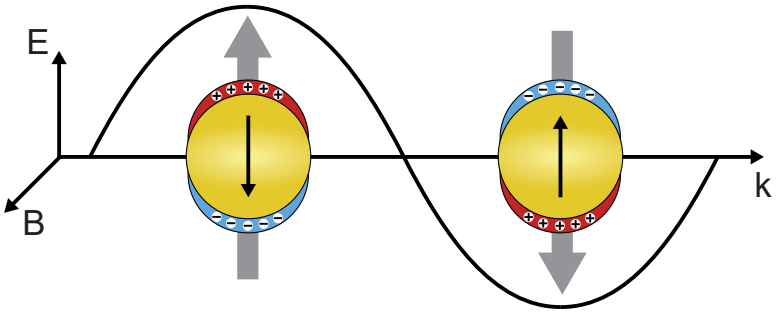

Figure 7.9: Sketch of Localized Surface Plasmon Resonance. An incident E-field can excite collective electron oscillations. A strong near-field amplitude enhancement is observed at the resonance frequency.

is also enhanced by the resonance and on the other hand it is not necessary to have a complicated optical set-up to couple in light for LSPR.
The restoring force of the separated charges depends on the size of the particle, and as a consequence also the resonance frequency is size-dependent. Despite that, also other parameters are heavily influencing LSPR, such as shape, structure, and material of the metal particle but also the surrounding medium. Changes will lead to a strong shift, which can be used to characterize samples and interfacial properties.

7.3.2 FEM model using Comsol Multiphysics

Simulations have been carried out using Comsol Multiphysics. For modeling LSPR, the RF-module has been used to simulate electromagnetic waves in the frequency domain. A sketch of the domain layout can be found in figure 7.10 (a). It mainly consists of three parts (with additional sub-layers): the metal electrode in the center of the model, the substrate in the lower part, and the environment on top. The top boundary surface is chosen as a port for wave excitation with a linearly polarized EM-Wave traveling in the z-direction and only having an E_0 amplitude value in the x-direction. The lower boundary surface is defined as an outgoing port calculating S-parameters, which are the elements of a scattering matrix necessary to extract reflectance and transmittance percentages. The substrate and environment domains have to be rather large in height as at least a full wavelength must fit inside these boxes. Since also resonance frequencies in the near-infrared regime were calculated in this section, these domains then have to be some micrometers in height. In figure 7.10 (a), the electric field of an incoming wave is additionally visualized.
Opposing sidewalls are defined as periodic boundary conditions using Floquet periodicity[85]. This way, the model represents an infinite array of nanoparticles

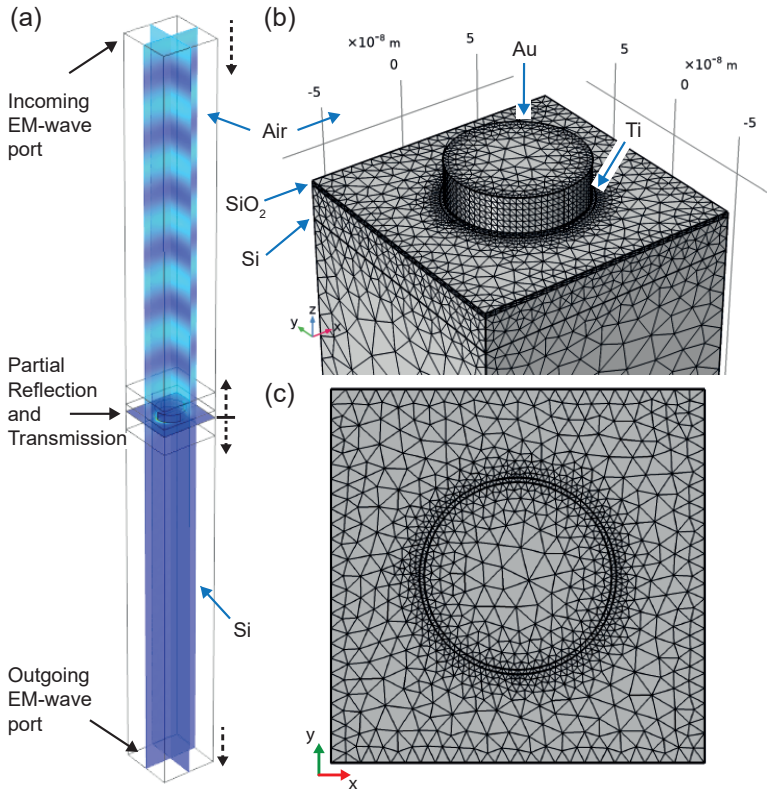

Figure 7.10: FEM model of light-matter interaction at nanostructured metal electrodes on a substrate (here mostly silicon). (a) Full domain elements of the model with three 2d slices of the electric field distribution (x-y, x-z, and y-z plane). (b)+(c) Mesh elements of the domains. The mesh is gradually refined towards the structure edges. An extra fine grid is added at the metal surface.

both in x and y direction, while minimizing needed mesh elements and computation time. The electric displacement field model was used for all domains using the relative permittivity values ϵ_r from the corresponding material. An additional thin native oxide layer on top of the substrate and a titanium adhesion promoter between substrate and gold nanostructure have been included for the final model.

The real- and imaginary parts of the relative permittivity are based on literature values. The values for gold and titanium were taken from Johnson and Christy[47], values for silicon from Green et al.[45], and silicon-oxide from Gao et al. and Rodriguez-de Marco et al.[86,87].

The meshing type has to be controlled individually for each domain, however, changes in shape and dimensions are still automatically adjusted. First, an additional domain is added being 2 nm larger than the metal domain and defined as "air" (or the used environment material) just to force a refined mesh-element increase in the immediate vicinity of the metal, where changes in E-field are strongest (figure 7.10(c)). A normal tetrahedral mesh would lead to problems

for large but very thin domains, such as the native oxide layer or the titanium adhesion layer. Therefore, the top surface of the metal is covered with a free triangular 2D mesh, while a curvature factor of ≈0.08 is included in order to obtain a high-density mesh at the edges and a lower dense one in the center. This mesh is copied in multiple symmetric layers within the metal domain using a "Swept mesh". Typically, one layer every 3 nm height was used for the plasmonically active material and one layer every 1 nm for the very thin titanium adhesion layer (figure 7.10(b)). The same method is applied to the native oxide layer, where at least two mesh layers are used. After that, all elements are converted to tetrahedral ones.

Opposing sidewall boundaries are also first meshed with a 2D triangular method, where only one side was meshed first, which is then copied to the opposing side. This has been done to respect the floquet boundary conditions mentioned above, where the E-field must be identical and symmetrical at every single point of opposing sides and can cause trouble if the meshes are not identical. All remaining volumes are then filled with a free tetrahedral mesh, where the element size gradually increases when further away from the metal nanostructure in order to optimize the total element count.

This total count does depend strongly on the nanostructure size and thus on the total model volume. For a 75 nm disk with 150 nm pitch, typically 130k elements are generated.

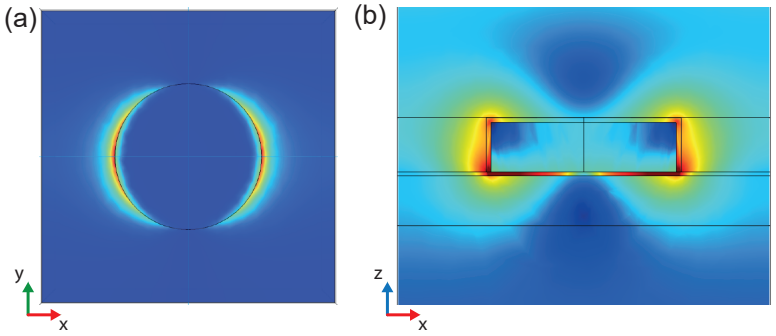

Figure 7.11: E-field distribution extracted of a FEM Simulation of a 75 nm disk (18 nm Au/2 nm Ti) on top of a silicon substrate with a 1.5 nm thin SiO_2 layer in air. (a) normalized E-Field in **linear scale** on top of the SiO_2 surface (x-y plane). (a) normalized E-Field in a **logarithmic scale** of the side-view of the metal antenna (x-z plane).

Figure 7.11 shows the E-field distribution of a simulated 75 nm gold disk on a silicon substrate with a 1.5 nm thin SiO_2 layer in air. Subfigure (a) shows a top-view (x-y plane) of the disk on a linear scale. The increased electric field at the edges in the direction of the incoming E-field of the light is clearly visible. This "antenna effect" is more prominent in subfigure (b) where a side-view of the

z-x plane is shown with a logarithmic scaling of the electric field. The strongest E-field enhancement is reached at the top and bottom edges of the particle and especially at the metal-SiO_2 interface.

7.3.3 Influence of design parameters on LSPR

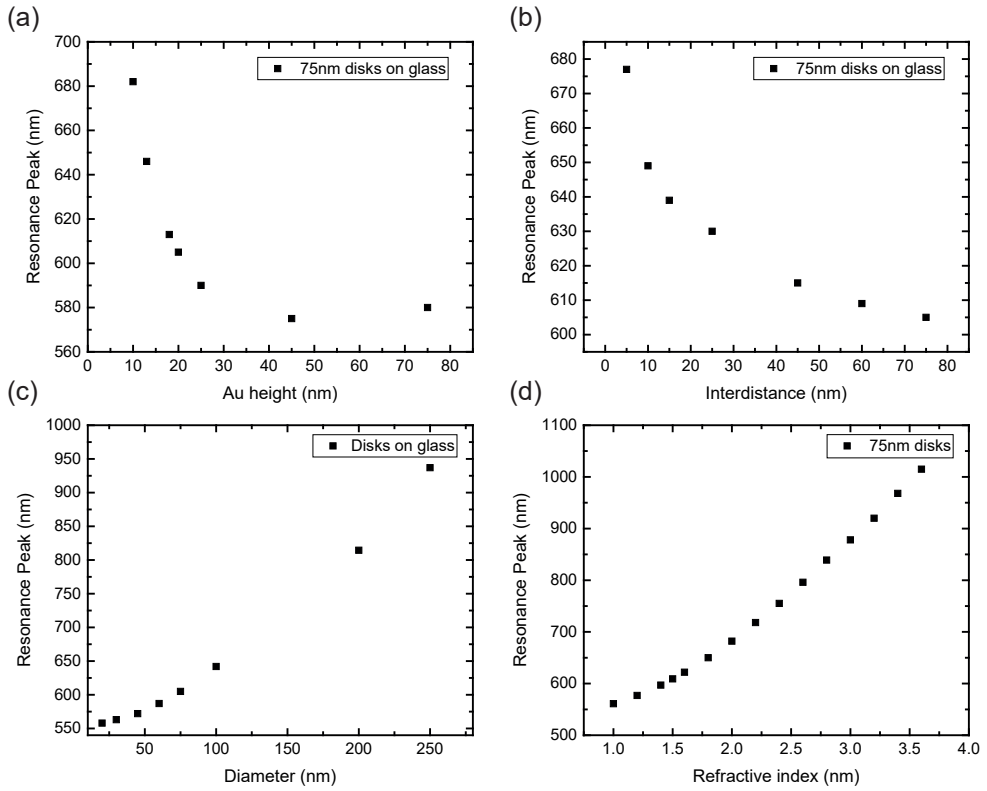

Figure 7.12: Reflection Peak positions of FEM simulated LSPR of gold nanodisk arrays on a glass substrate with following standard parameters (if not varied): 75 nm diameter, 150 nm pitch, 20 nm gold height (n=1.465). Results are shown for varying (a) disk height, (b) inter distance of individual disks (shrinking pitch), (c) disk diameter (while keeping pitch:diameter=2:1), (d) substrate refractive indexes.

In figure 7.12, the LSPR shift for changing design parameters is given, which were simulated using the FEM model. Transmittance, reflectance, and absorbance of the nanostructure were calculated using the S-parameters for all simulated wavelengths of the incoming light, and the maximum (or minimum) of the peaks were extracted. Here, 75 nm gold disks with 20 nm height are being shown as standard parameters. The substrate was initially chosen to be glass, as it is transparent in the LSPR range. Thus it is possible to measure both reflectance and transmittance experimentally. The general dependencies of the results also apply to other substrate materials, although they then scale differently.

It is clearly evident, that the resonance frequency strongly shifts with various parameters. The LSPR drops from around 680 nm to 575 nm for gold thicknesses of 10 nm and 45 nm, respectively. It then saturates at this level or even slightly increases when the thickness reaches the disk diameter (figure 7.12(a)). When the distance between the nanostructures is reduced, the resonance gets red-shifted (figure 7.12(b)). However, this effect only becomes relevant when distances are below 10 nm.

The greatest changes can be achieved by increasing the feature sizes or by changing the substrate material (figure 7.12 (c)+(d)). Although this is also true for the environment (the upper domain of the model), a change from an air (n=1) to a water-based electrolyte (n=1.33 in the visible range) would not change the frequency too much.

With the nanopatterning process presented in this thesis, LSPR starting from 550 nm up to the near-infrared region can be achieved on glass substrates. The resonance is strongly red-shifted with larger structure dimensions. Additionally, it is strongly red-shifted with increasing refractive index of the substrate. This is why the LSPR is mainly found in the red to the infrared region on silicon substrates.

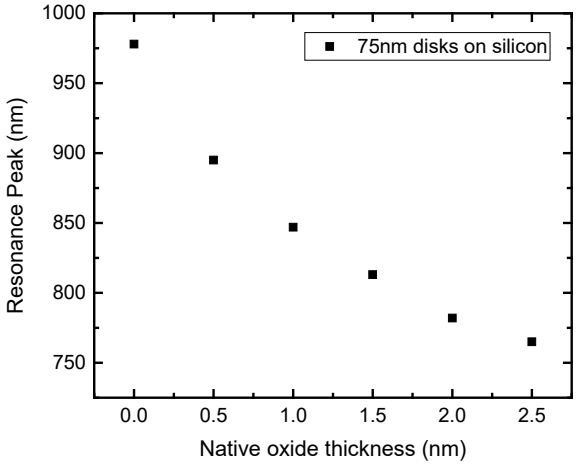

Figure 7.13: Reflection Peak positions of FEM simulated LSPR of 75 nm gold nanodisks (20 nm height) on a silicon substrate for varying native silicon oxide thicknesses.

Although the strong dependency on the substrate type has been shown, it is still interesting to see how small local changes of this parameter close to the metal antenna can affect the resonance. For this reason, a simulation has been performed, implementing a thin native oxide layer on top of a silicon substrate (below the metal nanostructure). The dependency is shown in figure 7.13. Even with a minimal oxide layer (changing the refractive index to SiO_2 n=1.46 at

900 nm wavelength[87]) the LSPR drops drastically from a value of around 980 nm without an oxide layer, to 810 nm for a layer thickness of 1.5 nm, which is a typical value for silicon under ambient conditions. This shows that LSPR is extremely sensitive to changes in even only the surroundings of the metal antenna. This sensitivity is in the same range as the E-field enhancement shown in figure 7.11 and is a further reason why LSPR is important for sensing applications.

7.4 Comparison of nanotransfer printing and lift-off nanoimprint lithography for electrochemical applications

7.4.1 Introduction

In this section, the applicability of nTP and LO-NIL for the structuring of low-cost, large-area photoelectrodes is presented, with special emphasis on the difference between the electrochemical properties of nanostructures produced by both methods. The interfaces are characterized by the use of plasmonic resonance effects of the nanostructures when illuminated with light in a well-chosen spectral range. This does shed more light on the role of the metal-semiconductor interface, and additionally, this is a proof-of-principle for plasmonic photoelectrochemical solar cells, potentially enabling higher efficiencies and product selectivity. Photoelectrochemical measurements will be presented and discussed considering the results of electrical measurements respecting the interfacial properties (section 6.4).
The beneficial effects of surface plasmon resonances on photoelectrochemistry have already been proven in literature[88,89]. It is possible to transfer the results to a copper system, which has been shown to yield a rich product spectrum containing methane and ethylene[82] (see also table 7.3).

In this section, arrays of gold nanodisks and nanosquares supported on p-type silicon (p-Si) are studied, which are a promising system for the photoelectrochemical reduction of carbon dioxide (CO_2)[7,83]. In figure 7.14, a layout of the sample design is given. Gold as an electrode material is chosen for several reasons:

1. Because of its stability in air
2. Because of the well-known plasmonic response under illumination in the visible spectrum

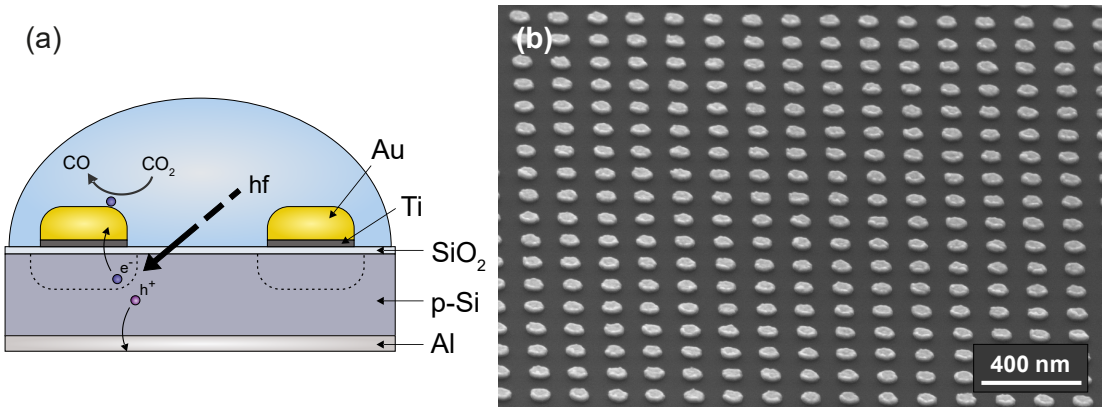

Figure 7.14: Sketch of the sample design used in this section. Ti/Au metal nanoelectrodes are fabricated with nTP and LO-NIL on a p-type silicon substrate with a thin SiO_2 layer. The back contact consists of aluminum, while the sample is illuminated from the top through the electrolyte. (b) SEM image of a slightly tilted sample surface, decorated with disks of 75 nm diameter and 150 nm inter distance.

3. It has the advantage of not having to change the developed and well-characterized manufacturing process described in the previous chapters (Although evaporating a different kind of metal isn't a problem)

4. Additionally, it is a promising catalyst for the electrochemical reduction of CO_2 since it yields the product carbon monoxide (CO) with high selectivity and a comparatively simple electrochemistry [82].

Parts of the following experiments have already been published, and sections are taken from these publications [13,90].

7.4.2 Substrate preparation

P-type silicon (CZ(111) ±0.5, 5-25 Ωcm, Boron doping: $5 \cdot 10^{15} - 4 \cdot 10^{16} cm^{-3}$, Si-Mat, Germany) is used as a substrate. The backside of the semiconductor is prepared with an aluminum (Al) back contact. Here, in a first step, the natural oxide is removed by a buffered oxide etch (BOE), a 6:1 mixture of 40% NH4F and 50% HF solution. Then, a 200 nm thick Al layer is deposited onto the etched surface via PVD and subsequently annealed at a temperature of 400°C for 30 min in a nitrogen atmosphere. The front side is oxidized in an oxygen plasma for 5 min, to remove all organic contaminations and also to grow a thin oxide film if a natural oxide is not already present on the silicon wafer. It has to be stated, that plasma growth of silicon-oxide using a Barrel etcher (see section 3.3) is rather limited and typically stops at only 1-1.5 nm thickness. This oxide layer is etched in a BOE solution until the plasma-grown oxide is completely removed, indicated by a clearly visible change to a hydrophobic surface. This is done

to remove metallic surface contaminations, which can not be removed with an oxygen plasma treatment. Depending on the experiment, the surface is then oxidized again. The clean surface is covered with a layer of photoresist (spin-coated) to protect it from cleavage dust. The wafer is cleaved into 11.5x11.5 mm^2 pieces and cleaned with acetone, isopropanol, and deionized water.

7.4.3 Nanopatterning procedures

Nanotransfer printing

The samples are prepared, as developed in chapter 6. In short, the following production steps are carried out:

1. A gold/titanium metal layer is deposited on the ready-to-use stamp in a high-vacuum physical vapor deposition (HV-PVD) system (Leybold L560, Germany) at an evaporation pressure of $6 \cdot 10^{-8}$ mbar. First, an 18 nm gold layer is evaporated at a rate of 3 Å/s followed by a 3 nm thin titanium layer evaporated at a rate of 1 Å/s.

2. Right after metal evaporation (but before taking the stamps out of vacuum conditions), the target substrate is cleaned (acetone/isopropanol) and pre-conditioned in an oxygen plasma (600 W, 2 min, 100 sccm, 100 Pa). Then, the exposed titanium surface on the stamp is activated with a mild oxygen plasma (100 W, 1 min, 90 sccm, 100 Pa).

3. The stamp is placed on the target substrate and put into an imprint machine (Obducat imprinter 2.5, Sweden).

4. A uniform pressure of 3 MPa is applied via compressed nitrogen for 3 min at a raised temperature of 200°C

5. While still hot, the stamp is lifted from the substrate.

Lift-off Nanoimprint lithography

The samples are prepared, as developed in chapter 5.

1. The lift-off resist (PMGI SF6) is diluted in a ratio of 1:4 for small feature sizes, then spin-coated on the wafer at 4000 rpm for 45 s. The resulting layer is soft-baked at 255°C for 3 min which gives a thickness of ≈30 nm. The LOR thickness was increased by using thicker metal layers. Then, a layer

of imprint resist (1:1.35 dilution) is directly spin-coated on top of the LOR at a spinning speed of 3000 rpm for 30 s. It is soft-baked at 100°C for 1 min, resulting in a layer thickness of ≈77 nm.

2. It is then patterned in a thermal imprint process at a temperature of 165°C and a pressure of 30 bars for 3 min. The sample is cooled down to 90°C and the stamp is demolded from the substrate using a sharp razor blade.

3. The residual layer is removed using anisotropic reactive ion etching (RIE) (PlasmaLab 80 Plus, Oxford Instruments, UK). A passivating RIE process with a gas mixture of O_2 (27 sccm) and C_4F_8 (25 sccm) is used at a plasma rf-power of 200 W as a highly anisotropic etching step and thus high shape retention. A short oxygen plasma etching step (5s) is performed to remove the fluorinated inhibition layer (section 5.4.4) Pure oxygen plasma etching (O_2 (25 sccm) at a plasma rf power of 35 W) is used for feature diameter adjustment.

4. In case of the existence of an aluminum back-contact, it is covered by a piece of wafer tape (Icros SB-085L-BN20-R2, Mitsui chemicals, Japan) as Al is etched by the developer solution.

5. The under etching of the imprint resist is performed in an isotropic wet-chemical developing step using a buffered potassium hydroxide (KOH) based developer (AZ400 K, Microchemicals, Germany) in a 1:5 dilution followed by thorough rinsing with deionized water. The lateral etching of the LOR is the most critical step. The development time varied between 17-25 s, depending on the individually measured LOR thickness. The complete removal of the LOR in the openings is indicated by a strong contrast change of the patterned area. In most cases, this visual change was the better way to define the etching time.

6. The target metal stack is evaporated using the same parameters and conditions as for the nTP process. Only the layer order is inverted as it is now directly evaporated on the substrate.

7. Lift-off is carried out in N-Methyl-2-pyrrolidon (NMP) (Merck, Germany) at a temperature of 50°C inside an ultrasonic bath until the LOR and imprint resist is completely removed and only the patterned metal nanostructures remained on the substrate.

7.4.4 Photoelectrochemical measurements

Electrochemical measurements in these sections were performed by the group of Prof. Krischer (Chemical Physics Beyond Equilibrium) in the person of Simon Filser. The electrochemical experiments were performed in a one-compartment cell made of polytetrafluoroethylene (PTFE) and quartz glass, sealed with fluoroelastomer o-rings. The reference electrode used is a saturated mercury sulfate electrode (sat. MSE), and a glassy carbon rod is used as the counter electrode. For better comparability, electrochemical potentials in the following are given versus the reversible hydrogen electrode (RHE). The EC-cell is cleaned in concentrated caroic acid and the samples in acetone and ethanol before use. The electrolyte is 0.1 M $KHCO_3$ at pH 6.8 saturated with CO_2 (purged with CO_2, purity 4.5), which is a common electrolyte for CO_2 reduction reaction (CRR)[82]. Here, it is buffered with a 0.1 M phosphate buffer at a pH of 6.8 obtained by the addition of 50 mM K_2HPO_4 and 50 mM KH_2PO_4. It is mixed using Normapur (VWR, USA) or Suprapur (Merck Millipore, Germany) purity grade chemicals in ultrapure water (18.2Ωcm). For the photoelectrochemical measurements, a Zennium potentiostat is used. The sample is illuminated from the front through the electrolyte by a TLS-03 tunable light source (Zahner, Germany). The cyclic voltammograms (CVs) are corrected from electronic artifacts by subtraction of a linear slope and smoothing with a 5 point adjacent averaging filter.

7.4.5 Differences in photoelectrochemical properties of nTP and LO-NIL nanostructures

The possible performance of samples with gold photoelectrodes fabricated by nTP and LO-NIL is first evaluated with simple photoelectrochemical measurements. Figure 7.15 shows cyclic voltammograms recorded under illumination with a wavelength of 848 nm and an intensity of 5 W/m^2, using a buffered 0.1 M $KHCO_3$ electrolyte at pH 6.8 saturated with CO_2. The chosen pH value is preventing the degradation of the silicon surface. They show several features that give hints about the different performance of the samples (and are marked in the figure):

1+2 The typical gold oxidation and gold oxide reduction features are clearly visible in the CV of the LO-NIL sample. For most nTP samples, these features are not visible, which is interpreted as a disturbed current transfer. This is in contrast to the LO sample that clearly shows the features. It has to be mentioned that some of the nTP samples do show these peaks, but

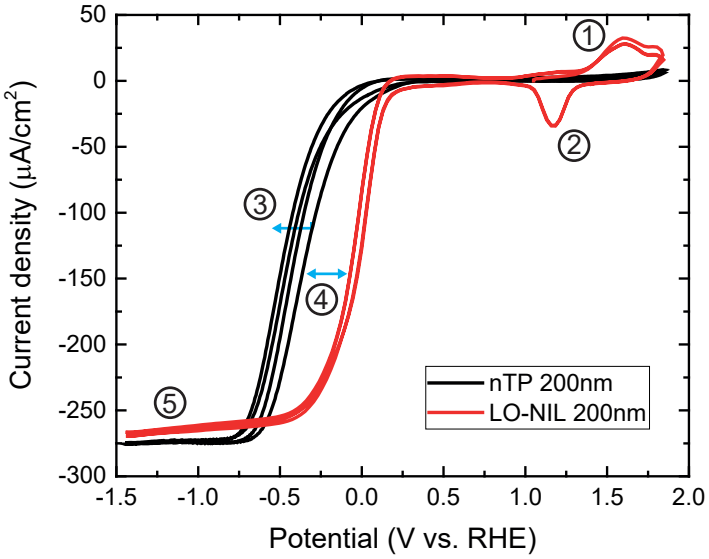

Figure 7.15: Cyclic voltammograms in buffered 0.1M $KHCO_3$ saturated with CO_2 and under illumination with a wavelength of 848 nm and an intensity of 5 W/m^2. An nTP sample (black) and LO-NIL sample (red) are shown. Compared to the nTP sample, the over-potential of CO_2 reduction and hydrogen evolution on the LO-NIL sample is reduced by almost 400 mV, the typical features of gold oxidation and gold oxide reduction are clearly visible.

most of them are not.

3 The onset potential of the reduction reactions on the nTP sample gets more negative after each scan, which is interpreted as a degradation of the structures. The LO-NIL sample is much more stable in this respect.

4 Most importantly, the onset of the hydrogen evolution (HER) that happens simultaneously to the CO_2 reduction (CRR) is shifted by approximately 400 mV to a lower overpotential for the LO-NIL sample compared to the nTP sample.

5 A saturating reduction current density is reached for larger negative potentials due to a limitation in electrons, which are generated by absorbed photons. The attainable current density is in good approximation proportional to the number of photoelectrons and, thus, to the illumination intensity. The LO-NIL gold structures shown here are slightly larger than the nTP ones. As a result, the number of photons actually reaching the absorbing silicon, and therefore the saturation current density for negative potentials is reduced.

In the following, the root cause of these differences is analyzed.

7.4.6 Roughness and defects comparison of nTP and LO-NIL

Differences in EC reactivity of samples made by different fabrication methods can be caused by changes in surface morphology of the metal electrodes, in particular, the surface and edge roughness. For example, it is reasonable to assume that the direct deposition of metal under high vacuum conditions results in a well-defined metal/air surface and a substrate/metal interface. Additionally, different methods may lead to more defect sites on the atomic scale, which are known to increase EC reactivity.
Thus, the morphology was examined with high-resolution AFM measurements using RMS roughness evaluation. Therefore, 200 nm squares (3 nm Ti - 18 nm Au) were fabricated with nTP and lift-off nanoimprint lithography (LO-NIL). Atomic force microscopy was performed using ultra-sharp tips with a tip radius of <1 nm (SHR 150, budgetsensors, Bulgaria) for high-resolution measurements. An RMS roughness of $\approx 1.7 \pm 0.7$nm was extracted for nTP samples and a value of $\approx 0.4 \pm 0.1$ nm for the LO-NIL ones (Figures 7.16(b) and 7.16(c)).

Additionally, the line edge roughness (LER) was extracted from SEM images, which is calculated as the standard deviation of the distances between the individual edge locations from the fitted edge line. For the transfer printed samples, a value of $\approx 4.8 \pm 0.9$nm and for the lift-off samples, a considerably smaller value of $\approx 2.0 \pm 0.5$nm were found.
As already discussed in chapter 6, the sidewall coating of the stamp protrusion cannot be avoided with nTP. This leads to the formation of metal dots, which will eventually stick to the edges of the transferred metal layers resulting in ear defects visible in figure 7.16(a). Less to none ear defects with the lift-off technique is observed. On a larger scale, metal contact pads (micrometer-sized) tend to have small holes if the metal layer is very thin. This can be attributed to thermal and mechanical stresses during the transfer process but does not affect smaller structures. Overall, samples fabricated with LO-NIL exceed the nTP prepared samples in feature accuracy and surface properties.

7.4.7 Interfacial properties of metal-/semiconductor contacts fabricated with nanoimprint technologies

The properties of the metal-/semiconductor interface are examined in this section. A typical characterization method for this purpose can be transmission electron microscopy (TEM). While this offers high-resolution images of the interface, the

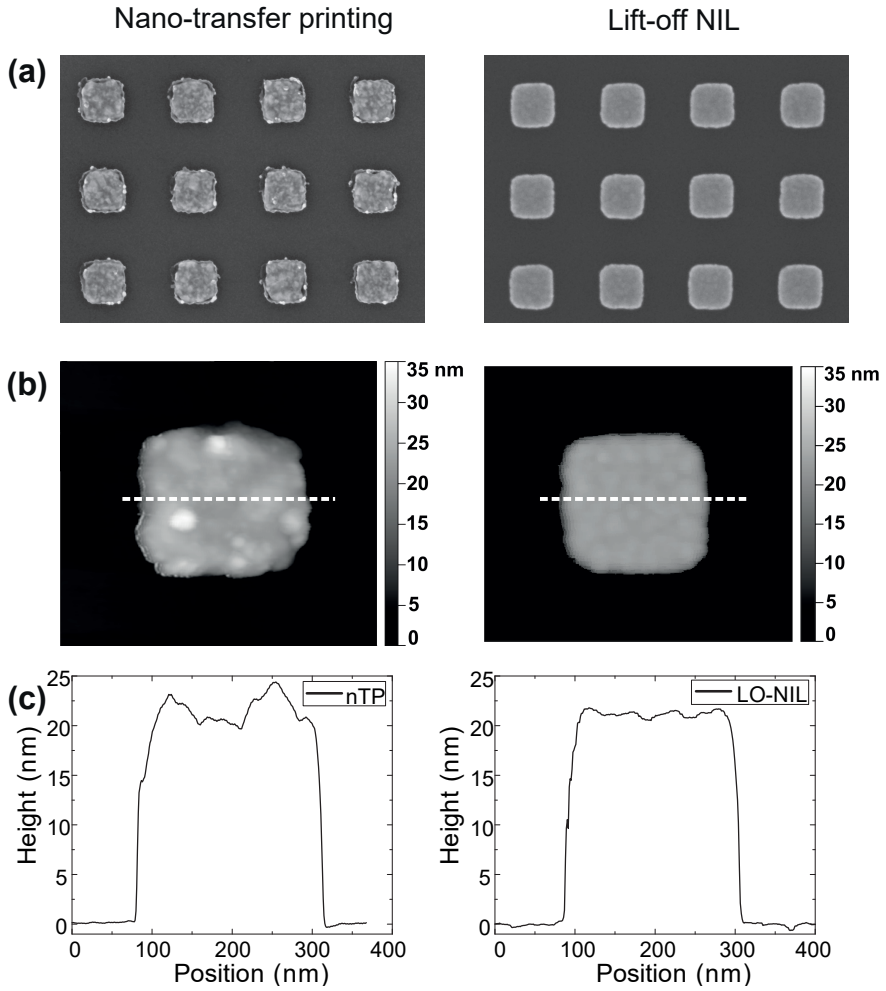

Figure 7.16: Roughness characterization of nTP and LO-NIL samples. (a) SEM top-view image of 18 nm Au/3 nm Ti 200 nm squares on a silicon substrate, (b) AFM image of a single metal nano-pad. The RMS roughness was measured to be $\approx 1.7 \pm 0.7$nm (nTP) and $\approx 0.4 \pm 0.1$nm (LO-NIL). (c) Center height profile extracted from the AFM images in (b). Reprinted from Nagel et al.[13] with the permission of AIP Publishing.

preparation is complicated, and only slices of the sample can be characterized (also destroying the sample). Here, plasmonic resonances are used instead as a non-invasive technique.

In order to obtain a meaningful evaluation of the interfacial properties with a plasmonic experiment, a variety of different samples have to be recorded. Plasmonic properties, in particular the wavelength of the major resonance, are depending on many parameters. The results are compared to simulations based on FEM Simulations (Comsol Multiphysics) (see section 7.3) and on FDTD simulations (Lumerical Solutions) by the work of Tianyue Zhang from the group of Prof. Feldmann (Ludwig-Maximilian's Universität München). Since Si is not transparent in large parts of the relevant spectrum, only reflectivity measurements were

performed for the structures on Si. All spectra are normalized to blank substrates without nanostructures, while the simulations are normalized relative to reflectivity values from Chelikowsky and Cohen[91].
The optical characterization of the samples was performed using reflectivity spectra. They were recorded on a Perkin Elmer UV-VIS-NIR spectrometer Lambda 900 in reflectivity mode. The spectra are normalized to the standard baseline to correct for an intensity reduction by misalignment of the beam due to a sample tilt. Measurements with nanostructures are related to blank silicon samples. Transmission spectroscopic measurements are done on a Varian Cary 5000 UV-VIS-NIR absorption spectrometer. SEM images are taken with a Zeiss NVision 40.

Characterization using plasmonic resonances

Figure 7.17 (I) shows the plasmonic resonances spectra of a series of samples with varying structure sizes fabricated by LO-NIL. The structures with sizes below 130 nm are nanodisks with a periodicity of 90 nm and 150 nm for structure size of 45 nm and 75 nm (tuned up to 130 nm), respectively. The ones larger than 200 nm are squares with rounded corners and periodicity of 430 nm. They consist of 3 nm Ti and 18 nm Au metal layers. The main trend, a red-shift of the plasmonic resonance with increasing size, is observed in the experiment as well as in the simulations and shown to be very similar for both (Figure 7.17 (c)). Simulated data in figure 7.17 (b) are produced with an FDTD model made by Tianyue Zhang, the results in (c) are produced by a FEM model using COMSOl Multiphysics as presented in the previous section. Both simulation methods gave almost identical results. FDTD simulations are chosen in (b) because they were already published[13] while in (c) more extensive studies results are presented. Here, the simulated resonance peaks strongly depend on the native oxide thickness of the silicon substrate, resulting in a blueshift of the resonance peak for thicker oxide layers.
Figure 7.17 (II) shows the plasmonic resonances spectra of 200 nm samples with varying gold thicknesses. The peaks blue-shifts for thicker gold layers and are in perfect agreement with the simulation model. Overall, as the simulation models precisely predict the device behavior it is possible to study unexpected measurement results and find the origin of the causing changes.

Figure 7.18 (a)+(b) shows a comparison of nanostructures fabricated by nTP and LO-NIL. While LO-NIL samples exactly match the expected results, the nTP

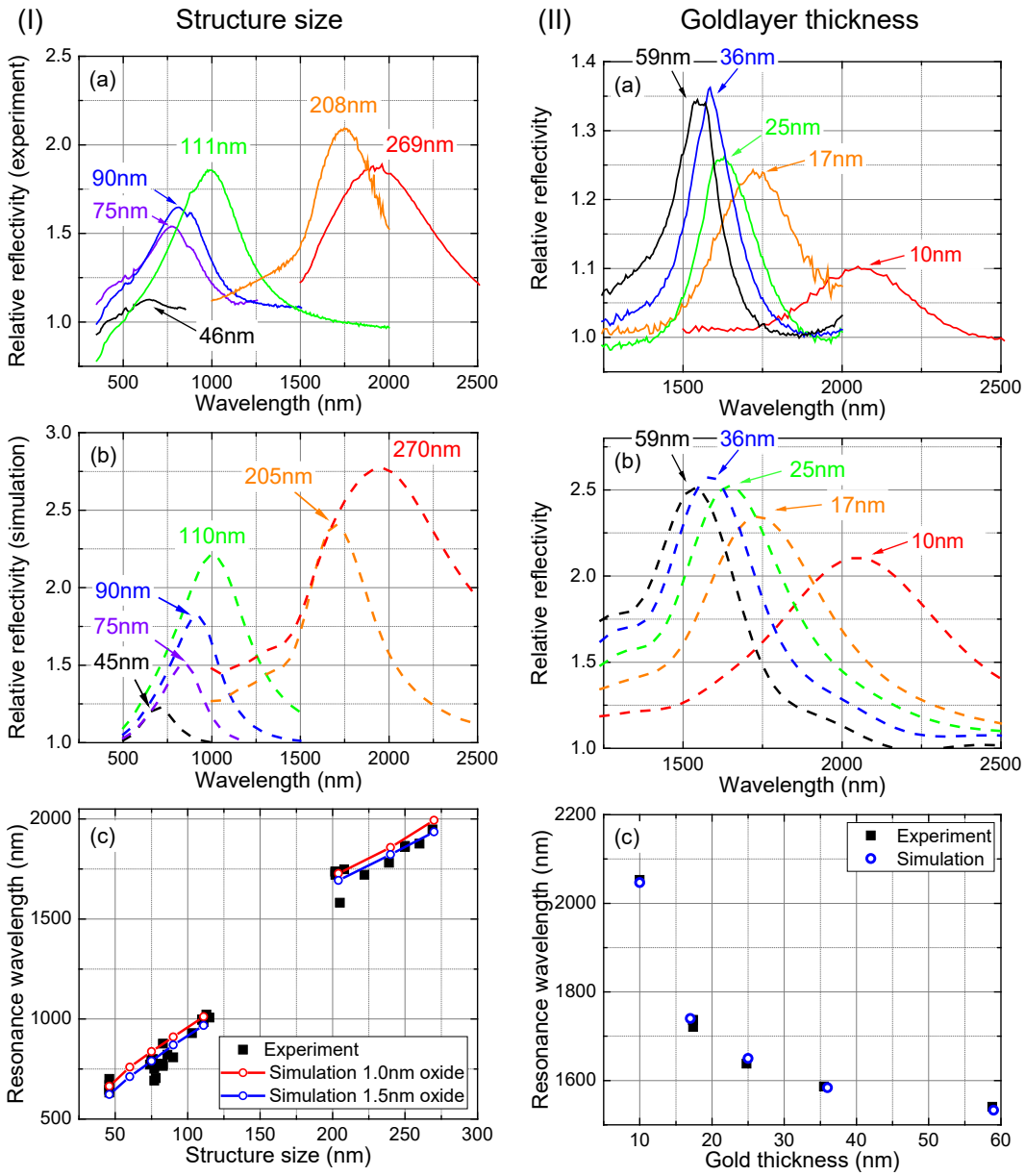

Figure 7.17: Comparison of plasmonic resonance peaks with simulated ones of a FEM (Comsol Multiphysics) and FDTD (Lumerical Solutions) model. (I) size-dependent using 3 nm Ti/18 nm Au metal layers and (II) metal layer thickness-dependent of 200 nm squares. (a) gives selected experimental UV-Vis measurements of the relative reflectivity, (b) the corresponding simulated spectra using FDTD, and (c) Lorentz peak fit values for all samples and FEM simulated peaks structures of the same size with two different native oxide thicknesses between the silicon substrate and the metal. Adapted and reprinted from[13] with the permission of AIP Publishing.

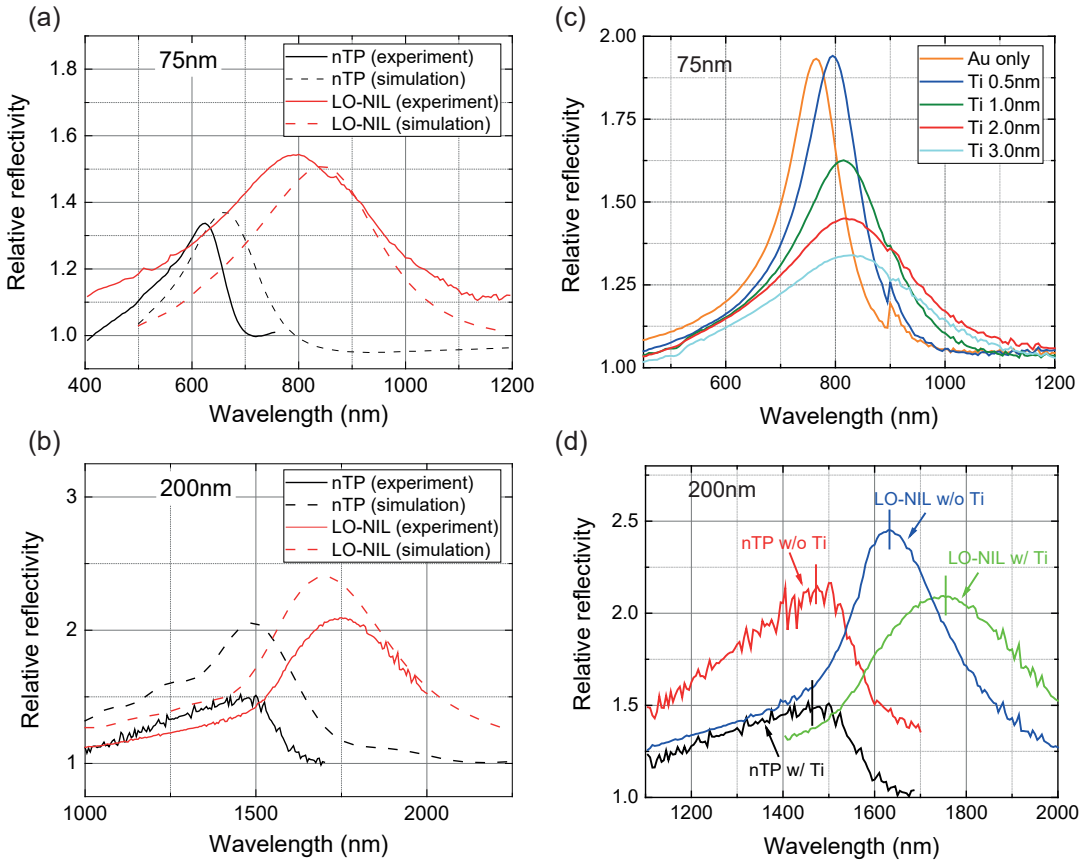

Figure 7.18: (a)+(b) Comparison of the plasmonic resonance peaks of nanostructures fabricated by nTP and LO-NIL. The experimental data (straight line) is also compared to the simulated spectra (dashed) both for 75 nm and 200 nm feature sizes on a Si substrate with 3 nm Ti/18 nm Au. The simulation model of the nTP includes an interfacial 2 nm wide air gap. (c)+(d) Experimental data of plasmonic resonance damping caused by the titanium adhesion layer. A drastic reduction in intensity is visible with thicker layers. Adapted and reprinted from Nagel et al.[13] with the permission of AIP Publishing.

samples have a strong blue-shift for all feature sizes, as can be seen in the figure. The root cause of this difference will be discussed later. In figure 7.18 (c), the effects when having titanium as an adhesion promoter between substrate and gold can be found. It clearly has a strong impact on the plasmonic resonance intensity as the titanium layer is damping this effect even when having the smallest layer thickness of less than 1 nm. This effect has to be taken care of, when designing a photonic energy conversion device. The small kink at 900 nm originates from a change of the photon detector of the UV-Vis-NIR during the measurement. (d) A direct comparison of the blue-shift with and without a titanium layer. Using a titanium layer, the blue-shift is more prominent.

7.4.8 Discussion

There are two key differences between the experimental and the simulated data. First, the peak intensity is lower for the experiments, and second, the experimental peaks are, on average, slightly blueshifted with respect to the simulated ones. The lower relative reflectivity intensity is mainly an artifact since the spectrometer geometry allows only very small angular deviations from the specular reflection in the reflected beam while all reflected light is considered in the simulations. The reason for the latter can be the imperfect shape of the experimental structures, especially the rounded edges, which is in line with Rodriguez-Canto et al., who examined comparable structures and observed a similar blueshift[46]. The increase of the blueshift for smaller structure sizes is in line with this interpretation, where the statistical scatter is larger. As presented in subfigure (I)(c), assuming a native oxide thickness of 1.5 nm is in better agreement with the experimental data. Typically, native oxides of silicon wafers are determined to be around 1.6 nm with ellipsometry. Here, freshly etched and plasma-oxidized wafers are used, where the plasma-oxide is slightly smaller. However, it is possible that the assumed thickness of the native silicon oxide of 1 nm is slightly underestimated in the simulation model. Additionally, roughness and graininess of the evaporated metal layer may result in small voids at the interface, changing the refractive index locally and leading to a blue-shift, which is more prominent for nTP samples.

The LO-NIL method enables tuning of the plasmonic resonance frequency and peak width by adjusting the metal layer thickness. The resulting red-shift with decreasing layer thickness is shown to be identical in experiment and simulation. This means that a decreasing aspect ratio (height/diameter) leads to a red-shift, which is in accordance with various previous works[92–94] as well as an increasing overall diameter[95]. Also, the results when having a Ti adhesion layer between gold and substrate is in accordance with the literature[96–98]. The resonance frequency is only slightly shifted, including a 3 nm Ti layer, but a strong reduction of the plasmonic scattering can be observed.
Even more striking is the strong blue-shift in the resonance of nTP structures compared to LO-NIL samples with nominally very similar parameters. Since the substrate and dimensions of the nanostructures are practically identical in both techniques, it is expected that this deviation is due to differences in manufacturing methods, which may be defects and imperfections, the morphology of the metal and its material and interface properties. There is strong evidence that the interface between metal and semiconductor is responsible for this shift. Typ-

ically, deviations from the ideal shape of the nanostructures lead to a red-shift of the resonance peak rather than to a blue shift. Thus it can be excluded as an explanation for this effect, as shown in the following. First, as presented in figure 7.16, samples fabricated with nTP indeed show an increased surface roughness and ear defects compared to LO-NIL. The influence of both ear defects in the form of edge grains[99] and surface roughness[100,101] on the plasmonic response of metal nanoparticles is reported to be a red-shift of the resonance. In addition, it has been shown that annealing of gold films at 200°C for 5 min (which is nearly identical to the nTP process parameters) can result in a smoother surface and lower edge roughness[99,102,103] as well as in changes of the dielectric function of gold, where an improved grain structure results in a decrease of the imaginary part of the dielectric function[99,104]. This would have the effect of a resonance blue-shift for annealed gold squares[104]. However, since the nTP samples showed an increased surface roughness compared to the lift-off one, after all, it can be discarded as an explanation. Hence, surface roughness and defects as well as material properties are not expected to be the source of the blue-shift in resonance wavelength in the first place as they lead to a shift in the opposite direction. Yet, there is the possibility of a difference in the metal/semiconductor interface for the two preparation methods due to surface roughness. For the LO-NIL samples, the metal atoms are deposited onto the substrate under high vacuum conditions and should form an almost atomically flat interface, where only the formation of grains can lead to a small number of voids at the interface, which is in line with the performed simulations. In contrast, it is reasonable to assume that the printing of a metal surface with a surface roughness of a few nanometers onto a hard silicon oxide surface leads to the formation of holes between native silicon oxide and the Ti layer. Those voids lead to a change of the dielectric properties at the interface due to an additional volume with a refractive index lower than the one of Si and a correspondent change in the resonance wavelength. Since the structure of the assumed inhomogeneous Ti/SiO_2 interface is not exactly known and including an artificial roughness of a few nanometers would drastically increase the computation time, a simplified model was used in the simulations: Instead of presumed air inclusions of about 2-5 nm size, a 2 nm wide continuous layer of air between Ti and SiO_2 is included in the simulation model. The used thickness is justified by the measured RMS roughness of the nTP samples shown in figure 7.16. The results give a good prediction for the shift of the resonance (figure 7.18). To further study the effect of the interface bonding on the plasmonic properties, glass as a substrate with a lower refractive index was used. These measurements

show that the blue-shift of the nTP samples compared to the LO-NIL samples is reduced compared to the effect measured on Si substrates. Since the optical values of the dielectric function of air and vacuum ($\epsilon = 1$) are much more similar to glass ($\epsilon \approx 2.25$) than to silicon ($\epsilon \approx 15.5$) (at an exemplary wavelength of 600 nm),[45] the effect of an additional layer with a lower dielectric constant is more pronounced on Si.

The silicon-metal interface is also altered by the oxygen plasma treatment of the metal on the stamp and the fact that the titanium surface is under ambient conditions before the nTP, so that it is certainly partially oxidized, resulting in an additional TiO_2 layer between SiO_2 and Ti. In chapter 6, section 6.4, it was already shown that for oxygen plasma conditions comparable to the ones used on the titanium layers, no oxide could be found and a thickness <1 nm was estimated. Since even a very thin oxide layer could lead to a huge shift in the resonance peak wavelength, it is necessary to separate the effect of an oxide layer from roughness-induced voids. Therefore, nTP and lift-off samples with and without a titanium adhesion layer were measured, as shown in figure 7.18(d). Due to the vacuum deposition of the metal layers in the LO-NIL process, Ti oxidation can be excluded there. Even without a titanium layer and thus without the possibility of an additional oxide layer, the nTP samples are dominantly blue-shifted compared to the LO-NIL samples. This result further supports the assumption that the surface roughness of the metal film on top of the stamp will lead to voids in the later metal/substrate interface in the nTP process. However, the blue-shift shift of the resonance peak is larger on samples with a titanium layer. This indicates that also a thin titanium oxide layer is formed during the nTP process or that the interface roughness is higher with a titanium layer, which would both lead to an additional blue-shift compared to the lift-off method. The deviations in the structure dimensions are about 2 nm in thickness resulting in a relative shift of the resonance of about 2% for typical thickness values and about 5 nm in diameter, leading to a relative shift in the resonance of 3% for the smallest and 1% for the largest structures. The main error in the reflectivity spectra is a deviation in the intensity of about 5% resulting from a sample tilt while the wavelength accuracy is estimated to be about 1%.

This result of a bad Si-metal interface also explains the differences in cyclic voltammetry and electrochemical and energy conversion performance of nTP and LO-NIL samples already shown in figure 7.15. First, the shifted onset potential of HER and CCR by 400 mV can be attributed to this bad contact or a poorly conductive TiO_2 layer. This additionally explains the missing gold oxidation and

gold oxide reduction features, which also proves a disturbed current transfer for nTP samples. This is in sharp contrast to the LO samples that clearly shows the features. In section 6.4, it was proven that devices fabricated with nTP have comparably the same electrical properties as the LO-NIL ones. Thus, the change in properties has to be part of the working environment in the electrochemical cell. It is assumed that the reduced stability of the nTP samples and the disturbed current transfer is caused by electrolyte penetrating the metal/semiconductor interface since the layers are not perfectly laminated to each other. Parasitic reactions at the interface could either further oxidize the Ti or increase the size of the voids. Finally, forming hydrogen and carbon-dioxide gas can also lead to the complete removal of single nanostructures from the substrate.

7.4.9 Summary

Both nanofabrication techniques have a very high feature resolution in the sub-50 nm regime and have the potential for high-throughput and large area patterning. While in nTP the minimal feature size is just limited by the resolution of the stamp, LO-NIL is limited due to the needed under etching of the imprint resist before metal evaporation, which is the most critical step in the process. Although this leads to higher process complexity, LO-NIL offers the possibility of HV-PVD (resulting in excellent interface properties), ideal shape retention, and low surface roughness (Table 7.4). It has been shown that the plasmonic resonance peak wavelength is not only dependent on the size and shape of the nanostructures but also on a well-defined metal/substrate interface. It was found that the plasmonic resonance peak wavelength is blue-shifted for samples made by nTP compared to others made by LO-NIL due to voids at the interface. The latter technique also allows the tuning of the plasmonic resonance peak wavelength by varying feature sizes and metal thickness. Larger dimensions and thinner metal films result in a red-shift. In addition, the metal/substrate interface is very important for electrochemical applications since the smooth interface of the direct evaporation in the LO-NIL process leads to more stability, a lower overpotential for water splitting, and CO_2 reduction and better visibility of typical electrochemical features.
All of these electrochemical features show that LO-NIL is a suitable method for the fabrication of plasmonically and electrochemically active gold nanostructures while nTP yields structures with a much lower performance. For different applications, e.g., nano-contacts and circuits or in organic electronics, nTP can be of advantage because of its less complex and fast process[105].

Table 7.4: Fabrication method comparison.

	nTP	LO-NIL
Minimal structure size	++	+
Large area / Scalability	++	++
Surface / edge roughness	0	++
Process complexity	++	-
Interface properties	-	++
Feature size adjustable	No	Yes
Chemical free	Yes	No

++ Excellent | + Very good | O Acceptable | - Challenging

7.5 Photoelectrochemical reactivity and size effects of nanostructured electrode arrays in CO2-saturated aqueous electrolyte

7.5.1 Introduction

In this section, the activity of metal-insulator-semiconductor (MIS) photocathodes with arrays of nanostructured metal arrays between 75 nm and 1400 nm over macroscopic dimensions (5x5 mm^2) is studied. The aim is to contribute to the fundamental understanding of size-dependent effects of metal electrodes on their electrochemical reactivity. Here, the electronic properties of the MIS are not specially optimized, i.e., the photovoltage. The photocathodes are composed of Au/Ti/SiO_2/p-Si structures that are used for water splitting, and CO_2 reduction experiments in a CO_2 saturated and phosphate-buffered electrolyte. Parts of this section have already been published and are taken from Filser et al.[90]

7.5.2 Sample preparation

Silicon wafers are used as substrates of the following type

- P-type silicon: CZ(111) ±0.5, 5-25 Ωcm, Boron doping: $5{\cdot}10^{15}{-}4{\cdot}10^{16} cm^{-3}$, single side polished, Si-Mat, Germany
- P^{++}-type silicon: CZ(111) <0.01 Ωcm, Boron doping: $> 1{\cdot}10^{19} cm^{-3}$, single side polished, Si-Mat, Germany
- N^{++}-type silicon: CZ(100) 1-5 Ωcm, Phosphorus doping: $1 \cdot 10^{15} - 5 \cdot 10^{15} cm^{-3}$, single side polished, Microchemicals GmbH, Germany

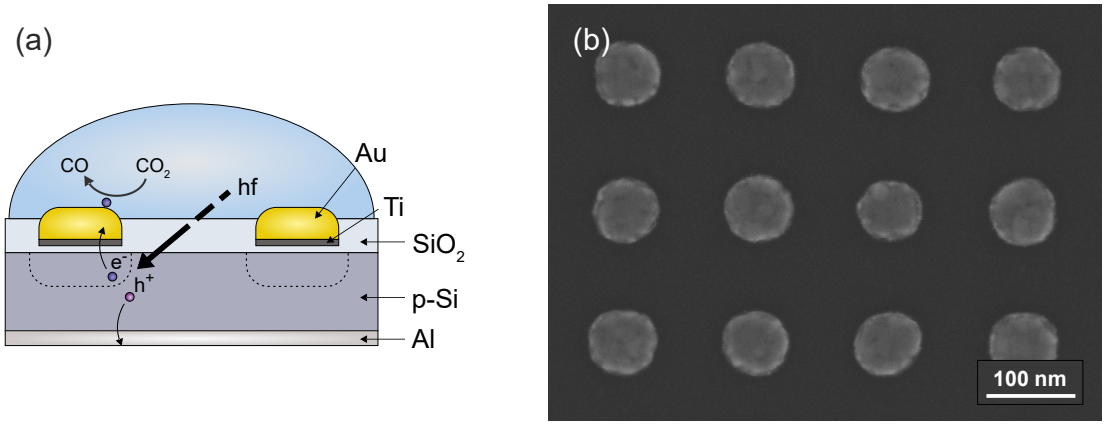

Figure 7.19: (a) Sketch of the sample design used in this section. Ti/Au metal nanoelectrodes are fabricated with nTP and LO-NIL on a p-type silicon substrate and are embedded in a 15 nm thick SiO_2 layer. The back contact consists of aluminum, while the sample is illuminated from the top through the electrolyte. (b) close-up SEM image of a sample with 75 nm disks.

Samples are prepared similarly to the previous section, with the following adjustments (see figure 7.19): First, the metal structures are embedded in a SiO_2 layer. Therefore the wafers were thermally oxidized at 1000°C for 8 min, resulting in an oxide thickness of about 30 nm. The aimed final thickness of 15±1 nm is achieved by thinning of the layer with a buffered oxide etch procedure (98:2 mixture of 40% ammonium fluoride (NH_4F) and 50% hydrofluoric acid (HF)). The backside contact consists of a 200 nm Al layer annealed at 250°C for 15 min for n-Si and 400°C for 30 min for p-Si and p^{++}-Si. LO-NIL is performed with standard process parameters. After patterning and under etching are performed, an intermediate oxide etching step is included. Here, additional RIE is applied to remove the 15 nm thick thermal SiO_2 layer only at the patterned openings, thus right at the spot below the future metal nanostructures. The opened pure silicon wafer surface is again covered by a thin plasma oxide layer, using the RIE (while still inside the chamber) with a short pure oxygen plasma step to get the same MIS stack properties as with the samples in the previous section. After this step, the Ti/Au layer is evaporated, and Lift-off is performed as usual. With this adjustment, the metal electrodes are embedded in the oxide layer, and the surrounding silicon surface is passivated by this thick oxide layer, which remained on this part of the surface. The stability and effectiveness of this passivation layer have been proven to prevent unwanted current flow over the SiO_2/Si interface[90]. A sketch of the layout is given in figure 7.19 (a) and an SEM image of the final device in figure 7.19 (b).

7.5.3 Photoelectrochemical measurements and product analysis

Figure 7.20: Picture of the EC-cell. The sample is mounted in the center of the EC-cell and sealed with an O-ring. It can be illuminated either from the backside or from the front through the electrolyte.

The measurements were performed in a three-compartment cell, as in the previous section. The compartment cell is separated from the gold counter electrode and the MSE reference electrode by a Nafion membrane. The electrolyte is a 75 mM potassium carbonate (K_2CO_3) electrolyte buffered with 100 mM phosphoric acid in a composition, which is equal to phosphate buffer with pH 6.8. The electrolyte is purged with CO_2. The cell resistance was determined to be 59Ω. The measurements were recorded using a Zahner CIMPS-QE/IPCE system with a TLS03 tunable light source. Gaseous products were analyzed with a Shimadzu GC-2010 Plus gas chromatograph equipped with a barrier ionization discharge detector BID-2010 Plus and a Restek ShinCarbon ST Micropacked Column. EC measurements and product analysis in this section were performed by the group of Prof. Krischer, TUM. Liquid products were neglected in the measurements as they have less than 1% faradaic efficiency for Au electrodes[82]. A picture of a mounted sample inside the EC-cell can be found in figure 7.20.

Characterization of electrode size dependent effects

Parasitic current flows and chemical activity under illumination were characterized by electrochemical linear sweep voltammograms (LSV). In figure 7.21, p-type silicon substrates decorated with an array 200 nm Au squares and 240 nm inter distance on a 2x2 mm^2 patterned area are shown in the dark and under illumination for different illumination intensities. Light at a wavelength of 444 nm is being

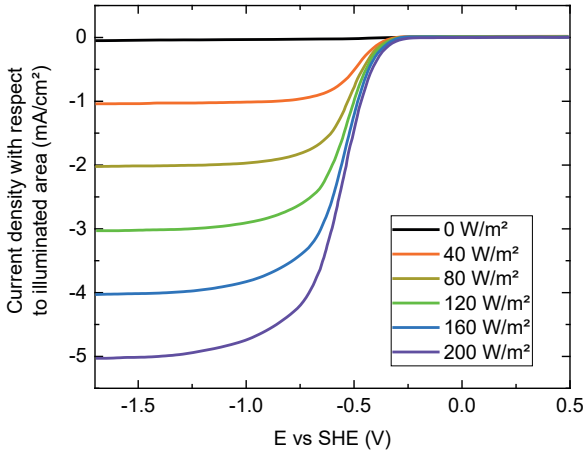

Figure 7.21: Linear sweep voltammograms of 200 nm Ti/Au squared electrodes with 240 nm inter distance in 75 mM K_2CO_3 buffered with 100 mM H_3PO_4 and purged with CO_2. Various illumination intensities with light at 444 nm wavelength are shown. Adapted from [90].

used with a FWHM of 12 nm. In the dark no significant current flows in the entire potential range, thus parasitic currents are neglectable. The onset potential is around -300 mV vs SHE. The current saturates for higher (more negative) potentials. The saturation level is directly proportional to the illumination intensity.

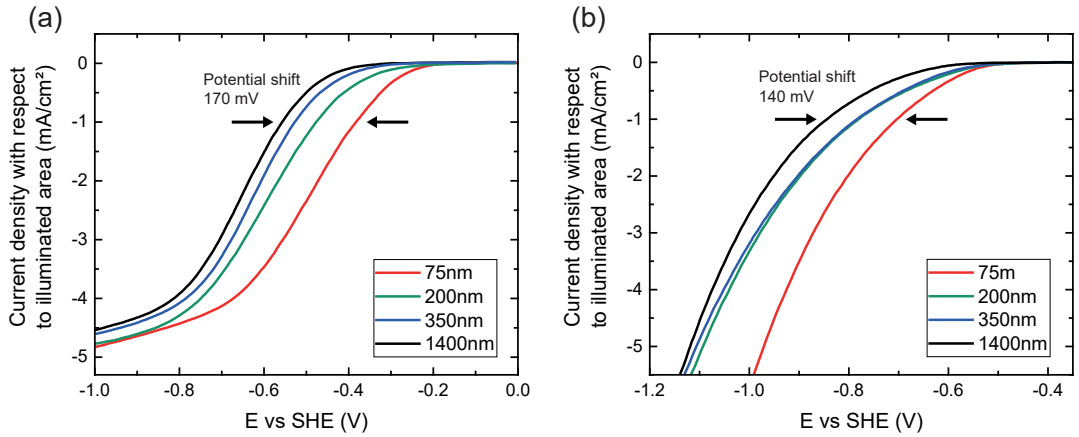

Figure 7.22: Linear sweep voltammograms of nanostructured Ti/Au electrodes with sizes of 1400 nm, 350 nm, 200 nm and 75 nm in 75 mM K_2CO_3 buffered with 100 mM H_3PO_4 and purged with CO_2. (a) on a p-Si substrate (5-25Ωcm) under illumination with light of 444 nm wavelength and 200 W/m^2 intensity. The onset potential for CRR and HER is reduced with smaller feature sizes. The potential shift between the 1400 nm and the 75 nm structured electrodes is around 170 mV. (b) on a degenerated p^{++}-Si substrate without illumination. The potential shift follows the same trend as on the p-Si with illumination. The overall shift is around 140 mV. The figure is adapted from [90].

In figure 7.22 LSV of samples of different structure sizes are shown both on a

p-Si and a degenerated p^{++}-Si substrate in 75 mM K_2CO_3 buffered with 100 mM H_3PO_4 and purged with CO_2. This gives further insight into the size effects of the catalytic nanoelectrodes on their electrochemical activity. Figure 7.22 (a) gives LSVs, current normalized to the illuminated area. The samples are illuminated with light of 444 nm wavelength and 200 W/m^2 intensity. Here, the onset potential of CRR and HER shifts to lower over-potentials with smaller structure sizes. Four different sizes have been examined: the 1400 nm, 350 nm, and 200 nm samples are nanosquares on a 2x2 mm^2 structured area, while the 75 nm samples are nanodisks. They have a metal to silicon filling factor of 20-22%, where the 350 nm samples have a slightly increased FF of 25%. However, although the coverage of the 350 nm samples is higher than of the rest, it very well follows the found trend. At a faradaic current density of 1 mA/cm^2, the difference in potential between the sample sets with the largest structure size of 1400 nm and the smallest 75 nm ones is around 170 mV.

In order to rule out effect originating from the metal/semiconductor interface, same experiments have been performed without additional illumination on a degenerately doped p^{++}-Si substrate with a specific electrical resistance of below <0.01 Ωcm, thus having an ohmic contact of the MIS structure (figure 7.22 (b)). The same trend of a reduction in over-potential with smaller feature sizes is clearly visible.

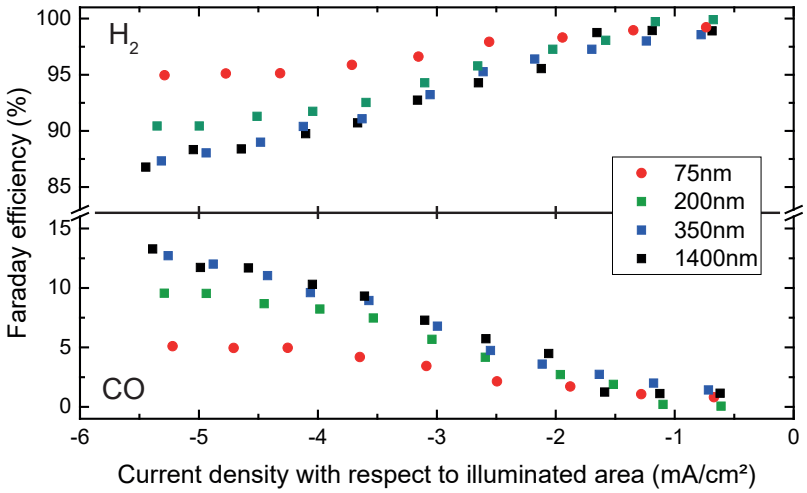

Figure 7.23: Gaseous product analysis of electrolysis measurements p-Si samples with nanostructures Ti/Au electrodes under illumination. The faradaic efficiency of the products is given with respect to the illumination-limited current density at a potential of -1.76 V vs. SHE. Taken from Filser et al.[90]

Gaseous product analysis of electrolysis measurements has been performed. The results are presented in figure 7.23 for differently sized Au structures on p-Si

substrates under illumination at a constant applied potential of -1.76 V vs SHE. The current under these quasi-galvanostatic conditions is adjusted by a variation of the light intensity[90]. Liquid products were neglected in the measurements as they have less than 1% faradaic efficiency for Au electrodes[82]. The current density of the LSV presented before originates from water splitting (HER) and CO_2 reduction (CRR). The only detected products are hydrogen and carbon monoxide, which is in accordance with the literature on Au electrodes[106] (also see table 7.3). The faradaic efficiencies increase with higher over-potentials until the illumination-limited saturated current density plateau is reached. Then, the efficiencies stay approximately constant. Overall the CO Faraday efficiency increases for more negative current densities. Additionally, it decreases with decreasing structure size. The values for the 350 nm and 1400 nm samples, however, are almost identical. On the contrary, the hydrogen evolution has a stronger enhancement for decreasing sizes.

7.5.4 Discussion

In electrochemical experiments, it is typically complicated to address measured effects to their physical and chemical origins. Besides chemical effects, the sample design can have a huge influence on the results. Especially when the findings are connected to a size effect of sample design elements. In the following, a discussion of the size-related increase in electrochemical activity is presented. With the help of nanoimprint technologies, it is possible to exclude individual effects as the root cause of this activity increase.

First, the LSV of structured electrodes on p-Si under illumination (figure 7.21) proves a working electrochemical energy conversion device. Under illumination, photogenerated electrons in the absorbing substrate are transferred to the electrode surface due to the rectifying behavior of the Schottky contact (figure 7.2). There, the electrons can undergo a Faradaic reaction in the given electrolyte. The Faradaic current density increases for more negative potentials until it becomes more and more limited by the generation rate of photoelectrons, and the current is entirely limited by the incoming photon flux. This results in a saturation of the current and the reaction rate. The saturation level in this regime is directly proportional to the illumination intensity, which is typical for a photoelectrode exhibiting a Schottky contact under reverse bias.
The activity of nanostructured Au arrays on SiO_2/Si for water splitting and CO_2 reduction increases with decreasing electrode size between 1400 nm and 75 nm,

and especially when below 350 nm. This effect was found to occur on illuminated p-Si substrates, p^{++}-Si substrates in the dark (figure 7.22) and also on n-Si in the dark[90].

This proves that the shift is not caused by a difference in photovoltage for different samples and feature sizes, which would also manifest itself in a shift of the j-U-curve to more positive potentials (lower over-potentials).

Characterization of the Schottky contact behavior showed nearly identical j-U curves for all samples[90]. This was done by evaporating an additional gold layer on top of the patterned area, electrically connecting all nanostructures, thus being able to measure all MIS structures at once. At a current density of 1 mA/cm^2 the individual potentials deviated by only 12 mV, which is an order of magnitude less than the measured potential shift of the linear sweep voltammograms between the 1400 nm and the 75 nm samples.

Both findings strongly suggest that this is an electrochemical or catalytic effect rather than a solid-state effect from the MIS structure.

For arrays of small patterned electrodes, the diffusion profile of the reactants towards the active surface is intrinsically optimized compared to a flat and fully covered electrode surface. For a bulk-catalyst material, the reaction species are delivered to the catalyst surface by planar diffusion, while for small catalyst particles, spherical diffusion takes place. This diffusion profile could further be optimized when changing the patterned electrode dimensions. In the presented experiments, it is very interesting to see that the individual LSVs for the various electrode dimensions are only shifted on the potential axis. This means that the enhancement also occurs for very small, thus kinetically limited current densities. As a result, a limitation caused by a different diffusion profile to/from the small structures can be excluded. An explanation for this finding can be found in the chosen stamp layout and the perfectly ordered pattern using nanoimprint technology. It has already been predicted that diffusion to microelectrode arrays is mainly dependent on the ratio of structure size to pitch[106]. This ratio is nearly identical to the chosen nanoimprint stamps.

Chemical reactions are very sensitive to the existence of defective sites on the catalyst material[107]. Changes in the defect density would also be visible in the activation energy and reaction rate of HER and CRR. In the presented case, all metal structures are polycrystalline with a high grain and defect density. The metal deposition took place in the same evaporation machine with identical deposition rates and chamber pressure conditions. Different morphologies of the Au electrodes are therefore highly unlikely. This has been additionally checked with

double capacitance measurements normalized to the geometrical gold surface area and it was found to be independent of the structure size.
The experiments can be compared to studies of similar systems. Hinogami et al.[83] observed a significant enhancement of H_2 evolution and CO_2 reduction with illuminated p-Si electrodes decorated with Au, Ag, or Cu nanoparticles. The metal particles were well distributed in shape, and size exhibited a rather wide variety between some ten and some hundred nm. Different from this study, the electrodes were not supported by a Ti adhesion layer, and no SiO_2 was grown on the p-Si substrate. Still, the LSVs of the nanoparticle decorated samples were shifted by 500 mV compared to both the metal bulk electrodes and the continuous metal layer on top of a p-Si substrate, which showed no photo-effect in their case. It was assumed that the increase in activity leads to a change in band bending at the metal/semiconductor interface when the contact area is less than 5x5 nm^2, which they concluded from theoretical results. They, therefore, argued that the contact area between the semiconductor and the metal particles is considerably smaller than the base area of the particles or that the area is divided into many small areas instead of forming a completely covered area.

It is reported to increase the catalytic activity when very small catalyst particles (<10 nm) or only thin closed layers are used[108–110]. For small particles, the activity very much depends on the diameter, and it only changes drastically for sizes below 5 nm[111]. For thin layers, the activity of many catalyst materials increases. This is explained by Hammer, Norskov, and coworkers by a shift in the d-band center due to a strain-effect in a pseudomorphic metal overlayer on a supported material[112]. However, these layers have to be very thin. For platinum layers on gold, this effect only plays a role for a few monolayers thickness of catalyst material[108]. The presented electrodes in this thesis are rather mesoscopic in this respect, and with 18 nm thickness, both explanations should have no impact in this system.
For not fully covered surfaces, a spill-over effect can take place. Adsorbed hydrogen on the catalyst material can spill-over to the surrounding substrate, where it is energetically more favorable to form hydrogen molecules under the right conditions, which then desorbs from the surface. Esposito et al.[113] investigated H_2 evolution from protons at structured $Pt/SiO_2/Si$ photoelectrodes. Besides having Pt instead of Au as catalyst and metal structures sizes in the 100 μm range, the main difference is that the surrounding oxide layer was just 2 nm thick. The authors report a strong enhancement of the hydrogen evolution reaction for metal

structures on SiO_2, which they attributed to two effects: an inversion layer which forms at the thin insulator/electrolyte contact and the spill-over effect to the SiO_2 surface. Due to the much thicker SiO2 layer of 15 nm between the Au structures, which isolates the semiconductor from the electrolyte, both mechanisms can, however, be neglected as an explanation in the present work.
The quantity in which the structures of different sizes differ is the edge length or circumference. Normalizing the current to the circumference reduces the potential shift of the LSVs to around 50 mV[90]. It can be assumed that the enhanced activity results from the Au/SiO_2 interface at the edges of the gold structures. Au and SiO_2 have very different double layer capacitances; thus the charge distribution and double-layer structure at the transition between the metal islands and the SiO_2 surface will deviate from the situation on flat Au surfaces. Since the potential drop across the double layer as well as their chemical constituents are decisive for the rate of an electrochemical reaction, it appears natural to assume a changed reaction rate at the rim[90]. However, it is exceptionally challenging to elucidate how the changed chemical composition and the electrostatic potential close to the metal structure edge impacts the reaction kinetics. This will be the topic of future studies.

7.6 Summary

In this section, a functional solar fuel device was developed. It was shown that nanostructuring a gold electrode on a silicon substrate leads to an enhanced activity compared to the continuous Au layer and reducing the feature sizes from 1400 nm to 75 nm further increases this effect. The effect is independent of the semiconductor doping concentration and type as it is found to be evenly strong on n-Si, p-Si, and p^{++}-Si samples. The onset-potential shift on p-Si (as well as on p^{++}-Si) is found to be 170 mV between the smallest and largest structure sizes for a current density of 1 mA/cm^2. This corresponds to a reduction of the needed over-potential for HER of more than 31%, which directly means an enormous efficiency increase! The product distribution in buffered and CO_2 saturated electrolyte shows a decreased faradaic efficiency for CO production on smaller structures, which means that the selectivity is shifted more towards hydrogen evolution rather than CO_2 reduction. The performed measurements and the discussion with findings in literature prove this effect to be a purely chemical one as influences of other parameters could be excluded as explanations. A change in the chemical composition of the double layer at the rim of the gold

electrode nano-islands was suggested to be the origin of this effect.

8 Conclusion and outlook

This thesis aimed to implement and optimize nano-transfer printing and nanoimprint lithography as reliable and reproducible methods for the fabrication of metal electrodes for energy conversion applications with a focus on heterogeneous electrocatalysis. The challenges of these applications were found to be well-defined interfaces between metal and substrate and especially a clean electrode surface since even mono-layer contaminations would strongly influence any experimental results. Additionally, the effects of nanostructured electrodes on the electrochemical activity were studied. The basis of the experiments was the development of a stamp replication process, where the fabricated semi-flexible working stamps were then used in nTP and NIL processes. On the one hand, this enabled comparably large patterned areas and thus strong signals in the EC experiments, and on the other hand, this enabled reliable results as a high count of identical samples for each study could be fabricated.

Both methods have been characterized in terms of electric and optical properties, morphology, shape resolution and retention, and electrocatalytic activity. Mainly gold as a standard electrode material has been used because of its importance in electronic devices in research and industry, but also as it is known for its catalytic activity for CO_2 reduction. It was demonstrated that nTP is an attractive method for directly printing electrical circuits and devices fast and easily in a purely additive manner. Especially the separation of chemicals and structuring processes from the sample opens up a variety of new applications (e.g., in organic electronics), where standard patterning procedures are inapplicable. For applications where harsh conditions apply, LO-NIL is the better choice because the nanostructures are highly stable. It has been shown that an efficient solar fuel device can be developed, that converts CO_2 into renewable carbon fuels using solar energy. Here, the shape and size of the nanostructured electrode can help to increase the overall efficiency or to adjust product selectivity.

8.1 Key results

Transfer printing of nanostructured metal electrode arrays over large areas Typical problems regarding nTP such as master re-usability, defect tolerance, process cost, and speed have been solved utilizing a replication technique (chapter 4). Temperature and print duration have been found to be the main process parameters influencing the yield of nTP on silicon substrates (chapter 6). It was shown, that these parameters facilitate a gold atom reordering in the transfer layer, which reduces mechanical contact forces towards the stamp. Using the optimized procedure developed in this work, a high yield above 99% has been achieved repeatedly with process temperatures of around 200°C. On soft materials (e.g., organic layers) the temperature could be reduced to values below 50°C.

Realization of a lift-off nanoimprinting process for well-defined metal-semiconductor interfaces A bi-layer lift-off process with nanoimprint technology was developed (section 5.3). A sacrificial layer was introduced between the substrate and the imprint resist, enabling the formation of an artificial undercut of the imprinted pattern in an additional developing step. With this procedure, metal lift-off of thicker layers was possible with extra-low defects density and high yield. Feature size tuning was achieved during RIE using pure oxygen plasma, which enabled an increase of structure dimensions up to the pitch of the imprint stamp pattern. The addition of Octafluorocyclobutane (C_4F_8) in a 2-gas RIE approach, on the other hand, formed a sidewall passivation layer resulting in a high-resolution process with 1-2 nm feature resolution.

Realization and characterization of resist masks for nanostructured electrodes used in electrochemistry Using the imprint polymer as a mask, a nanostructured electrode could be formed out of a continuous metal layer (section 7.2). Here, only a single nanoimprint step was needed. The mask was chemically stable and contamination-free even in highly concentrated acidic electrolytes. It can be used for experiments where nanostructured electrodes can lead to new physical effects or separate and analyze effects, which are close to the measurement noise.

Proof-of-concept realization of a photoelectrocatalytic device Photoelectrocatalytic devices have been fabricated both with nTP and LO-NIL. Due to the enhanced interfacial properties of the MIS contact (evaporated under high

vacuum conditions), the LO-NIL process leads to more stability and a lower overpotential for water splitting and CO_2 reduction (section 7.4). Additionally, feature size tuning during RIE allows future studies of e.g., plasmonic catalysis effects, where the LSPR frequencies and enhanced electric field enhancements mainly depend on the electrode sizes and inter distances.

Characterization of electrode size-dependent overpotential reduction and faradaic efficiency shift of gaseous products It was shown that nanostructuring a gold electrode on a silicon substrate leads to an enhanced activity compared to continuous Au layer and reducing the feature sizes from 1400 nm to 75 nm further increased this effect (section 7.5). It was found that this effect has a chemical origin. The onset-potential shift on p-Si (as well as on p^{++}-Si) was found to be 170 mV between the smallest and largest structure sizes for a current density of 1 mA/cm^2. The product distribution in buffered and CO_2 saturated electrolytes showed a decreased faradaic efficiency for CO on smaller structures meaning that the selectivity is shifted more towards hydrogen evolution rather than CO_2 reduction.

8.2 Outlook

Copper as a catalyst material for the production of hydrocarbons Copper is unique among the metals tried as an electrode for CO_2 reduction in its producing hydrocarbons at significant current densities[114]. The hydrocarbons methane (CH_4) and ethylene (C_2H_4) are the dominant products at sufficiently negative potentials. At less negative potentials, this shifts towards hydrogen (H_2), formic acid (HCOOH), and carbon monoxide (CO).[115].
Thus, a future goal would be to substitute gold with copper as the electrode material. This can be done by just evaporating copper after nanopatterning the substrate surface in a LO-NIL process. However, copper tends to oxidize rapidly, which reduces or even stops its catalytic capabilities. Although it is possible to electrochemically reduce the naturally grown copper oxide by applying a suitable voltage when immersing it in the electrolyte, it is beneficial to deposit just a thin copper layer on top of the gold nano-islands of samples fabricated with the standard process as described in this thesis. This can be done with electrodeposition in a copper-containing electrolyte. This has two advantages: first, the sample is already fixed in the measurement cell, thus only the electrolyte has to be changed between deposition and measurement. As this can be performed while applying

a protective potential, oxidation of the copper surface is prevented. And second, when growing a thin copper shell with only some monolayers thickness on top of the gold electrode, one could make use of strain effects in the copper layer leading to optimized energy levels for CO_2 reduction and CH_4 production. Similar effects have already been reported for Pd on Au support as well as for platinum overlayers on gold[81,116,117].

This core-shell approach has been tested during this thesis. Typically, one can make use of the underpotential deposition effect (UPD). It is the electrodeposition of a metal on a support, at a potential less negative than the equilibrium potential for the reduction of this metal. In other words, when a metal can deposit onto another material more easily than it can deposit onto itself. The advantage of this method is an intrinsic growth stop when the deposited metal reaches bulk properties. This is typically already the case after only few monolayers. In fact, it is even possible to deposit only a single monolayer on the target support material.

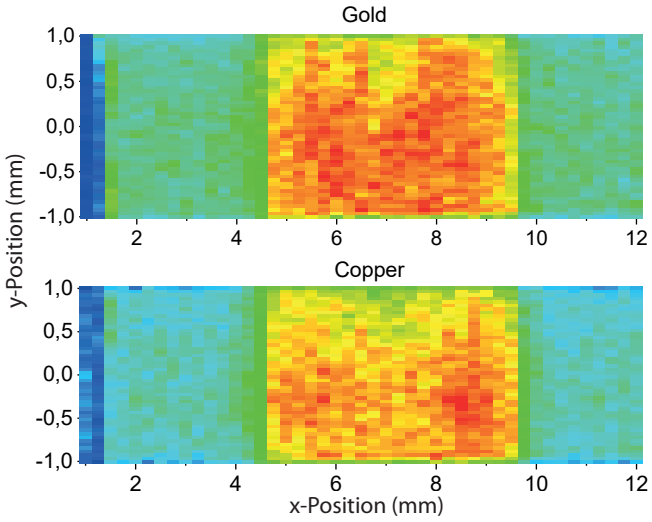

Figure 8.1: XPS mapping image of a lift-off sample with 200 nm gold squares. The XPS measurements are performed after electrochemical copper deposition. A copper signal can only be detected on top of the structured gold area.

Underpotential deposition of copper on the fabricated nanostructured gold electrodes has been performed, and the result has been checked with XPS mapping technique (figure 8.1). The UPD was carried out by the group of Prof. Krischer. In figure 8.1, the XPS mapping of a sample after copper deposition is presented. In the upper sub-figure, the gold signal is shown using this scanning mode. On the very left on the x-axes, the blue (dark) area indicates the edge of the sample. The area between 4.5 mm and 9.5 mm (yellow and red) is the nanopatterned part,

thus giving a high gold signal. As the copper layer is very thin, the XPS can still detect the gold core within the copper shell. The 5x5 mm^2 structured area is surrounded by the blank Si/SiO_2 substrate, without a measurable gold signal. In the lower sub-figure, the detector has been adjusted to record the copper signal only. It is clearly visible, that the deposition of copper has only taken place on top of the patterned gold electrode.
With these copper-coated samples, the production of methane and ethylene could be already proven in product analysis measurements. Optimizing the process and sample design for this purpose needs to be examined in more detail in future work.

Utilizing plasmonic effects in photocatalysis In recent years, the use of surface plasmon polaritons (SPPs), collective oscillations of the electron ensemble, on metal nanostructures has been proposed for a wide range of applications ranging from sensing, for example in surface-enhanced Raman spectroscopy (SERS)[118–121], surface-enhanced infrared absorption spectroscopy (SEIRAS)[120,122,123] or gas sensing[46] over integration of optical and electrical circuits[124,125] photovoltaic applications, such as the enhancement of light absorption[126–128] and light-emitting diodes (LEDs)[129] to catalytic[130–134] and photoelectrochemical purposes[88,89].
Especially the last point is interesting because it offers an exciting opportunity to optimize electrocatalytic processes. Surface plasmons can enhance electromagnetic fields locally by orders of magnitude (section 7.3.2) and lead to a high concentration of electrons at the Catalyst-Electrolyte interface, which is crucial for electrochemical reactions. It can increase photon absorption tailored for the solar spectrum[135], or it can be used to especially increase rate-determining steps in multi-step catalytic reaction pathways by exciting vibrational modes of molecules (in this case, CO_2). And even if it is not possible to address a particular intermediate step in the reaction pathway, plasmon heating can lead to a local heating effect, which intrinsically only occurs at the local interface regions of the heterogeneous catalysis where reactions actually take place[136–139]
The requirements for the fabrication of nanostructures for these techniques are as versatile as the applications. As they respond very sensitively to environmental changes, high reproducibility and cleanliness have to be ensured as well as the fabrication on large areas at low cost. The tunability of the plasmonic resonance is required for sensing[46,119] LEDs[129], systems with certain spectral transparency windows[140], or the excitation of electronically excited states in molecules[131–134]. Fine-tuning of the resonances is important when they shall be excited using

monochromatic light sources such as LEDs or lasers[136]. Depending on the purpose, the plasmonic resonance frequency can reach from the near-ultraviolet to the mid-infrared spectral range.
It has been shown in the previous sections and in the literature that different parameters, especially structure size[92–94] aspect ratio[141], arrangement[142,143], metal composition[92], the refractive index of the substrate[141,144] and the interface between substrate and nanostructures[96] influence the resonance. For more sophisticated techniques, even the exact shape can be of interest, for example, nanotriangles or antennas have been shown to be beneficial for more effective sensing[123,124,145]. These requirements can be fulfilled with nanoimprint technologies as presented in this thesis. Simulations and measurements (section 7.4) in this work already proved the fabricated devices to be plasmonically active. Even when transitioning to a copper electrode system, it can be utilized for electric-field enhancement for increased reaction rates or to change product selectivity, as copper is also known to be a plasmonically active material in the visible and near infra-red region.

Stand-alone device design For a stand-alone device, the pure p-Si substrate in the presented experiments has to be substituted with a photovoltaic structure yielding a sufficiently high voltage. For the characterization of size-dependent effects of the nanopatterned electrode, only p-Si was used here for several reasons: First, the process time and costs are greatly reduced. Then, the actual potential on the electrode surface can be freely defined by applying a voltage using a potentiostat. And finally, the reduced device complexity limits possible sources of error and influence when interpreting the measurement data.
The photovoltage of a standard solar cell is limited to the band gap of the semiconductor, which is 1.12 V for a silicon-based device. However, the HER potential is 1.23 V, and there is always the need for an additionally applied over-potential. One solution to this problem would be to use a different material system. In literature, a wide variety of substrate types (or photoabsober material combinations) are being used, especially wide-bandgap materials such as titanium dioxide (TiO_2) or cadmium sulfide (CdS). However, these substrates have the trade-off to have a poor utilization of the solar spectrum so that silicon multi-junction cells may be the best choice to be used in order to combine a high voltage with better efficiencies[10,11,146,147]. The use of a-Si:H/c-Si:H cells for the photoelectrochemical reduction of CO_2 would consequently lead to the same Au-Si interface, like the one studied in this thesis. In future work, a multi-junction cell is the best option

to develop a stand-alone device.

Large scale, high-throughput nanostructure fabrication For scientific research applications, only small patterned areas are usually required, and larger variations of the structural layouts are needed instead. However, nanoimprint technologies have the advantage of being easily scalable. In this thesis, a plate-to-plate approach was chosen (a flat and "hard" stamp and substrate). While the typical sample dimension was around 1 cm^2 this can be easily increased to full wafer scale. Figure 8.2 shows such a nanoimprint on a full 6 inch silicon wafer, which was performed as a test during this thesis using surface conformal imprint lithography (SCIL).

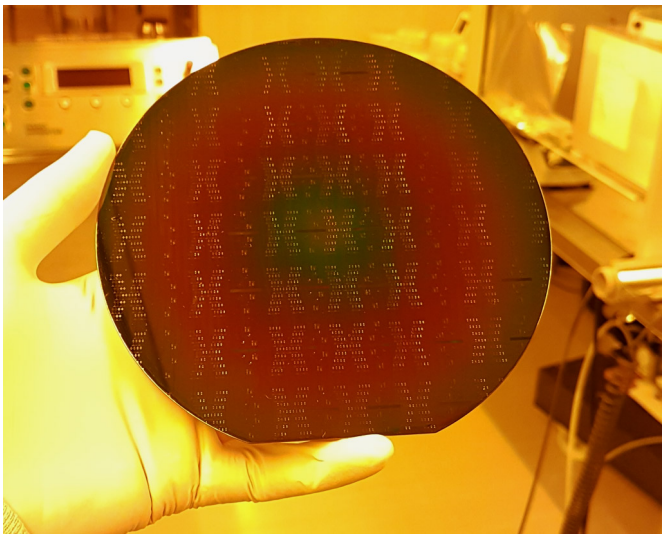

Figure 8.2: Picture of a performed full-scale nanoimprint on a 6 inch silicon wafer.

Also, a roll-to-roll or roll-to-plate approach could be interesting, where the stamp pattern is written directly on a roller or a roller is used to press a continuous flexible stamp on a substrate[148–151]. This offers high-throughput for replicating micro- and nanostructures, fulfilling industrial-scale applications.

9 References

[1] Gordon E. Moore. Cramming more components onto integrated circuits. IEEE Solid-State Circuits Society Newsletter, 11(3):33–35, sep 2006.

[2] Stephen Y Chou. Nanoimprint lithography. Journal of Vacuum Science & Technology B: Microelectronics and Nanometer Structures, 14(6):4129, nov 1996.

[3] Stephen Y Chou, Peter R Krauss, and Preston J Renstrom. Imprint Lithography with 25-Nanometer Resolution. Science, 272(5258):85–87, apr 1996.

[4] Akihiro Nakamura, Yasuyuki Ota, Kayo Koike, Yoshihide Hidaka, Kensuke Nishioka, Masakazu Sugiyama, and Katsushi Fujii. A 24.4% solar to hydrogen energy conversion efficiency by combining concentrator photovoltaic modules and electrochemical cells. Applied Physics Express, 8(10), 2015.

[5] Pei Zhai, Sophia Haussener, Joel Ager, Roger Sathre, Karl Walczak, Jeffery Greenblatt, and Thomas McKone. Net primary energy balance of a solar-driven photoelectrochemical water-splitting device. Energy and Environmental Science, 6(8):2380–2389, 2013.

[6] Michael G. Walter, Emily L. Warren, James R. McKone, Shannon W. Boettcher, Qixi Mi, Elizabeth A. Santori, and Nathan S. Lewis. Solar water splitting cells. Chemical Reviews, 110(11):6446–6473, 2010.

[7] Severin N. Habisreutinger, Lukas Schmidt-Mende, and Jacek K. Stolarczyk. Photocatalytic reduction of CO2 on TiO2 and other semiconductors. Angewandte Chemie - International Edition, 52(29):7372–7408, 2013.

[8] Bhupendra Kumar, Mark Llorente, Jesse Froehlich, Tram Dang, Aaron Sathrum, and Clifford P. Kubiak. Photochemical and Photoelectrochemical Reduction of CO 2. Annual Review of Physical Chemistry, 63(1):541–569, 2012.

[9] Jinli Qiao, Yuyu Liu, Feng Hong, and Jiujun Zhang. A review of catalysts for the electroreduction of carbon dioxide to produce low-carbon fuels. Chemical Society Reviews, 43(2):631–675, 2014.

[10] Jürgen Ziegler, Bernhard Kaiser, Wolfram Jaegermann, Félix Urbain, Jan Philipp Becker, Vladimir Smirnov, and Friedhelm Finger. Photoelectrochemical and photovoltaic characteristics of amorphous-silicon-based tandem cells as photocathodes for water splitting. ChemPhysChem, 15(18):4026–4031, 2014.

[11] F. Urbain, K. Wilken, V. Smirnov, O. Astakhov, A. Lambertz, J. P. Becker, U. Rau, J. Ziegler, B. Kaiser, W. Jaegermann, and F. Finger. Development of thin film amorphous silicon tandem junction based photocathodes providing high open-circuit voltages for hydrogen production. International Journal of Photoenergy, 2014(July), 2014.

[12] Zhaoning Yu, D. Wasserman, S. A. Lyon, Michael D. Austin, Mingtao Li, Stephen Y. Chou, Wei Wu, and Haixiong Ge. Fabrication of 5nm linewidth and 14nm pitch features by nanoimprint lithography. Applied Physics Letters, 84(26):5299–5301, 2004.

[13] Robin D. Nagel, Simon Filser, Tianyue Zhang, Aurora Manzi, Konrad Schönleber, James Lindsly, Josef Zimmermann, Thomas L. Maier, Giuseppe Scarpa, Katharina Krischer, and Paolo Lugli. Nanoimprint methods for the fabrication of macroscopic plasmonically active metal nanostructures. Journal of Applied Physics, 121(8):084305, feb 2017.

[14] Hongqin Liu, Sabine Szunerits, Wenguo Xu, and Rabah Boukherroub. Preparation of superhydrophobic coatings on zinc as effective corrosion barriers. ACS Applied Materials and Interfaces, 1(6):1150–1153, 2009.

[15] Maciej Psarski, Jacek Marczak, Grzegorz Celichowski, Grzegorz B. Sobieraj, Konrad Gumowski, Feng Zhou, and Weimin Liu. Hydrophobization of epoxy nanocomposite surface with 1H,1H,2H,2H-perfluorooctyltrichlorosilane for superhydrophobic properties. Central European Journal of Physics, 10(5):1197–1201, 2012.

[16] Robin D. Nagel, Tobias Haeberle, Morten Schmidt, Paolo Lugli, and Giuseppe Scarpa. Large Area Nano-transfer Printing of Sub-50-nm Metal Nanostructures Using Low-cost Semi-flexible Hybrid Templates. Nanoscale Research Letters, 11 (1):143, dec 2016.

[17] Stephen Y Chou. Sub-10 nm imprint lithography and applications. Journal of Vacuum Science & Technology B: Microelectronics and Nanometer Structures, 15(6):2897, nov 1997.

[18] D Cheyns, K Vasseur, C Rolin, J Genoe, J Poortmans, and P Heremans. Nanoimprinted semiconducting polymer films with 50Â nm features and their application to organic heterojunction solar cells. Nanotechnology, 19(42):424016, oct 2008.

[19] Wenjin Zeng, Karen Siew Ling Chong, Hong Yee Low, Evan Laurence Williams, Teck Lip Tam, and Alan Sellinger. The use of nanoimprint lithography to improve efficiencies of bilayer organic solar cells based on P3HT and a small molecule acceptor. Thin Solid Films, 517(24):6833–6836, oct 2009.

[20] Yiping Zhao, Erwin Berenschot, Meint De Boer, Henri Jansen, Niels Tas, Jurriaan Huskens, and Miko Elwenspoek. Fabrication of a silicon oxide stamp by edge lithography reinforced with silicon nitride for nanoimprint lithography. Journal of Micromechanics and Microengineering, 18(6), 2008.

[21] Tomi Haatainen, Päivi Majander, Tommi Riekkinen, and Jouni Ahopelto. Nickel stamp fabrication using step & stamp imprint lithography. Microelectronic Engineering, 83(4-9 SPEC. ISS.):948–950, 2006.

[22] M. Mühlberger, I. Bergmair, A. Klukowska, A. Kolander, H. Leichtfried, E. Platzgummer, H. Loeschner, Ch. Ebm, G. Grützner, and R. Schöftner. UV-NIL with working stamps made from Ormostamp. Microelectronic Engineering, 86(4-6):691–693, apr 2009.

[23] Amit Kumar and George M. Whitesides. Features of gold having micrometer to centimeter dimensions can be formed through a combination of stamping with an elastomeric stamp and an alkanethiol "ink" followed by chemical etching. Applied Physics Letters, 63(14):2002–2004, 1993.

[24] Dong Qin, Younan Xia, and George M Whitesides. Soft lithography for micro- and nanoscale patterning. Nature protocols, 5(3):491–502, 2010.

[25] D. Armani, C. Liu, and N. Aluru. Re-configurable fluid circuits by PDMS elastomer micromachining. Technical Digest. IEEE International MEMS 99 Conference. Twelfth IEEE International Conference on Micro Electro Mechanical Systems (Cat. No.99CH36291), pages 222–227, 1999.

[26] Ying Zhang, Chi-Wei Lo, J Ashley Taylor, and Shu Yang. Replica molding of high-aspect-ratio polymeric nanopillar arrays with high fidelity. Langmuir : the ACS journal of surfaces and colloids, 22(20):8595–601, sep 2006.

[27] Tobias Haeberle. Metal transfer printing as an enabling technology for device fabrication. PhD thesis, Technical University Munich, 2018.

[28] Anna Klukowska, Anett Kolander, Iris Bergmair, Michael Mühlberger, Hannes Leichtfried, Freimut Reuther, Gabi Grützner, and Rainer Schöftner. Novel transparent hybrid polymer working stamp for UV-imprinting. Microelectronic Engineering, 86(4-6):697–699, apr 2009.

[29] Micro resist technology. Ormostamp - for polymer working stamps, 2014.

[30] SCHOTT AG. Spezifikation - Physikalische und chemische Eigenschaften D 263® T eco, April 2009.

[31] C.Y. Hui, A. Jagota, Y.Y. Lin, and E.J. Kramer. Constraints on Microcontact Printing Imposed by Stamp Deformation. Langmuir, 18(4):1394–1407, feb 2002.

[32] Andreas Finn, Bo Lu, Robert Kirchner, Xaver Thrun, Karola Richter, and Wolf-Joachim Fischer. High aspect ratio pattern collapse of polymeric UV-nanoimprint molds due to cleaning. Microelectronic Engineering, 110:112–118, oct 2013.

[33] Matthew A. Hopcroft, William D. Nix, and Thomas W. Kenny. What is the Young's modulus of silicon? Journal of Microelectromechanical Systems, 19(2): 229–238, 2010.

[34] Thomas Bodner, Andreas Behrendt, Emil Prax, and Frank Wiesbrock. Correlation of surface roughness and surface energy of silicon-based materials with their priming reactivity. Monatshefte für Chemie - Chemical Monthly, 143(5):717–722, feb 2012.

[35] Tu T. Truong, Rongsheng Lin, Seokwoo Jeon, Hee Hyun Lee, Joana Maria, Anshu Gaur, Feng Hua, Ines Meinel, and John A. Rogers. Soft lithography using acryloxy perfluoropolyether composite stamps. Langmuir, 23(5):2898–2905, 2007.

[36] M.J. Stefan. Parallel Platten Rheometer. Akad. Wiss. Math.-Naturwiss. Vienna, 2(69), 1874.

[37] Richard S Stearns, I. N. Duling, and Robert H Johnson. Relationship of Glass Transition Temperature to Viscosity-Temperature Characteristics of Lubricants. Industrial & Engineering Chemistry Product Research and Development, 5(4): 306–313, dec 1966.

[38] Jerzy Zarzycki. Glasses and the vitreous state. Cambridge University Press, 1991.

[39] M.J. Mondry, D.I. Babic, J.E. Bowers, and L.A. Coldren. Refractive indexes of (Al,Ga,In)As epilayers on InP for optoelectronic applications. IEEE Photonics Technology Letters, 4(6):627–630, jun 1992.

[40] Micro resist technology. mr-I 8000R Thermoplastic Polymer for Nanoimprint Lithography with Improved Release Properties, 2012.

[41] MicroChem. LOR and PMGI Resists, 2007.

[42] Nano Dennmark ApS. NDK-UV-01 & NDK Primer, 2014.

[43] Micro resist technology. mr-UVCur21 SF - UV-curable Polymer for UV-based Nanoimprint Lithography, 2012.

[44] Micro resist technology. Processing Guidelines - OrmoStamp, 2012.

[45] Martin A. Green and Mark J Keevers. Optical properties of intrinsic silicon at 300 K. Progress in Photovoltaics: Research and Applications, 3(3):189–192, 1995.

[46] P J Rodríguez-Cantó, M Martínez-Marco, F J Rodríguez-Fortuño, B Tomás-Navarro, R Ortuño, S Peransí-Llopis, and A Martínez. Demonstration of near infrared gas sensing using gold nanodisks on functionalized silicon. Optics express, 19(8):7664–7672, 2011.

[47] P. B. Johnson and R. W. Christy. Optical Constants of the Noble Metals. Physical Review B, 6(12):4370–4379, dec 1972.

[48] Kevin M. McPeak, Sriharsha V. Jayanti, Stephan J P Kress, Stefan Meyer, Stelio Iotti, Aurelio Rossinelli, and David J. Norris. Plasmonic Films Can Easily Be Better: Rules and Recipes. ACS Photonics, 2(3):326–333, mar 2015.

[49] David B Hall, Patrick Underhill, and John M Torkelson. Spin coating of thin and ultrathin polymer films. Polymer Engineering & Science, 38(12):2039–2045, dec 1998.

[50] M.D. Tyona. A theoritical study on spin coating technique. Advances in materials Research, 2(4):195–208, dec 2013.

[51] D. E. Bornside, C. W. Macosko, and L. E. Scriven. Spin coating: One-dimensional model. Journal of Applied Physics, 66(11):5185–5193, 1989.

[52] James Lindsly. Herstellung und Charakterisierung von metallischen Nanostrukturen mittels Lift-off Nanoimprint Lithografie für elektrokatalytische Anwendungen. PhD thesis, Technical University Munich, 2015.

[53] Franz Laermer, Andrea Schilp, and Bernhard Elsner. EP1095400. Technical report, Europäisches Patentamt, 1996.

[54] Jeremy Golden, Harris Miller, Dan Nawrocki, and Jack Ross. Optimization of Bi-layer Lift-Off Resist Process. 2009.

[55] Giuseppe Scarpa, Stefan Harrer, Alaa Abdellah, Guillermo Penso-blanco, Paolo Lugli, Sebastian Strobel, and Gerhard Abstreiter. Pattern Generation by Using High-Resolution Nanoimprinting and Nanotransfer Printing Techniques. 9th IEEE Conference on, 8:432–438, 2009.

[56] Mario Bareiss, Benedikt Weiler, Daniel Kalblein, Ute Zschieschang, Hagen Klauk, Giuseppe Scarpa, Bernhard Fabel, Paolo Lugli, and Wolfgang Porod. Nanotransfer printing of functioning MIM tunnel diodes. In 2012 IEEE Silicon Nanoelectronics Workshop (SNW), pages 1–2. IEEE, jun 2012.

[57] Benedikt Weiler, Robin Nagel, Tim Albes, Tobias Haeberle, Alessio Gagliardi, and Paolo Lugli. Electrical and morphological characterization of transfer-printed Au/Ti/TiOx/p+-Si nano- and microstructures with plasma-grown titanium oxide layers. Journal of Applied Physics, 119(14):145106, apr 2016.

[58] Yueh-lin Loo, Robert L Willett, Kirk W Baldwin, and John A Rogers. Additive, nanoscale patterning of metal films with a stamp and a surface chemistry mediated transfer process: Applications in plastic electronics. Applied Physics Letters, 81(3):562, 2002.

[59] T. Suni, K. Henttinen, I. Suni, and J. MaÌˆkinen. Effects of Plasma Activation on Hydrophilic Bonding of Si and SiO[sub 2]. Journal of The Electrochemical Society, 149(6):G348, 2002.

[60] G. Kissinger and W. Kissinger. Hydrophilicity of Silicon Wafers for Direct Bonding. Physica Status Solidi (a), 123(1):185–192, jan 1991.

[61] Yueh-Lin Loo, Robert L Willett, Kirk W Baldwin, and John a Rogers. Interfacial Chemistries for Nanoscale Transfer Printing. Journal of the American Chemical Society, 124(26):7654–7655, jul 2002.

[62] Brinker KC Zapp JA, Limperos G and Limperos G Zapp JA. Toxicity of pyrolysis products of 'Teflon' tetrafluoroethylene resin. Proceedings of the American Industrial Hygiene Association Annual Meeting, 1955.

[63] V. Masteika, J. Kowal, N. S. J. Braithwaite, and T. Rogers. A Review of Hydrophilic Silicon Wafer Bonding. ECS Journal of Solid State Science and Technology, 3(4):Q42–Q54, feb 2014.

[64] M. M. R. Howlader, T. Suga, H. Itoh, T. H. Lee, and M. J. Kim. Role of Heating on Plasma-Activated Silicon Wafers Bonding. Journal of The Electrochemical Society, 156(11):H846, 2009.

[65] Jakub Siegel, Olexiy Lyutakov, Vladimír Rybka, ZdeÅˆka Kolská, and Václav Švorčík. Properties of gold nanostructures sputtered on glass. Nanoscale Research Letters, 6(1):96, dec 2011.

[66] Walter M. Kane, James P. Spratt, and Lincoln W. Hershinger. Effects of annealing on thin gold films. Journal of Applied Physics, 37(5):2085–2089, 1966.

[67] Benedikt Weiler. Nanotransfer Printing and Kinetic Monte Carlo Simulations of Metal-Oxide-Structures. PhD thesis, Technical University Munich, 2016.

[68] V. Mikhelashvili and G. Eisenstein. Effects of annealing conditions on optical and electrical characteristics of titanium dioxide films deposited by electron beam evaporation. Journal of Applied Physics, 89(6):3256–3269, 2001.

[69] Qiong Cheng, Waqas Ahmad, Guohua Liu, and Kaiying Wang. Structural evolution of amorphous thin films of titanium dioxide. Proceedings of the IEEE Conference on Nanotechnology, pages 1598–1601, 2011.

[70] Tomohito Sekine, Kenjiro Fukuda, Daisuke Kumaki, and Shizuo Tokito. Enhanced adhesion mechanisms between printed nano-silver electrodes and underlying polymer layers. Nanotechnology, 26(32):321001, aug 2015.

[71] Myung-Gyu Kang, Myung-Su Kim, Jinsang Kim, and L. Jay Guo. Organic Solar Cells Using Nanoimprinted Transparent Metal Electrodes. Advanced Materials, 20(23):4408–4413, dec 2008.

[72] Stephen Y Chou and Wei Ding. Ultrathin, high-efficiency, broad-band, omni-acceptance, organic solar cells enhanced by plasmonic cavity with subwavelength hole array. Optics express, 21 Suppl 1(January):A60–76, 2013.

[73] Morten Schmidt. Alternative fabrication techniques for organic electronic devices. PhD thesis, Technical University Munich, 2017.

[74] Allen J. Bard and Larry R. Faulkner. Electrochemical Methods: Fundamentals and Applications. John Wiley & Sons, Inc., 2001.

[75] Winfried Mönch. On the alleviation of Fermi-level pinning by ultrathin insulator layers in Schottky contacts. Journal of Applied Physics, 111(7), 2012.

[76] Ruud Kortlever, Jing Shen, Klaas Jan P Schouten, Federico Calle-Vallejo, and Marc T M Koper. Catalysts and Reaction Pathways for the Electrochemical Reduction of Carbon Dioxide. The Journal of Physical Chemistry Letters, 6(20): 4073–4082, oct 2015.

[77] Paul Sabatier. Hydrogénations et déshydrogénations par catalyse. Berichte der deutschen chemischen Gesellschaft, 44(3):1984–2001, jul 1911.

[78] Paola Quaino, Fernanda Juarez, Elizabeth Santos, and Wolfgang Schmickler. Volcano plots in hydrogen electrocatalysis - uses and abuses. Beilstein journal of nanotechnology, 5(1):846–54, 2014.

[79] Yoshio Hori, Hidetoshi Wakebe, Toshio Tsukamoto, and Osamu Koga. Electrocatalytic process of CO selectivity in electrochemical reduction of CO2 at metal electrodes in aqueous media. Electrochimica Acta, 39(11-12):1833–1839, aug 1994.

[80] André D. Taylor, Brandon D. Lucas, L. Jay Guo, and Levi T. Thompson. Nanoimprinted electrodes for micro-fuel cell applications. Journal of Power Sources, 171(1):218–223, sep 2007.

[81] Holger Wolfschmidt, Rainer Bussar, and Ulrich Stimming. Charge transfer reactions at nanostructured Au(111) surfaces: influence of the substrate material on electrocatalytic activity. Journal of physics. Condensed matter : an Institute of Physics journal, 20(37):374127, sep 2008.

[82] Yoshio Hori, Katsuhei Kikuchi, and Shin Suzuki. Production of CO and CH4 in electrochemical reduction of CO2 at metal electrodes in aqueous hydrogencarbonate solution. Chemistry Letters, 14(11):1695–1698, nov 1985.

[83] R Hinogami, Y Nakamura, S. Yae, and Y. Nakato. An Approach to Ideal Semiconductor Electrodes for Efficient Photoelectrochemical Reduction of Carbon Dioxide by Modification with Small Metal Particles. The Journal of Physical Chemistry B, 102(6):974–980, feb 1998.

[84] Cornelia Ostermayr. Electrocatalytic activity of platinum on extended gold surfaces and defined gold-nanostructure arrays for the hydrogen reactions. PhD thesis, Technical University Munich, 2014.

[85] Christopher Hakoda, Joseph Rose, Parisa Shokouhi, and Clifford Lissenden. Using Floquet periodicity to easily calculate dispersion curves and wave structures of homogeneous waveguides. AIP Conference Proceedings, 1949(April), 2018.

[86] L. Gao, R. Lemarchand, and M. Lequime. Refractive index determination of SiO2 layer in the UV/Vis/NIR range: Spectrophotometric reverse engineering on single and bi-layer designs. Journal of the European Optical Society, 8:13010, 2013.

[87] Luis V. Rodríguez-de Marcos, Juan I. Larruquert, José A. Méndez, and José A. Aznárez. Self-consistent optical constants of SiO_2 and Ta_2O_5 films. Optical Materials Express, 6(11):3622, 2016.

[88] Peng Wang, Baibiao Huang, Ying Dai, and Myung-Hwan Whangbo. Plasmonic photocatalysts: harvesting visible light with noble metal nanoparticles. Physical Chemistry Chemical Physics, 14(28):9813, 2012.

[89] Xuming Zhang, Yu Lim Chen, Ru-Shi Liu, and Din Ping Tsai. Plasmonic photocatalysis. Reports on progress in physics. Physical Society (Great Britain), 76 (4):046401, apr 2013.

[90] Simon Filser, Thomas L. Maier, Robin D. Nagel, Werner Schindler, Paolo Lugli, Markus Becherer, and Katharina Krischer. Photoelectrochemical reactivity of well-defined mesoscale gold arrays on SiO2/Si substrates in CO2-saturated aqueous electrolyte. Electrochimica Acta, 268:546–553, 2018.

[91] James R. Chelikowsky and Marvin L. Cohen. Electronic structure of silicon. Physical Review B, 10(12):5095–5107, dec 1974.

[92] Kyeong Seok Lee and Mostafa A. El-Sayed. Gold and silver nanoparticles in sensing and imaging: Sensitivity of plasmon response to size, shape, and metal composition. Journal of Physical Chemistry B, 110(39):19220–19225, 2006.

[93] Christoph Langhammer, Zhe Yuan, Igor Zorić, and Bengt Kasemo. Plasmonic properties of supported Pt and Pd nanostructures. Nano Letters, 6(4):833–838, 2006.

[94] Igor Zorić, Michael Zäch, Bengt Kasemo, and Christoph Langhammer. Gold, platinum, and aluminum nanodisk plasmons: Material independence, subradiance, and damping mechanisms. ACS Nano, 5(4):2535–2546, 2011.

[95] J. J. Mock, M. Barbic, D. R. Smith, D. A. Schultz, and S. Schultz. Shape effects in plasmon resonance of individual colloidal silver nanoparticles. Journal of Chemical Physics, 116(15):6755–6759, 2002.

[96] Terefe G. Habteyes, Scott Dhuey, Erin Wood, Daniel Gargas, Stefano Cabrini, P. James Schuck, A. Paul Alivisatos, and Stephen R. Leone. Metallic adhesion layer induced plasmon damping and molecular linker as a nondamping alternative. ACS Nano, 6(6):5702–5709, 2012.

[97] Heykel Aouani, Jerome Wenger, Davy Gerard, Herve Rigneault, Eloise Devaux, Thomas W. Ebbesen, Farhad Mahdavi, Tingjun Xu, and Steve Blair. Crucial Role of the Adhesion Layer on the Plasmonic Fluorescence Enhancement. ACS Nano, 3(7):2043–2048, jul 2009.

[98] Thomas Siegfried, Yasin Ekinci, Olivier J.F. Martin, and Hans Sigg. Engineering Metal Adhesion Layers That Do Not Deteriorate Plasmon Resonances. ACS Nano, 7(3):2751–2757, mar 2013.

[99] Andreas Trügler, Jean-Claude Tinguely, Georg Jakopic, Ulrich Hohenester, Joachim R. Krenn, and Andreas Hohenau. Near-field and SERS enhancement from rough plasmonic nanoparticles. Physical Review B, 89(16):165409, apr 2014.

[100] Andreas Trügler, Jean-claude Tinguely, Joachim Krenn, Andreas Hohenau, and Ulrich Hohenester. Influence of surface roughness on the optical properties of plasmonic nanoparticles. Physical Review B, 83(8):081412, 2011.

[101] Jessica Rodríguez-Fernández, Alison M. Funston, Jorge Pérez-Juste, Ramón A. Álvarez-Puebla, Luis M. Liz-Marzán, and Paul Mulvaney. The effect of surface roughness on the plasmonic response of individual sub-micron gold spheres. Physical Chemistry Chemical Physics, 11(28):5909, 2009.

[102] Jean-Claude Tinguely, Idrissa Sow, Claude Leiner, Johan Grand, Andreas Hohenau, Nordin Felidj, Jean Aubard, and Joachim R. Krenn. Gold Nanoparticles for Plasmonic Biosensing: The Role of Metal Crystallinity and Nanoscale Roughness. BioNanoScience, 1(4):128–135, dec 2011.

[103] M J Rost, D a Quist, and J W M Frenken. Grains, Growth, and Grooving. Physical Review Letters, 91(2):026101, jul 2003.

[104] Kuo Ping Chen, Vladimir P. Drachev, Joshua D. Borneman, Alexander V. Kildishev, and Vladimir M. Shalaev. Drude relaxation rate in grained gold nanoantennas. Nano Letters, 10(3):916–922, 2010.

[105] Tobias Haeberle, Florin Loghin, Ute Zschieschang, Hagen Klauk, and Paolo Lugli. Carbon nanotube thin-film transistors featuring transfer-printed metal electrodes and a thin, self-grown aluminum oxide gate dielectric. IEEE-NANO 2015 - 15th International Conference on Nanotechnology, pages 160–163, 2015.

[106] Hye Jin Lee, C. Beriet, R. Ferrigno, and H. H. Girault. Cyclic voltammetry at a regular microdisc electrode array. Journal of Electroanalytical Chemistry, 502 (1-2):138–145, 2001.

[107] Avelino Corma, Mercedes Boronat, Silvia González, and Francesc Illas. On the activation of molecular hydrogen by gold: a theoretical approximation to the nature of potential active sites. Chemical Communications, 32:3371, 2007.

[108] Holger Wolfschmidt, Daniel Weingarth, and Ulrich Stimming. Enhanced reactivity for hydrogen reactions at Pt nanoislands on Au(111). Chemphyschem : a European journal of chemical physics and physical chemistry, 11(7):1533–41, may 2010.

[109] Masatake Haruta. Size- and support-dependency in the catalysis of gold. Catalysis Today, 36(1):153–166, apr 1997.

[110] Brian E. Hayden. Particle size and support effects in electrocatalysis. Accounts of Chemical Research, 46(8):1858–1866, 2013.

[111] Britt Hvolbæk, Ton V.W. Janssens, Bjerne S. Clausen, Hanne Falsig, Claus H. Christensen, and Jens K. Nørskov. Catalytic activity of Au nanoparticles. Nano Today, 2(4):14–18, 2007.

[112] B Hammer and JK Nørskov. Theoretical surface science and catalysis - calculations and concepts. Advances in catalysis, 45:71–129, 2000.

[113] Daniel V. Esposito, Igor Levin, Thomas P. Moffat, and A. Alec Talin. H2 evolution at Si-based metal-insulator-semiconductor photoelectrodes enhanced by inversion channel charge collection and H spillover. Nature Materials, 12(6): 562–568, 2013.

[114] M. Gattrell, N. Gupta, and a. Co. A review of the aqueous electrochemical reduction of CO2 to hydrocarbons at copper. Journal of Electroanalytical Chemistry, 594(1):1–19, aug 2006.

[115] Andrew a. Peterson, Frank Abild-Pedersen, Felix Studt, Jan Rossmeisl, and Jens K. Nørskov. How copper catalyzes the electroreduction of carbon dioxide into hydrocarbon fuels. Energy & Environmental Science, 3(9):1311, 2010.

[116] Ata Roudgar and Axel Groß. Local reactivity of thin Pd overlayers on Au single crystals. Journal of Electroanalytical Chemistry, 548:121–130, may 2003.

[117] Stanislav Pandelov and Ulrich Stimming. Reactivity of monolayers and nanoislands of palladium on Au(111) with respect to proton reduction. Electrochimica Acta, 52(18):5548–5555, may 2007.

[118] Katrin Kneipp, Yang Wang, Harald Kneipp, Lev T. Perelman, Irving Itzkan, Ramachandra R. Dasari, and Michael S. Feld. Single Molecule Detection Using Surface-Enhanced Raman Scattering (SERS). Physical Review Letters, 78(9): 1667–1670, mar 1997.

[119] Sumeet Mahajan, Mamdouh Abdelsalam, Yoshiro Suguwara, Suzanne Cintra, Andrea Russell, Jeremy Baumberg, and Philip Bartlett. Tuning plasmons on nano-structured substrates for NIR-SERS. Physical Chemistry Chemical Physics, 9(1):104–109, 2007.

[120] Surbhi Lal, Nathaniel K. Grady, Janardan Kundu, Carly S. Levin, J. Britt Lassiter, and Naomi J. Halas. Tailoring plasmonic substrates for surface enhanced spectroscopies. Chemical Society Reviews, 37(5):898–911, 2008.

[121] Chao Wang and Stephen Y Chou. Integration of Metallic Nanostructures in Fluidic Channels for Fluorescence and Raman Enhancement by Nanoimprint Lithography and Lift-off on Compositional Resist Stack. Microelectronic engineering, 98:693–697, oct 2012.

[122] Masatoshi Osawa. Dynamic Processes in Electrochemical Reactions Studied by Surface-Enhanced Infrared Absorption Spectroscopy (SEIRAS). Bulletin of the Chemical Society of Japan, 70(12):2861–2880, 1997.

[123] Lisa V. Brown, Xiao Yang, Ke Zhao, Bob Y. Zheng, Peter Nordlander, and Naomi J. Halas. Fan-shaped gold nanoantennas above reflective substrates for surface-enhanced infrared absorption (SEIRA). Nano Letters, 15(2):1272–1280, 2015.

[124] Ekmel Ozbay. Plasmonics: Merging photonics and electronics at nanoscale dimensions. Science, 311(5758):189–193, 2006.

[125] Matthew Rycenga, Claire M. Cobley, Jie Zeng, Weiyang Li, Christine H. Moran, Qiang Zhang, Dong Qin, and Younan Xia. Controlling the synthesis and assembly of silver nanostructures for plasmonic applications. Chemical Reviews, 111(6): 3669–3712, 2011.

[126] S. Pillai, K. R. Catchpole, T. Trupke, and M. A. Green. Surface plasmon enhanced silicon solar cells. Journal of Applied Physics, 101(9), 2007.

[127] Harry A Atwater and Albert Polman. Plasmonics for improved photovoltaic devices. Nature Materials, 9(10):865–865, oct 2010.

[128] P. Spinelli, E. Ferry, J. Van De Groep, M. Van Lare, A. Verschuuren, I. Schropp, A. Atwater, A. Polman, P. Spinelli, V. E. Ferry, J. Van De Groep, M. Van Lare, M. A. Verschuuren, R. E.I. Schropp, H. A. Atwater, and A. Polman. Plasmonic light trapping in thin-film Si solar cells. Journal of Optics, 14(2), 2012.

[129] Xuefeng Gu, Teng Qiu, Wenjun Zhang, and Paul K. Chu. Light-emitting diodes enhanced by localized surface plasmon resonance. Nanoscale Research Letters, 6 (1):199, 2011.

[130] Xi Chen, Huai Yong Zhu, Jin Cai Zhao, Zhan Feng Zheng, and Xue Ping Gao. Visible-light-driven oxidation of organic contaminants in air with gold nanoparticle catalysts on oxide supports. Angewandte Chemie - International Edition, 47(29):5353–5356, 2008.

[131] Phillip Christopher, Hongliang Xin, and Suljo Linic. Visible-light-enhanced catalytic oxidation reactions on plasmonic silver nanostructures. Nature Chemistry, 3(6):467–472, may 2011.

[132] Xuebin Ke, Sarina Sarina, Jian Zhao, Xingguang Zhang, Jin Chang, and Huaiyong Zhu. Tuning the reduction power of supported gold nanoparticle photocatalysts for selective reductions by manipulating the wavelength of visible light irradiation. Chemical Communications, 48(29):3509–3511, 2012.

[133] Matthew J. Kale, Talin Avanesian, and Phillip Christopher. Direct Photocatalysis by Plasmonic Nanostructures. ACS Catalysis, 4(1):116–128, jan 2014.

[134] Talin Avanesian and Phillip Christopher. Adsorbate specificity in hot electron driven photochemistry on catalytic metal surfaces. Journal of Physical Chemistry C, 118(48):28017–28031, 2014.

[135] Scott K. Cushing, Alan D. Bristow, and Nianqiang Wu. Theoretical maximum efficiency of solar energy conversion in plasmonic metal-semiconductor heterojunctions. Physical Chemistry Chemical Physics, 17(44):30013–30022, 2015.

[136] James R. Adleman, David A. Boyd, David G. Goodwin, and Demetri Psaltis. Heterogenous catalysis mediated by plasmon heating. Nano Letters, 9(12):4417–4423, 2009.

[137] Linan Zhou, Dayne F. Swearer, Chao Zhang, Hossein Robatjazi, Hangqi Zhao, Luke Henderson, Liangliang Dong, Phillip Christopher, Emily A. Carter, Peter Nordlander, and Naomi J. Halas. Quantifying hot carrier and thermal contributions in plasmonic photocatalysis. Science, 362(6410), 2018.

[138] Yun Yu, Vignesh Sundaresan, and Katherine A. Willets. Hot Carriers versus Thermal Effects: Resolving the Enhancement Mechanisms for Plasmon-Mediated Photoelectrochemical Reactions. Journal of Physical Chemistry C, 122(9), 2018.

[139] Alexander O Govorov and Hugh H Richardson. Generating heat with metal nanoparticles We describe recent studies on photothermal effects using colloidal. Review Literature And Arts Of The Americas, 2(1):30–38, 2007.

[140] Urcan Guler, Justus C. Ndukaife, Gururaj V. Naik, A. G. Agwu Nnanna, Alexander V. Kildishev, Vladimir M. Shalaev, and Alexandra Boltasseva. Local heating with titanium nitride nanoparticles. In CLEO: 2013, volume 753, Washington, D.C., 2013. OSA.

[141] K. Lance Kelly, Eduardo Coronado, Lin Lin Zhao, and George C. Schatz. The optical properties of metal nanoparticles: The influence of size, shape, and dielectric environment. Journal of Physical Chemistry B, 107(3):668–677, 2003.

[142] M. Chergui, A. Melikyan, and H. Minassian. Calculation of surface plasmon frequencies of two, three, and four strongly interacting nanospheres. Journal of Physical Chemistry C, 113(16):6463–6471, 2009.

[143] Yoshiaki Nishijima, Lorenzo Rosa, and Saulius Juodkazis. Surface plasmon resonances in periodic and random patterns of gold nano-disks for broadband light harvesting. Optics Express, 20(10):11466, may 2012.

[144] Mark W. Knight, Yanpeng Wu, J. Britt Lassiter, Peter Nordlander, and Naomi J. Halas. Substrates matter: influence of an adjacent dielectric on an individual plasmonic nanoparticle. Nano Letters, 9(5):2188–2192, 2009.

[145] W. Q. Li, G. Wang, X. N. Zhang, H. P. Geng, J. L. Shen, L. S. Wang, J. Zhao, L. F. Xu, L. J. Zhang, Y. Q. Wu, R. Z. Tai, and G. Chen. Geometrical and morphological optimizations of plasmonic nanoarrays for high-performance SERS detection. Nanoscale, 7(37):15487–15494, 2015.

[146] Félix Urbain, Vladimir Smirnov, Jan Philipp Becker, Uwe Rau, Jürgen Ziegler, Bernhard Kaiser, Wolfram Jaegermann, and Friedhelm Finger. Application and modeling of an integrated amorphous silicon tandem based device for solar water splitting. Solar Energy Materials and Solar Cells, 140:275–280, 2015.

[147] Zhengshan (Jason) Yu, Mehdi Leilaeioun, and Zachary Holman. Selecting tandem partners for silicon solar cells. Nature Energy, 1(September):16137, 2016.

[148] Nazrin Kooy, Khairudin Mohamed, Lee Tze Pin, and Ooi Su Guan. A review of roll-to-roll nanoimprint lithography. Nanoscale Research Letters, 9(1), 2014.

[149] Arne Schleunitz, Christian Spreu, Tapio Mäkelä, Tomi Haatainen, Anna Klukowska, and Helmut Schift. Hybrid working stamps for high speed roll-to-roll nanoreplication with molded solâ€“gel relief on a metal backbone. Microelectronic Engineering, 88(8):2113–2116, aug 2011.

[150] a. Jain and R. T. Bonnecaze. Fluid management in roll-to-roll nanoimprint lithography. Journal of Applied Physics, 113(23):234511, 2013.

[151] Se Hyun Ahn and L Jay Guo. Large-area roll-to-roll and roll-to-plate nanoimprint lithography: a step toward high-throughput application of continuous nanoimprinting. ACS nano, 3(8):2304–10, aug 2009.

10 Acknowledgements

Finally, I want to thank a lot of people, who supported me during the work of this thesis. I was honored to meet you all during this time, I really appreciated it!

First of all, I would like to thank my supervisor, Prof. Dr. Paolo Lugli not only for offering me the great opportunity to work on this exciting topic at his chair but also for his input and the perfect scientific labs and working environment he developed over the years at the Lehrstuhl für Nanoelektronik, Technische Universität München (TUM).

A special thanks to my colleagues: Tobias Häberle and Morten Schmidt, who also worked at the nanopatterning part at our chair and who are co-authors of my publications. Special thanks for all the discussions and all the input you gave me and the countless hours working in the clean-room, making nearly infinite amounts of OrmoStamps.
Of course, Marius Loch, Vijay-Deep Bhatt for fruitful discussions during the work and also during writing my thesis. Benedikt Weiler, for all the work he did for electrical characterization and simulation of transfer printed metal electrodes.
And of course Aniello Falco, Marco Bobinger, Andreas Albrecht, Michael Haider, Florin Loghin, Katharina Melzer, you were always a fantastic team - thanks for sharing the time with me!

The thesis definitely wouldn't be possible without Prof. Dr.-ing. Markus Becherer and Dr.-ing. Bernhard Fabel, keeping things running at the institute, always having an eye on my progress, and having outstanding skills in solving problems of any kind.
Thanks so much to our technicians who supported me whenever they could, for your invaluable experience and knowledge! Rosemarie Mittermaier, Siegfried Schreier and Peter Weiser.

I would like to thank the bachelor and master students James Lindsly and Ste-

fan Lochbrunner I had the pleasure and privilege to work with. Especially James helped me with developing the nanoimprint lift-off process and spend several very long evenings in the labs at the Zentrum für Nanotechnologie und Nanomaterialien (ZNN) in Garching with me. Sorry about that!

I would also like to express my thanks to Prof. Dr. Giuseppe Scarpa who introduced me to the topic and the institute and with whom I worked closely on several lectures and seminars.

I had a kind of second research group during my thesis. We worked intensively in collaboration with the chair of Prof. Krischer, such that it felt like a second home to me at the end of my work. Also, basically everything I know about electrochemistry, I learned from the weekly meetings and the discussions of our measurement results and problems. Here, I worked closely with Simon Filser on the topic of the solar fuel device whose constant commitment to the progress of the work I particularly appreciate. His master and bachelor students Josef Zimmermann and Thomas Maier have actively supported him in this process.

I would like to express my dearest thanks to my parents, my sister and my friends. Without their continuing support and friendship, this work would not have been possible.
Finally, I would like to dedicate this work to my wife, who has unconditionally supported me during this time. Each day together with you brings joy and happiness into my life. My greatest thanks go to you!